First-Principles Calculations of Electronic, Optical, and Transport Properties of Materials for Energy Applications

by

Guangsha Shi

A dissertation submitted in partial fulfillment
of the requirements for the degree of
Doctor of Philosophy
(Materials Science and Engineering and Scientific Computing)
in the University of Michigan
2017

Doctoral Committee:

Assistant Professor Emmanouil Kioupakis, Chair
Associate Professor Pierre Ferdinand P. Poudeu
Assistant Professor Liang Qi
Professor Ctirad Uher

2017

ACKNOWLEDGMENTS

First, I would like to express my sincere gratitude to my advisor Prof. Emmanouil Kioupakis for his continuous support of my Ph.D. study and related research. Prof. Kioupakis did not only helped me in research with his great patience and immense knowledge, but also set a best example to me with his sincerity, kindness, humbleness, and forgiveness. I always feel it a great honor to be the first student to join his research group in University of Michigan. I am fortunate to have Prof. Kioupakis not only as a good mentor in my scientific research, but also as a good mentor in my life.

Besides my advisor, I would like to thank my committee members Prof. Pierre Ferdinand P. Poudeu, Prof. Liang Qi, and Prof. Ctirad Uher, for their insightful comments and encouragement. My sincere thanks also goes to my fellow group mates Dylan Bayerl, Andrew McAllister, Michael Waters, Alex Toulouse, Christina Jones, Jihang Lee, Logan Williams, Kelsey Mengle, Nocona Sanders for the stimulating discussions and memorable moments. I would like to thank my family and my best friends Weimin Wang and Fanbo Meng in particular, as it is their love and company that helped me through the hardest times in the last five years. I am also thankful to Mrs. Renee Hilgendorf for all the administrative support and the care she provided all these years.

This research was supported by the National Science Foundation CAREER award through Grant No. DMR-1254314, and by the Center for Solar and Thermal Energy Conversion, an Energy Frontier Research Center funded by the U.S. Department of Energy Office of Science, Office of Basic Sciences under Award DE-SC0000957. Computational resources were provided by the National Energy Research Scientific Computing Center, supported by the Office of Science of the U.S. Department of Energy under Contract No. DE-AS02-05CH11231.

TABLE OF CONTENTS

LIST OF FIGURES

LIST OF TABLES

ABSTRACT

First-Principles Calculations of Electronic, Optical, and Transport Properties of Materials for Energy Applications

by

Guangsha Shi

Chair: Emmanouil Kioupakis

Solar electricity is a reliable and environmentally friendly method of sustainable energy production and a realistic alternative to conventional fossil fuels. Moreover, thermoelectric energy conversion is a promising technology for solid-state refrigeration and efficient waste-heat recovery. Predicting and optimizing new photovoltaic and thermoelectric materials composed of Earth-abundant elements that exceed the current state of the art, and understanding how nanoscale structuring and ordering improves their energy conversion efficiency pose a challenge for materials scientists.

I approach this challenge by developing and applying predictive high-performance computing methods to guide research and development of new materials for energy-conversion applications. I present my calculated results on the extraordinary properties of nanostructured semiconductor materials, including strong visible-light absorbance in nanoporous silicon and few-layer SnSe and GeSe. These findings highlight the capability of nanoscale structuring and ordering to improve the performance of Earth-abundant materials compared to their bulk counterparts for solar-cell applications. I also successfully identified the dominant mechanisms contributing to free-carrier absorption in n-type silicon. My findings help evaluate the impact of the energy loss from this absorption mechanism in doped silicon and are thus important for the design of silicon solar cells.

In addition, I calculated the thermoelectric transport properties of p-type SnSe, a bulk material with a record thermoelectric figure of merit. I predicted the optimal temperatures and free-carrier concentrations for thermoelectric energy conversion, as well the theoretical upper limit of the figure of merit. I also determined the electronic structures and thermoelectric properties of Mg_2Si, Mg_2Ge, and Mg_2Sn, a family of Earth-abundant thermoelectric compounds.The methods and codes I developed in my research form a general predictive toolbox for the design and optimization of the functional properties of materials for energy applications.

CHAPTER 1

Introduction

The discovery of advanced materials for energy applications has been one of the most significant and urgent tasks for society in the new century. The traditional fossil-fuel-based energy production is not a sustainable solution to our energy needs due to diminishing supply, air pollution, and CO_2 emissions. Moreover, only a fraction of the fossil-fuel energy is converted to useful work, while the majority is lost to heat. Solar electricity is established as a reliable and environmentally friendly method for energy production and a viable alternative to fossil fuels, while thermoelectric energy conversion is promising for efficient waste-heat recovery. Solar electricity has important applications e.g., in the International Space Station, where photovoltaic solar panels are used to derive electricity from sunlight. In the outer solar system, where the sunlight is too weak to produce sufficient power, radioisotope thermoelectric generators are employed to power deepspace spacecraft, such as the Voyager and Cassini missions, as well as the Curiosity rover of the Mars Science Laboratory. Our work on the discovery of novel photovoltaic and thermoelectric materials is also a part of Materials Genome Initiative, which was designed to support and accelerate the discovery and deployment of advanced materials.

Predictive insights from computer simulations can accelerate the discovery of new photovoltaic and thermoelectric compounds. The development of new materials has been the catalyst behind most major technological innovations throughout human history. However, there is a significant delay between the discovery of new materials and their commercial deployment. Advances in computer-simulation algorithms and high-performance computing resources promise to speedup the development of new compounds with desirable properties and significantly shorten this time delay. First-principles calculations based on density functional theory and related techniques are a predictive set of computational tools to model the structural, electronic, vibrational, and transport properties of materials entirely from theory. The ability to describe the transport behavior without any input from experiment is a prerequisite for the computational discovery of new thermoelectric materials. The

theory can also suggest engineering approaches to optimize the thermoelectric performance without lengthy and costly experimental tests.

1.1 Photovoltaic and thermoelectric effects

The photovoltaic effect was first observed by Alexandre-Edmond Becquerel in 1839 and its first commercial use was in 1955 at remotely located telephone repeaters. Solar cells soon established themselves as the power source of choice for satellites in space, and they have held this role ever since. With increasing advancements in technology, the cost of photovoltaic technology, which used to be prohibitively high in its early days, has steadily dropped in recent years. Today, solar electricity has firmly established itself as a premier method of sustainable energy and as a realistic alternative to conventional fossil fuels.

The selection of photovoltaic materials is generally based on their light absorption efficiency, energy conversion efficiency, manufacturing technology, and cost of production. The major types of materials that have been successfully used are crystalline and thin films. Crystalline materials are dominated by single-crystal and polycrystalline silicon, while thin-film materials include amorphous silicon, Gallium Arsenide (GaAs), Cadmium Telluride (CdTe), Copper Indium Gallium Diselenide ($CuInGaSe_2$, or CIGS), etc.. Thin-film materials usually exhibit higher light-absorption efficiency, while the thin deposited layer reduces the materials cost compared to bulk devices. However, their non-single-crystal structures typically result in lower energy conversion efficiency than silicon. The energy conversion efficiency of CIGS, which is the second highest (after GaAs) among all thin-film materials (tested to be 19.7% in 2013[10]), is still lower than laboratory energy conversion efficiencies as high as 25% for single-crystal silicon and 20.4% for polycrystalline silicon.[11] Currently there is a significant ongoing experimental and computational research effort on low-dimensional photovoltaic materials. Computational investigations are particularly useful since they can explore the photovoltaic properties of as-yet unsynthesized materials and can help guide experimental efforts.

Thermoelectric energy conversion is a promising technology for sustainable energy production and utilization. Fossil-fuel-based energy production is not a sustainable solution to the energy needs of our society due to diminishing supply, air pollution, and CO_2 emissions. Moreover, only a fraction of the fossil-fuel energy is converted to useful work, while the majority is lost to heat. Thermoelectric conversion is a reliable and environmentally friendly method to convert heat directly into electricity and is a promising solution to improve the efficiency of fossil-fuel engines. Ongoing research aims to utilize thermoelectric conversion for waste-heat recovery from automotive radiator and exhaust systems.

Thermoelectric energy conversion also finds use in solid-state refrigerators. These low-maintenance devices can be applied to cool, e.g., electronic components without expanding gases or moving parts.

The coupled electrical and thermal transport properties of thermoelectric materials enable the direct conversion of heat into electricity. The best available thermoelectric materials are doped semiconductors such as Bi_2Te_3, PbTe, and $Si_{1-x}Ge_x$.[12, 13, 14, 15] However, applications of these materials are limited to specialized devices (e.g., deep-space power generation) because their efficiency is low compared to heat engines. Moreover, they contain either rare (e.g., Te) or toxic (e.g., Pb) elements, which impedes large-scale applications. New thermoelectric materials with superior performance will facilitate the adoption of waste-heat recovery technology and mitigate the impact of fossil fuels on the environment. Ongoing research efforts at the University of Michigan and elsewhere aim to discover new thermoelectric compounds, alloys, and nanostructures with enhanced thermoelectric performance.[16, 17] The thermoelectric efficiency, which is measured by the dimensionless figure of merit, is not easy to maximize because optimizing one physical parameter that affects it often adversely affects another. Therefore, the computational work based on predictive methods is essential to guide the discovery of good thermoelectric materials composed of earth-abundant elements.

1.2 Methodology

High-performance-computing calculations have become an indispensable toolbox in materials research. Atomistic calculations based on density functional theory (DFT) and many-body perturbation theory (MBPT) enable the predictive theoretical characterization of materials properties without empirical or adjustable parameters. Advances in software development and supercomputing hardware enabled the application of DFT and MBPT to predictively investigate a broad range of materials and phenomena, including quantum processes in materials such as free-carrier absorption, Auger recombination, and thermoelectric transport[18, 19, 20], novel wide-gap semiconductors for power electronics and UV photonics[21, 22, 23], silicon nanostructures for optimal light absorption in the visible range[24], 2D optoelectronic materials[25, 26, 27], atomistic understanding of resistive switching materials[28, 29], and the theoretical characterization of experiementally measured materials properties[30, 31, 32, 33, 34].

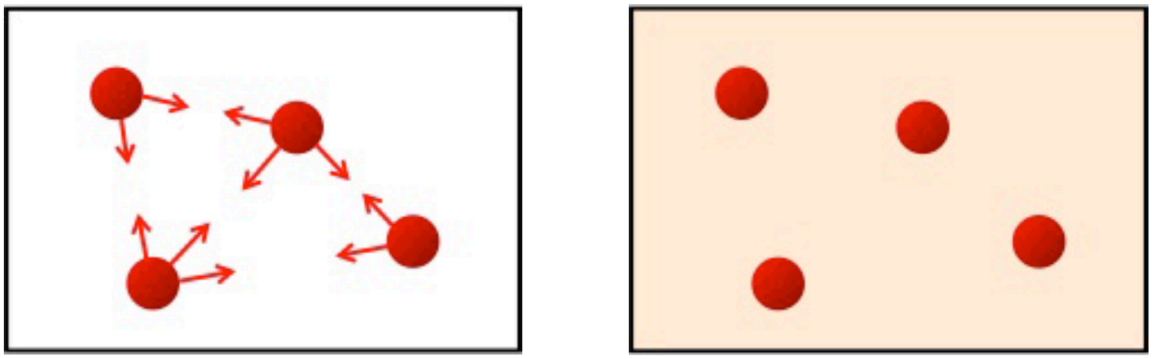

Figure 1.1: The original many-body problem of interacting electrons in a static external potential is reduced to a problem of non-interacting electrons moving in an effective potential.

1.2.1 Density functional theory

First-principles calculations of electronic and optical properties start directly at the level of established microscopic laws of quantum physics at the atomic level, without assumptions such as empirical models and adjustable parameters fitted to experimental data. Electrons in solids form an interacting many-body quantum system moving in the static ionic potential of the nuclei. To solve for the wave functions and eigen-energies of the many-body electron system in a brute-force way, one needs to determine the interacting many-body wave function taking all electron interactions into account, which is computationally prohibitive even on modern supercomputers even for systems with as few as 10 electrons. An elegant solution to this problem was made possible with the development of density functional theory (DFT), in which the properties of a many-electron system can be determined by a universal functional of the spatially dependent electron density. Because of its satisfactory accuracy in the treatment of solid-state systems and ita relatively low computational cost compared to wave-function-based methods, such as Hartree-Fock and higher-order techniques, DFT is established as one of the most popular and versatile methods in computational materials physics to determine phase stability, structural properties, bond and surface energies, phase diagrams, and kinetic barriers.

The theoretical footing of DFT is established by the HohenbergKohn theorem[35], which demonstrates that the ground state properties of a many-electron system are uniquely determined by its electron density that depends only on the three spatial coordinates. The Kohn-Sham method[36] reduces the many-body problem of interacting electrons in a static external potential to a fictitious problem of non-interacting electrons moving in an effective potential, the Kohn-Sham potential, as shown in Figure 1.1, whose solution gives the same electron density as the original interacting problem. In practice, the exact universal func-

tional that incorporates all effects of electron exchange and correlation is approximated by analytical expressions. Popular choices for the exchange-correlation functional are local versions such as the local density approximation (LDA),[37] which assumes that the electron gas is locally uniform and its exchange-correlation energy is given by the results of quantum Monte-Carlo calculations[38], or the generalized gradient approximation (GGA), e.g., in the Perdew-Burke-Ernherhoff parameterization (PBE),[39] which also incorporates the gradient of the density. Effectively, the Kohn-Sham theorem reduces the interacting N-particle problem to N one-particle problems. The cost of DFT using a local exchange-correlation functional is therefore lower than the Hartree-Fock method and similar to the cost of the Hartree method. For practical DFT calculations, several more approximations and implementation choices need to be made regarding the interaction of valence electrons with core electrons (e.g., all-electron or pseudopotential DFT), the basis set (e.g., plane waves, real-space grids, or numerical atom-centered orbitals), the boundary conditions of the simulation box (periodic boundary condictions or vanishing wave function at the boundary), etc. Several codes exist that implement different versions of DFT, such as Quantum-Espresso or VASP.[40, 41]

1.2.2 Quasiparticle corrections and the GW method

DFT is, in principle, an exact theory to reproduce and predict ground-state properties, such as the total energy and atomic structure, but it is not a theory to address excited state properties, such as the band structure and optical excitation energies. The problem arises when an electron is added to the system of interacting electrons. This electron interacts with the surrounding electrons via the screened Coulomb interaction and the combination of the electron and the cloud of the disturbed neighboring electrons behaves effectively like a new particle with renormalized properties called a quasiparticle. A solution to this problem is achieved with many-body perturbation theory in the GW approximation. The approximation is that the self-energy Σ is expanded in a formal Taylor series in terms of the single-particle Green's function G and the screened Coulomb interaction W and the lowest order term is kept in the expansion[42, 43]. The GW method has been shown to provide more accurate results for band structures than DFT and local exchange-correlation funcitonals. While DFT within LDA or PBE underestimates band gaps systematically, the GW approximation provides band gaps of insulators and semiconductors in much better agreement with experiment[44], as shown in Figure 1.2. The GW method is implemented in the BerkeleyGW software package.[1]

The GW approximation provides accurate description of electronic structures but it is

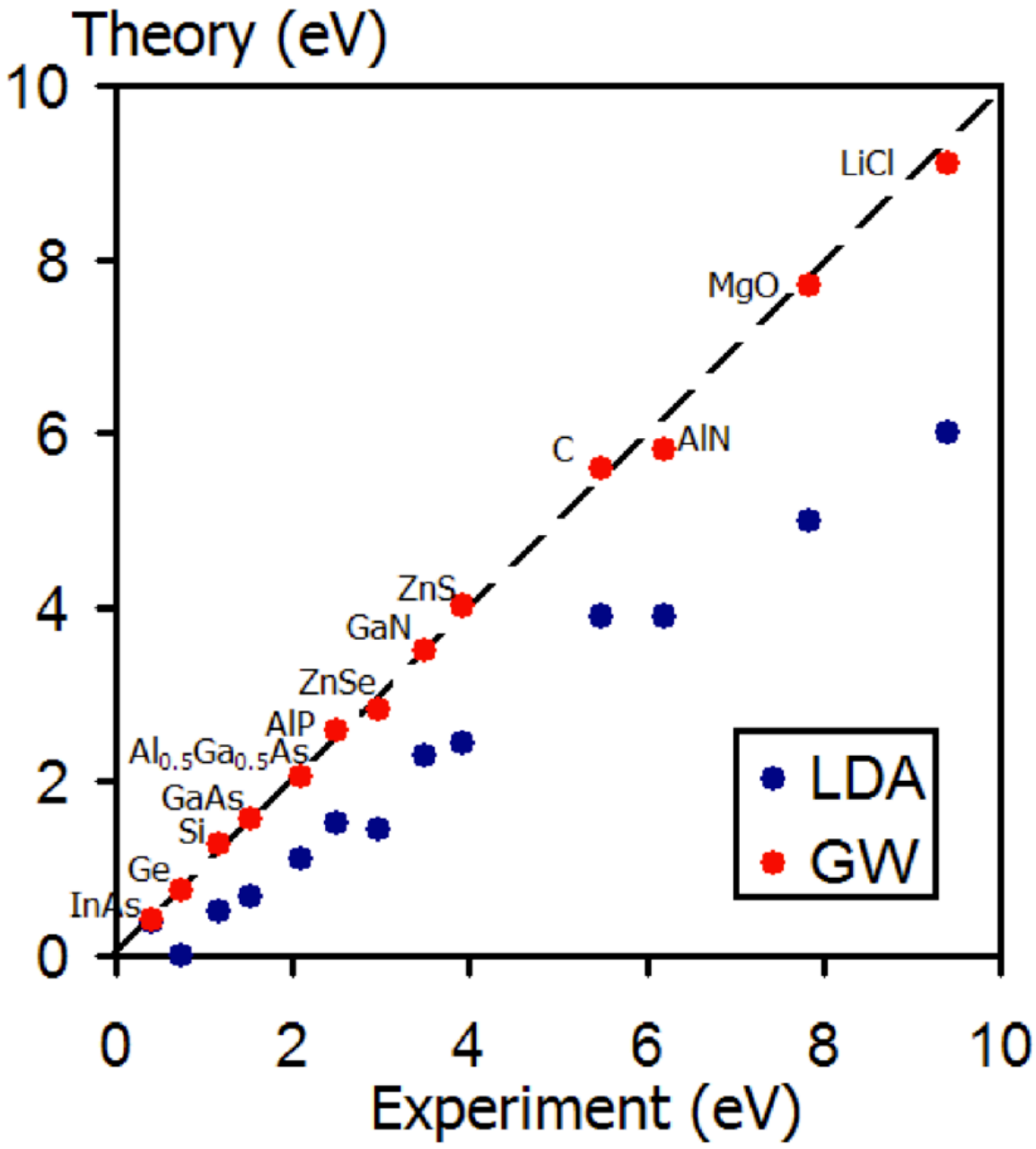

Figure 1.2: The GW approximation seems to provide band gaps of insulators and semiconductors in agreement with experiment, and hence to correct the systematic DFT underestimation.

a one-particle-excitation theory and thus not sufficient to obtain correct optical properties, which are two-particle excitations. Optical spectra of semiconducting materials are strongly affected by the attractive interaction between the photo-excited electron in the conduction band and the hole that it leaves behind in the valence band. This electron-hole interaction creates new bound states with excitation energies below the gap known as excitons. To describe excitonic effects, one should switch from a one-particle formalism to a two-particle theory by solving the Bethe-Salpeter Equation (BSE)[45]. An example absorption spectrum for silicon computed at the GW and GW-BSE levels is shown in Figure 1.3. The calculated spectrum is found to have good agreement with experiment only when both the quasiparticle effects within the GW approximation and the excitonic effects are included. The careful treatment of excitonic effects is particularly important for quantum-confined structures such as nanowires[46, 47, 21] where quantum-confinement effects additionally increase the exciton binding energy and shift the onset of optical absorption to lower energies.

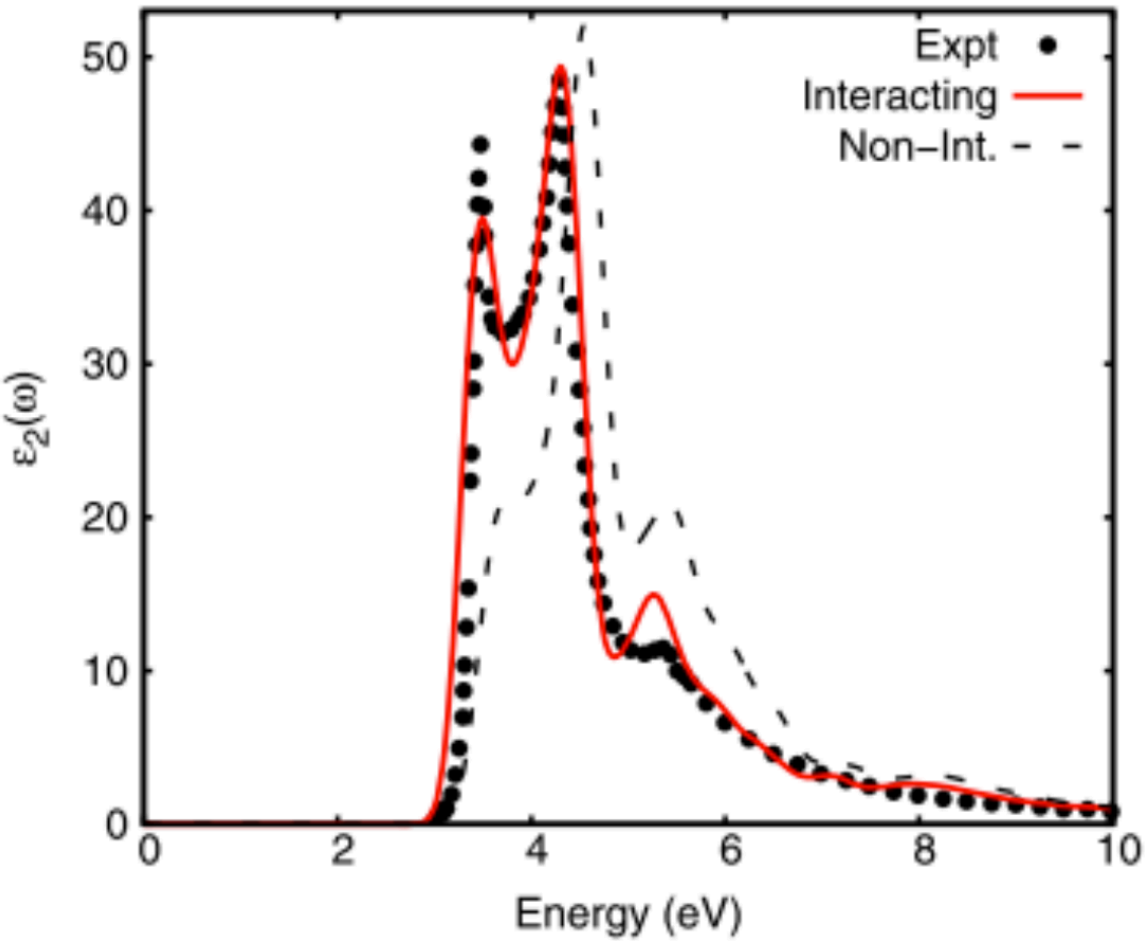

Figure 1.3: The absorption spectra for silicon calculated at the GW (black dashed) and GW-BSE (red solid) levels using the BerkeleyGW package[1] compared to that from experiment[2].

CHAPTER 2

Nanoporous Silicon for Solar-Cell Applications

Bulk silicon is a poor light emitter and absorber, but its optical properties are significantly enhanced by nanostructuring. We use first-principles calculations to investigate the electronic and optical properties of nanoporous silicon. We determine and analyze the electronic structure, optical coefficients, and photovoltaic conversion efficiency as a function of pore size and spacing. Our results show that the visible-range absorption coefficient of nanoporous Si is greatly improved compared to the bulk for pore spacings and sizes on the scale of a few nanometers. The photovoltaic efficiency is improved to up to 2.7 times compared to bulk Si and the theoretical maximum conversion efficiency reaches up to 6.3% for a thin-film nanoporous material thickness of 135 nm. Our results show that nanoporous Si is a promising material for thin-film photovoltaic applications.

Silicon is an earth-abundant material of great importance in semiconductor electronics such as integrated circuits and solar cells. However, Si is an indirect-gap semiconductor and optical transitions across its minimum gap require the assistance of phonons.[48] This results in a low absorption coefficient in the visible range and increases the material thickness and cost for photovoltaic applications. The indirect band gap of bulk Si also makes it an inefficient light emitter and precludes its applications for active optoelectronic components. Increasing the light absorption and emission in Si could extend the already established Si manufacturing technology into optoelectronics and has been an area of intense research activity.

Nanostructuring is a promising approach to engineer the optical properties of Si and increase the efficiency of thin-film Si solar cells. Pattering the surface of Si with nanopores of 220 nm diameter has been demonstrated to reduce the surface reflection to less than 5% and increase optical absorption in the visible range.[49] Moreover, Si nanowires with a diameter of 390 nm increase the optical path length in thin-film solar cells by up to a factor of 73 and deliver efficiencies above 5%.[50] Similar Si nanowire array geometries have been found to suppress reflectivity and improve absorption in the visible range.[51, 52] The structural features of the above-mentioned Si nanostructures are on the order of 100 nm, which is comparable to the wavelength of visible photons and therefore has a strong effect on wave propagation and reflection in solar cells made of these nanostructures. However, nanostructures of this scale do not exhibit strong quantum confinement and the fundamental electronic properties of Si (e.g., band gap, exciton binding energy, optical matrix elements) are not affected significantly compared to the bulk. Nanostructuring with pores of 60 nm diameter has been demonstrated to enable optical gain and stimulated emission in nanoporous crystalline Si, but this is attributed to recombination at A-center defects.[53]

Si nanostructures with features on the scale of a few nanometers are strongly affected by quantum confinement and their optical absorption and emission properties can be significantly enhanced compared to the bulk. Besides increasing the band gap, quantum confinement breaks the momentum-conservation requirement along the confinement direction and increases the probability of optical transitions across the indirect band gap. Nanostructuring can thus enable the emission of visible light from Si.

Visible photoluminescence at room temperature has been reported for Si quantum wire arrays with features on the 5-nm scale.[54]

Luminescence has also been reported in 1-nm wide Si nanoparticles that can be tailored through modification of the surface chemistry.[55] Moreover, highly efficient and color-tunable visible LEDs have been fabricated with Si nanocrystals with a size between 1 and 2 nm.[56]

Previous theoretical work has examined the electronic and optical properties of a range of nanometer-sized Si nanostructures. Van de Walle and Northrup investigated the electronic properties of Si-based layered structures using first-principles methods.[57] They found that a two-layer Si structure has a direct band gap and a strong direct transition between the band-edge states. Hybertsen studied the phonon-assisted and zero-phonon transitions in Si nanostructures and found that phonon-assisted processes dominate optical transitions for nanofeature sizes above 1.5 to 2 nm.[58] A genetic algorithm was employed by d'Avezac *et al*. to search for all possible Si/Ge superlattices and found one specific configuration with a direct band gap and a strong dipole-allowed transition.[59] Direct band gaps were also observed by Peelaers *et al*. for Si/Ge core-shell nanowires with a diameter of 1.2 to 1.6 nm[60] and by Yang *et al*. for Si nanowire with a diameter of 1.2 nm.[46] Moreover, a large exciton binding energy (0.8-1.1 eV) was reported by Yang *et al.*[46] and by Bruno *et al.*[47] for Si nanowires with a diameter less than 2 nm. The strong excitonic effects in these nanostructures are attributed to the enhanced electron-hole interaction due to the quantum confinement. This body of theoretical work provides strong evidence that Si nanostructures with characteristic features on the order of a few nanometers are very promising for optoelectronic applications.

Nanoporous Si presents the advantage that the pores introduce quantum confinement and carrier scattering only in two of the three spatial dimensions. Thus, nanopores cause the scattering of electrons by the pore sidewalls and enable the absorption of light with polarization perpendicular to the pore direction. However, at the same time nanopores do not strongly affect carrier scattering or the carrier mobility along the pore direction, and thus allow for high carrier-extraction efficiency. As a result, thin-film nanoporous Si may overcome the stability and efficiency limitations of disordered hydrogenated amorphous Si, which suffers from the detrimental Staebler-Wronski effect.[61]

In this work we present and analyze the electronic and optical characteristics of nanoporous Si with nanoscale patterns on the order of a few nanometers. Quantum confinement by the nanopores increases the band gap and enhances carrier scattering, thus improves the optical absorption that is desired in solar-cell applications. We show that nanoporous Si can exhibit simultaneously improved absorption, reduced reflectivity, and increased photovoltaic conversion efficiency compared to bulk Si. Our results indicate that the photovoltaic efficiency of nanoporous Si can be improved by up to 2.7 times compared to the bulk for a film thickness of 135 nm and that the maximum absolute conversion efficiency in nanoporous Si can reach up to 6.3%. Therefore, nanoporous Si thin films can have a higher photovoltaic conversion efficiency than thin-film bulk Si and a substantially increased efficiency to material cost ratio than commercial bulk Si solar cells, and could be applied to develop low-cost and

flexible Si solar cells with an appreciable efficiency. This work has been published in ACS Photonics.[24]

2.1 Methodology

We studied the electronic and optical properties of nanoporous Si using first-principles calculations based on density functional theory (DFT) and many-body perturbation theory. We performed DFT calculations to obtain the ground-state charge density and electronic wave functions using the local-density approximation[38, 62] for the exchange-correlation potential. We used the plane-wave pseudopotential method[63] with a plane-wave cutoff of 16 Ry and norm-conserving pseudopotentials[64] as implemented in the Quantum-ESPRESSO code[40]. We calculated the quasiparticle band energies of nanoporous Si using the one-shot GW method[65] and the BerkeleyGW code[1]. The static dielectric function was calculated with a 7 Ry plane-wave cutoff and extended to finite frequency using the generalized plasmon-pole model of Hybertsen and Louie[65]. The Coulomb-hole self-energy term was calculated using a sum over three times as many unoccupied bands as occupied bands using the static-remainder approach[66]. The dielectric function was calculated using all occupied bands and unoccupied bands up to 7.5 eV above the valence-band maximum. The quasiparticle energies of the nanoporous Si structures with L=$3a_{\mathrm{Si}}$ were calculated with a $2\times2\times4$ Monkhorst-Pack[67] mesh while the other structures with larger unit cells were studied with a $1\times1\times4$ Monkhorst-Pack mesh. We also used the Bethe-Salpeter equation formalism[45] to study two-particle excitations and calculate the optical absorption and reflectivity spectra including excitonic effects. Excitonic effects on the optical absorption spectra have only been considered for the three examined structures *A*, *B*, and *C* with the smallest pore spacing ($L = 3a_{\mathrm{Si}}$) due to the high computational expense of Bethe-Salpeter calculations for larger structures.

2.2 Results and Discussion

2.2.1 Structure

Figure 2.1 shows some of the nanoporous Si structures examined in this work. The structural models were constructed by perforating bulk Si with nanoscale pores of radius *R* and spacing *L* along the [001] direction. Although hexagonal pore patterns are encountered experimentally, we considered a square-lattice distribution of pores because the hexagonal lattice is incommensurate with the symmetry of the (001) surface of Si and results in too

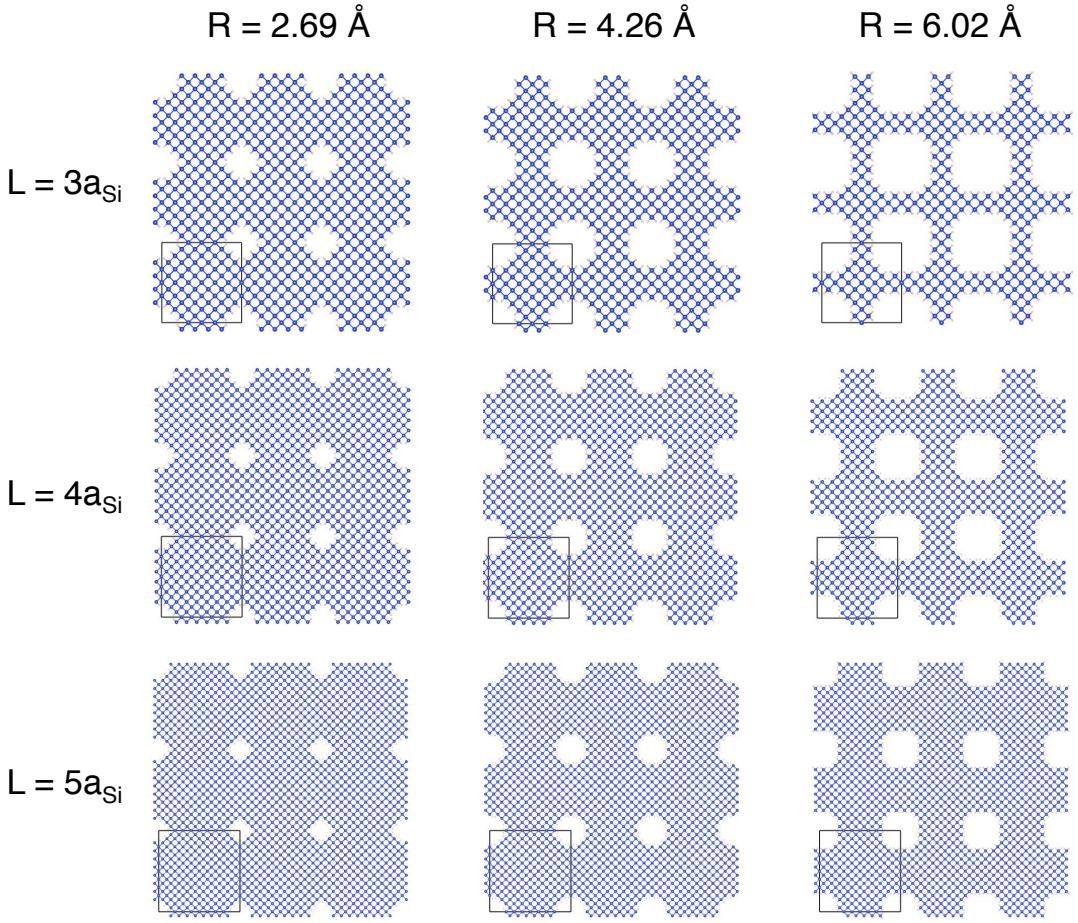

Figure 2.1: Some of the nanoporous Si structures with various pore radius R and pore spacing L examined in this work. Quantum confinement by the nanoscale pores increases the probability of optical transitions across the band gap of Si and enhances the absorption coefficient in the visible range.

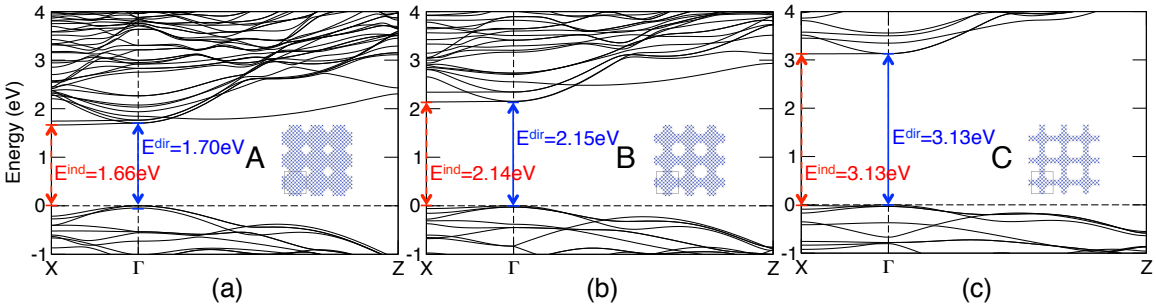

Figure 2.2: The band structures of three of the investigated nanoporous Si structures (*A*, *B*, and *C* shown in the insets).

large simulation cells. We expect that a hexagonal pore arrangement yields similar results to the investigated square pore arrangement for the electronic and optical properties and the photovoltaic efficiency enhancement as a function of pore size and spacing. We investigated a total of 20 nanoporous Si structures with pore spacing up to six times the lattice constant of the conventional unit cell of bulk Si (a_{Si} = 5.43 Å) and pore radius ranging from 2.7 to 13.5 Å. The Si dangling bonds on the nanopore surfaces were passivated with H atoms to eliminate mid-gap defect states that contribute to nonradiative recombination. Chemical passivation by oxygen[68], methyl[69] (CH_3), and halogen[70] is used in practice to eliminate surface dangling bonds in porous Si and Si nanowires for higher ambient stability. The nanoporous Si systems we studied are all intrinsic. The additional screening and free-carrier absorption by free carriers are weak at typical solar irradiation conditions and are not expected to affect the calculated results. We studied nanostructures containing up to 300 atoms in the periodic cell, and GW calculations for the largest simulations cells required up to 10,000 CPU hours. All structures were relaxed to minimize the stress and the forces on the atoms.

2.2.2 Band structure

Figure 2.2 shows the band structures of three nanoporous Si structures [*A* ($L = 3a_{\mathrm{Si}}$, $R = 2.69$ Å), *B* ($L = 3a_{\mathrm{Si}}$, $R = 4.26$ Å), and *C* ($L = 3a_{\mathrm{Si}}$, $R = 6.02$ Å)] along the in-plane (Γ–X) and out-of-plane (Γ–Z) directions.

These three structures have the same pore spacing but different pore radii. As the pore size increases, the band gap widens from 1.66 eV to 3.13 eV due to increasing quantum confinement. The band gap of structures *A* and *B* is indirect with the valence-band maximum located at the Γ point and the conduction-band minimum located at the X point. The difference between the minimum direct and the indirect gap, however, decreases to below 1 meV for structure *C* and thus direct transitions also contribute to optical absorption near the onset for this structure. Since the conduction-band minimum of bulk Si is located at a point between Γ and X, the shift of the conduction-band minimum in nanoporous Si is attributed to band structure distortion by the introduction of nanopores. The lowest conduction band gets flatter along the quantum-confined direction as the pore radius increases and becomes almost horizontal for structure *C*.

The band gap of nanoporous Si as a function of pore radius and spacing is shown in Figure 2.3. Most structures are found to have quasi-direct band gaps and are marked with solid symbols in Figure 2.3. The band gaps tend to be quasi-direct for large pore spacing, which is the case for most examined structures with $L = 5a_{\mathrm{Si}}$ or $L = 6a_{\mathrm{Si}}$. This is explained

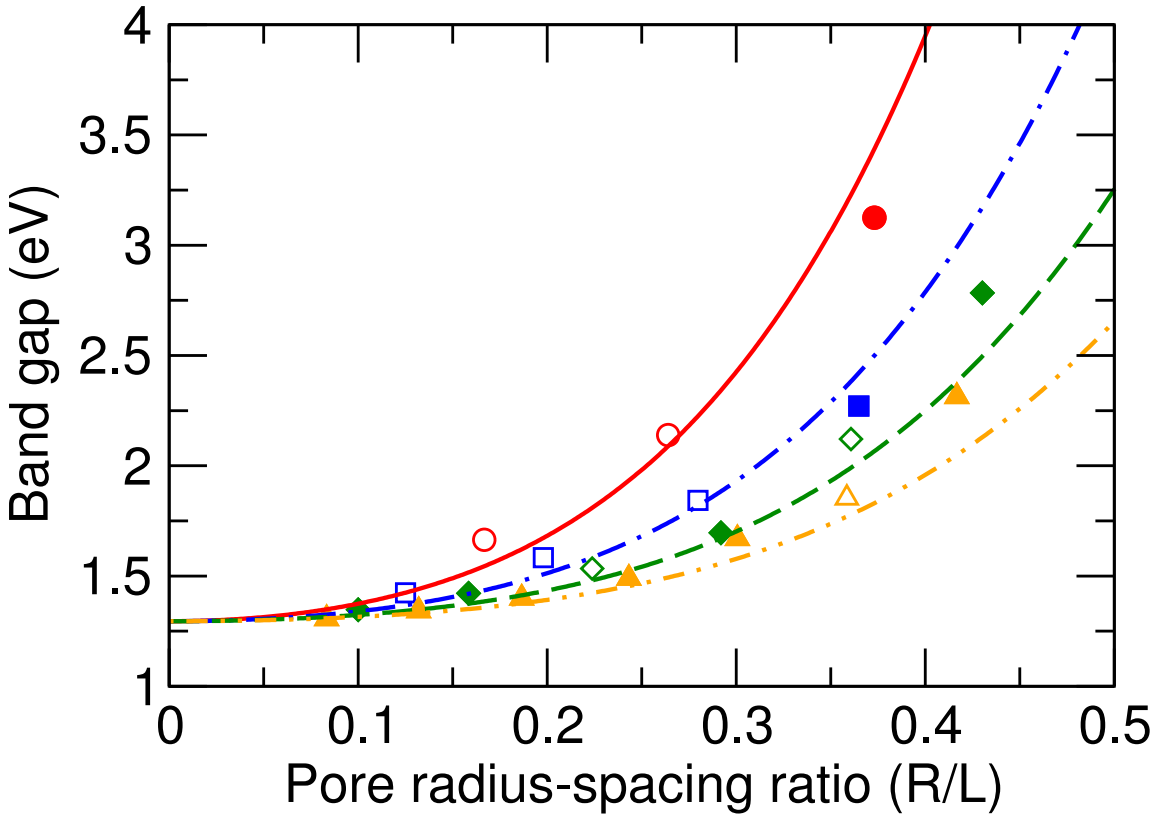

Figure 2.3: Band-gap values of nanoporous Si as a function of pore radius and spacing. The lines are fits to the calculated data. The structures with direct band gaps are marked with solid symbols.

by the multiple folding of the Brillouin zone along the quantum-confined direction. The gap is also more likely to be quasi-direct for structures with large pore size, a trend already analyzed for structures *A*, *B*, and *C*. The band-gap values were fitted as a function of pore radius R and spacing L according to:

$$E_{\text{gap}}(R, L) = E_{\text{gap}}^{\text{bulk}} + \frac{1}{L^2} f\left(\frac{R}{L}\right) \tag{2.1}$$

where the calculated band gap of bulk Si, $E_{\text{gap}}^{\text{bulk}}$, is 1.295 eV (which is within the typical 0.1 eV accuracy of the computational method compared to the experimental value of 1.17 eV at 0 K [71]), and $f(x)$ is a shape-dependent term representing different levels of confinement for different values of the R/L ratio that was found to be $f(x) = (1923x^2 + 14976x^4)$ eV Å^2 .

2.2.3 Optical matrix elements

Though most nanoporous structures with large pore spacings have a quasi-direct band gap, the transition probability across these gaps are small compared to typical direct-gap transitions. Figure 2.4 shows the average optical (velocity) matrix elements of interband transitions between states within 100 meV from the band edges at the Γ point for light polarized perpendicular to the pore direction. The optical matrix elements for all examined structures are smaller than the typical value for the direct allowed transition in bulk Si at the Γ point and for most structures they are also smaller than the typical indirect (phonon-assisted) optical transition matrix elements of bulk Si (Figure 2.4). Therefore, the reported direct gaps of Figure 2.3 are quasi-direct since they are associated with small transition probabilities. Only the matrix elements for the smallest pore spacing ($L = 3a_{\text{Si}}$) are larger than the characteristic value of phonon-assisted transitions. This is in agreement with the earlier work of Hybertsen,[58] who found that phonons are the dominant carrier-scattering mechanism that mediates optical transitions in Si for nanoscale features larger than 1.5 to 2 nm. The transition probability across the band gap is largest when quantum confinement is strongest (large pore radius and small pore spacing) and decreases with decreasing degree of quantum confinement. In the limit of small pore size and large pore separation the matrix elements approach zero, since this is the limit of the transition across the indirect gap of bulk Si, which is forbidden without the assistance of phonons.

2.2.4 Dielectric constant

The dielectric constants of all studied nanoporous Si structures are summarized in Figure 2.5. Screening is enhanced for increasing Si volume fraction. The first-principles results are in good agreement with both the 2D Bruggeman nonsymmetric model[72]

$$f_{\text{Si}} = \frac{1 - \epsilon_{\text{eff}}}{1 - \epsilon_{\text{Si}}} \left(\frac{\epsilon_{\text{Si}}}{\epsilon_{\text{eff}}} \right)^{\frac{1}{2}}, \tag{2.2}$$

and the 2D Maxwell-Garnett model[73]

$$\frac{\epsilon_{\text{eff}} - \epsilon_{\text{Si}}}{\epsilon_{\text{eff}} + \epsilon_{\text{Si}}} = (1 - f_{\text{Si}}) \frac{1 - \epsilon_{\text{Si}}}{1 + \epsilon_{\text{Si}}}, \tag{2.3}$$

where ϵ_{Si} and ϵ_{eff} are the dielectric constants of bulk and nanoporous Si, respectively. The 2D Maxwell-Garnett model considers vacuum cylinder inclusions in a matrix of bulk Si, while the 2D Bruggeman model treats both Si and vacuum as cylindrical inclusions in a theoretical effective medium. The Bruggeman model is thus an extension to the Maxwell-

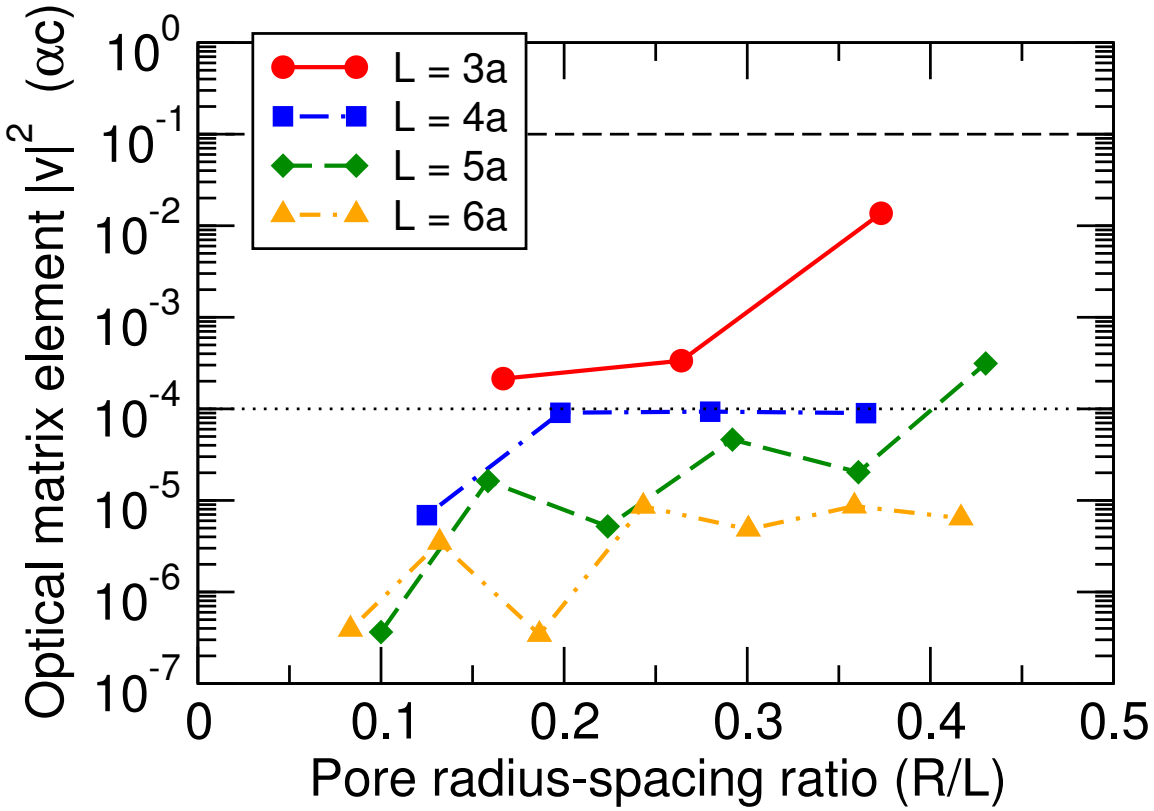

Figure 2.4: Average optical (velocity) matrix elements of interband transitions between the states within 100 meV from the band edges of the investigated nanoporous Si structures at the Γ point for light polarized perpendicular to the pore direction. The optical matrix elements are given in units of αc, where α is the fine-structure constant and c is the speed of light. The horizontal dashed line indicates the typical value of direct optical transition matrix elements across the direct gap of bulk Si at the Γ point, while the dotted line denotes the characteristic value of indirect (phonon-assisted) optical matrix elements across the indirect gap of bulk Si.

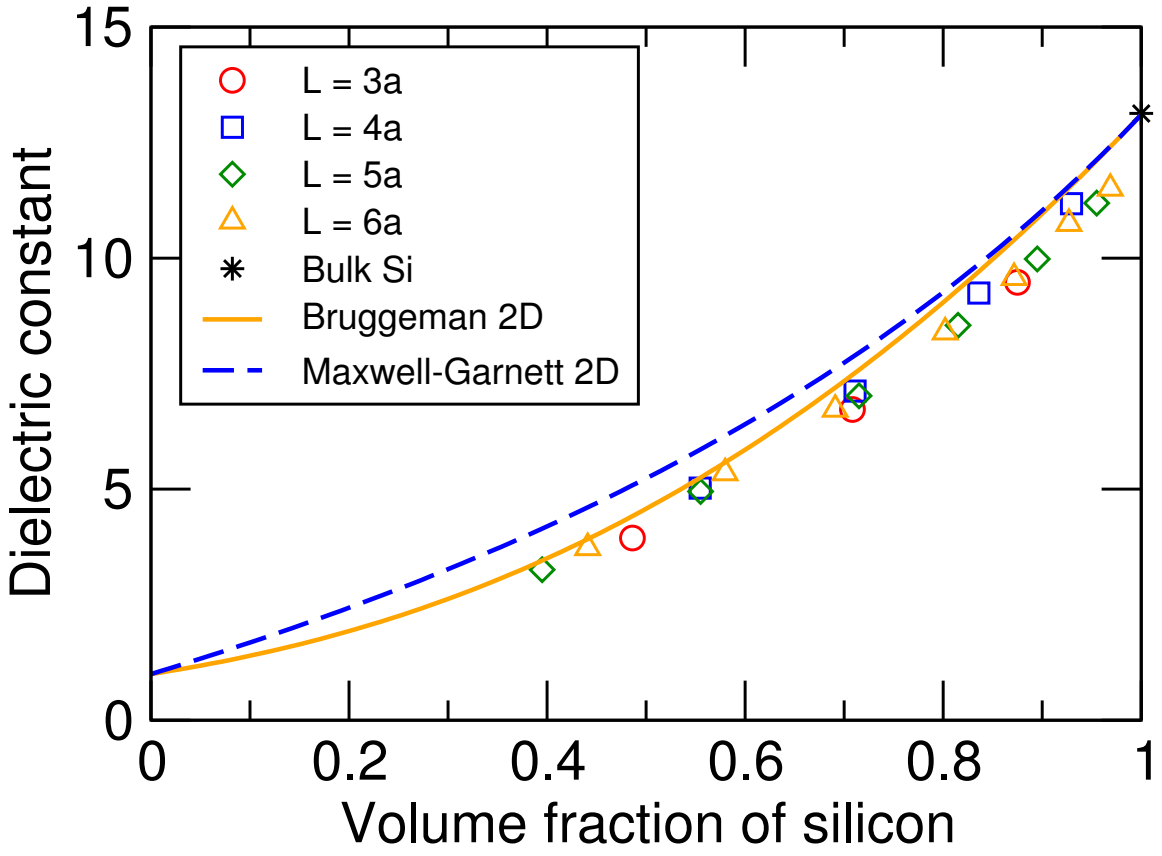

Figure 2.5: The dielectric constant of nanoporous Si as a function of Si volume fraction for various pore geometries. The data are in very good agreement with both the Bruggeman formula (solid) and the Maxwell-Garnett formula (dashed).

Garnett model.[74] Our first-principles results show that both models are similarly valid in describing the dielectric constant of porous Si at the nanoscale.

2.2.5 Optical properties

To understand the effect of quantum confinement on the optical properties of nanoporous Si we examine the real (ϵ_1) and imaginary (ϵ_2) parts of the dielectric function for structures *A* and *B* and compare it to the dielectric function of bulk Si (Figure 2.6). A Gaussian function with a width of 0.15 eV was used to account for the broadening of the optical spectra. For the purposes of this analysis, only direct optical transitions (no phonon-assisted absorption) across the direct gap of bulk Si have been included in Figure 2.6. The two nanoporous Si structures have the same pore spacing but different pore radii. Structure *A* has larger ϵ_1 than structure *B* and is closer to bulk Si (Figure 2.6a). This is because structure *A* exhibits stronger screening effects than structure *B* due to its higher Si volume fraction. The imaginary part curves (Figure 2.6b) show that the direct absorption edges for both examined nanoporous Si structures occur at lower energies (1.70 eV for structure *A* and 2.15 eV for structure *B*, Figure 2.2) than the first direct optical transition of bulk Si (3.4 eV [75]), which indicates that scattering of electrons by the nanopores enables quasi-direct optical transitions across the band gap. The refractive index n and the extinction coefficient κ are determined from ϵ_1 and ϵ_2 using

$$n(E) = \frac{1}{\sqrt{2}}\sqrt{\epsilon_1(E) + \sqrt{\epsilon_1^2(E) + \epsilon_2^2(E)}}, \tag{2.4}$$

and

$$\kappa(E) = \frac{1}{\sqrt{2}}\sqrt{-\epsilon_1(E) + \sqrt{\epsilon_1^2(E) + \epsilon_2^2(E)}}, \tag{2.5}$$

where E is the photon energy. The reflectivity and absorption coefficient were calculated from n and κ by

$$R(E) = \frac{(n-1)^2 + \kappa^2}{(n+1)^2 + \kappa^2}, \tag{2.6}$$

and

$$\alpha(E) = \frac{4\pi\kappa}{hc/E}, \tag{2.7}$$

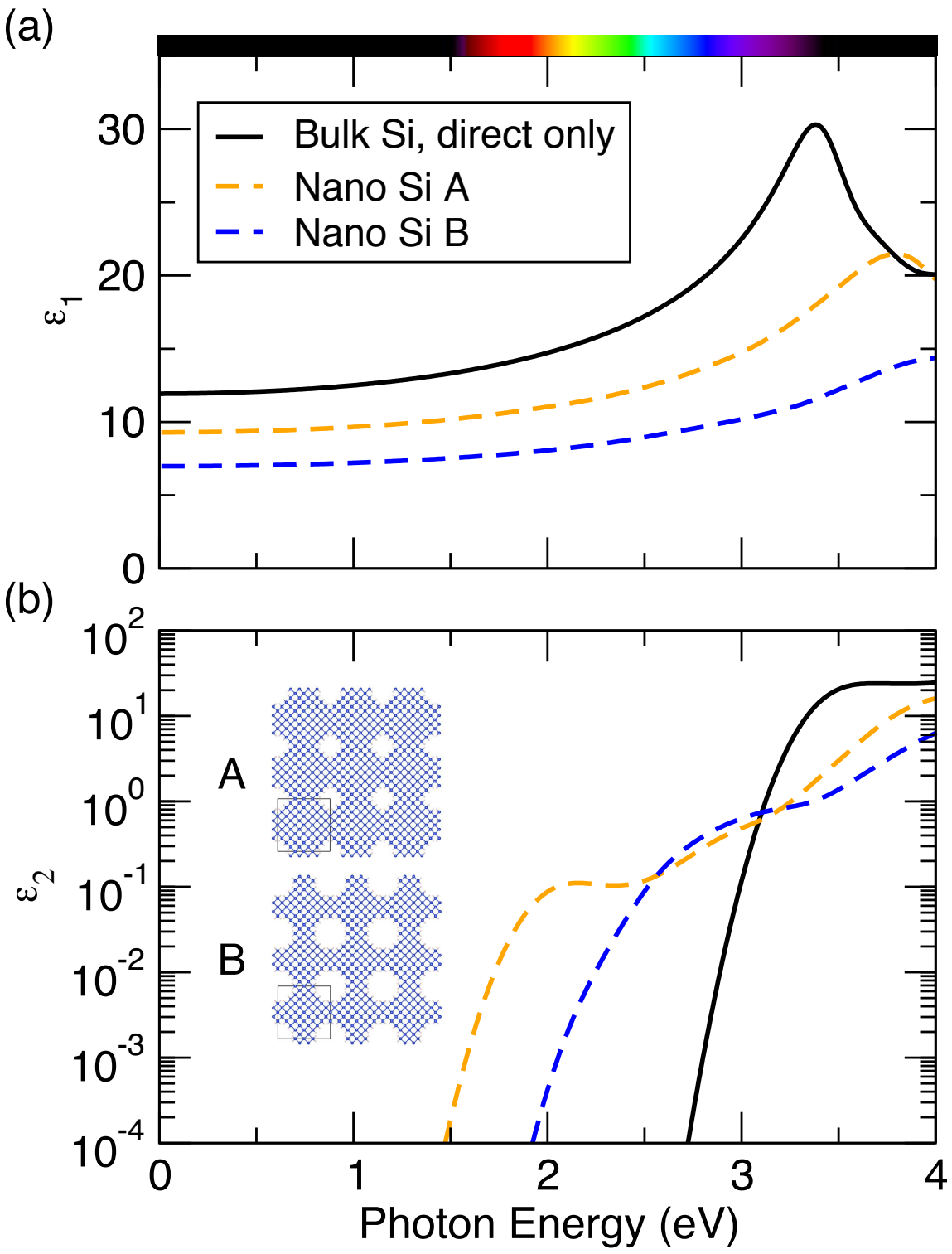

Figure 2.6: Dielectric functions of structures *A* and *B* compared to bulk Si. (a) real part (ϵ_1) and (b) imaginary part (ϵ_2). Electron scattering by the nanoscale pores enable optical transitions across the gap in structure *A* and *B*. Only direct optical transitions are considered for bulk Si (no phonon-assisted transitions) and only direct and quasidirect transitions are included for the nanostructures to highlight the additional absorption due to the quasidirect transitions in nanoporous Si.

and are shown as a function of photon energy for nanoporous Si structures *A* and *B* in Figure 2.7. Structure *B* shows lower reflectivity (Figure 2.7a) and larger optical gap (Figure 2.7b) than structure *A* and bulk Si[4] because of its lower Si volume fraction and stronger quantum confinement. Strong confinement in structure *B* also leads to stronger pore-electron scattering, which gives higher electron transition probability and absorption coefficient than both structure *A* and bulk Si in the 2.3–3.2 eV energy range (Figure 2.7b). We note that we did not include phonon-assisted optical transitions for nanoporous Si, which would increase the absorption even further.

2.2.6 Excitons

We studied excitonic effects in nanoporous Si arising from the electron-hole interaction. Excitonic effects have been shown by first-principles calculations to modify the optical coefficients of bulk Si due to the coherent coupling of different electron-hole configurations[76, 45]. In quantum-confined structures such as nanowires[46, 47, 21] excitonic effects additionally increase the exciton binding energy and shift the onset of optical absorption to lower energies.

Structure *B* has a larger exciton binding energy (0.23 eV) than structure *A* (0.13 eV) since the increased quantum confinement enhances the strength of the electron-hole interaction (Figure 2.7b). Though the exciton binding energy of the examined nanoporous structures *A* and *B* is increased by an order of magnitude compared to bulk Si (15 meV)[45] it is one order of magnitude smaller than that of Si nanowires with comparable confinement radius (0.8-1.1 eV) determined from theoretical predictions.[46, 47] This is attributed to the weaker quantum confinement in nanoporous Si than nanowires since the Si regions are connected in the nanoporous geometry and have a larger confinement volume for the same linear confinement dimension (Figure 2.1).

2.2.7 Photovoltaic conversion efficiency

Our predictive results can be applied to answer whether nanopores can improve the photovoltaic conversion efficiency of thin-film Si solar cells and to identify promising nanoporous Si structures for photovoltaic applications. The calculated reflectivity and absorption coefficient are two important factors that affect the photovoltaic conversion efficiency, defined as the fraction of solar energy converted to electrical power per unit area of material. The electrical power density is calculated by integrating the converted spectral irradiance over

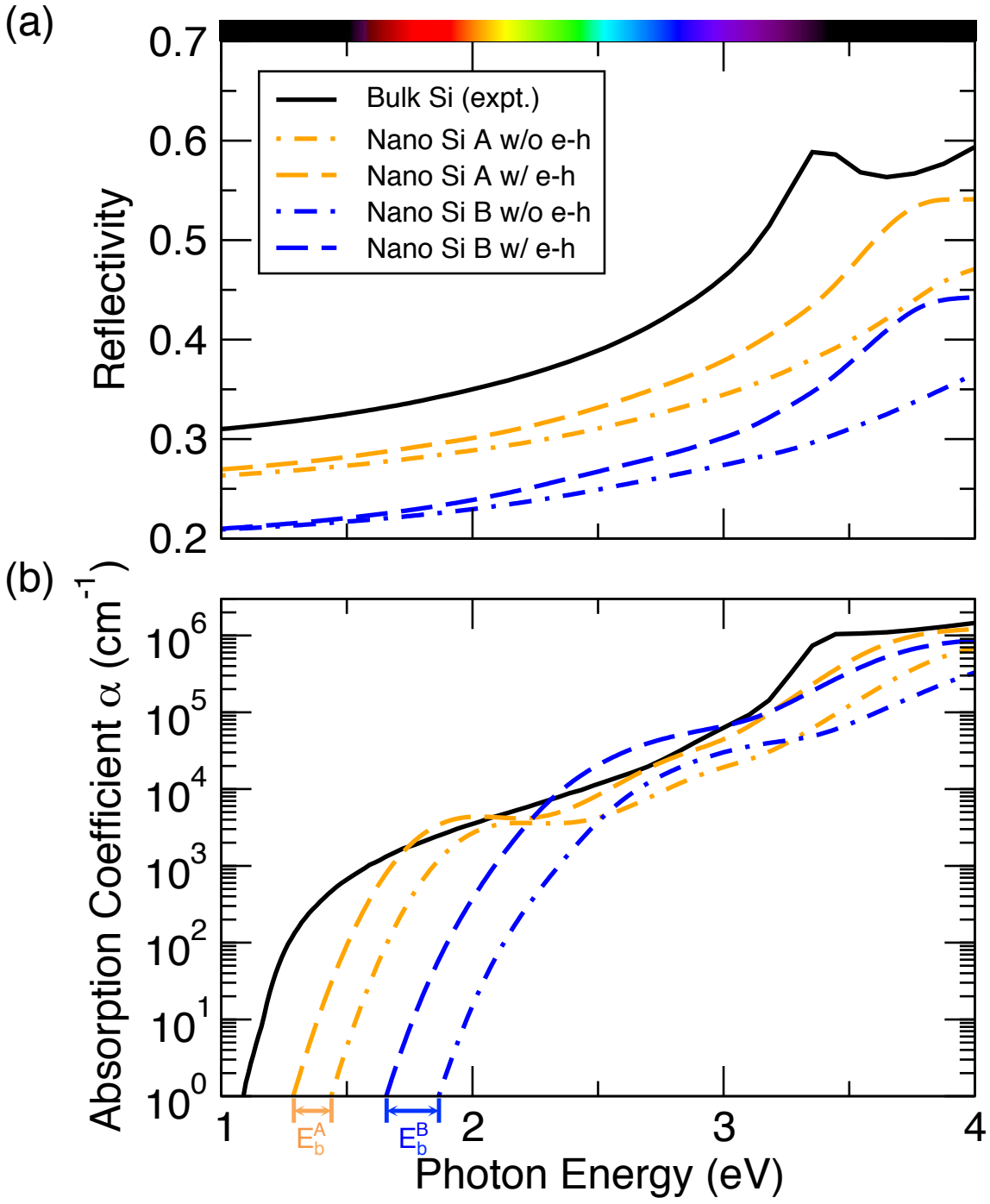

Figure 2.7: (a) Reflectivity and (b) absorption coefficient of nanoporous Si structures *A* and *B*. Dashed lines include excitonic effects due to electron-hole (e-h) interaction, while dash-dot lines do not include excitonic effects. The calculated results are also compared to the experimental data for bulk Si.

the solar-spectrum wavelengths

$$P = \int_0^{\lambda_{\text{max}}} W(\lambda)[1 - R(\lambda)]A(\lambda)C(\lambda)\,\mathrm{d}\lambda, \tag{2.8}$$

where λ is the photon wavelength, λ_{max} is the longest wavelength that can be absorbed by the nanostructure and is determined by the direct band gap of the nanoporous Si structure,

$$\lambda_{\text{max}} = \frac{hc}{E_{\text{g}}^{\text{dir}}}, \tag{2.9}$$

and $W(\lambda)$ is the solar spectral irradiance at Air Mass 1.5.[77] The term $R(\lambda)$ is the reflectivity of the front surface of the material and the absorbance $A(\lambda)$ is given by

$$A(\lambda) = 1 - \mathrm{e}^{-\alpha(\lambda)d} \tag{2.10}$$

where d is the thickness of the material. The term $C(\lambda)$ is a conversion factor to account for the fraction of the photon energy converted to electronic energy (i.e., to the excitation energy of one electron-hole pair across the minimum band gap),

$$C(\lambda) = \lambda\frac{E_{\text{g}}}{hc} \tag{2.11}$$

where E_{g} is the minimum (direct or indirect) band gap of the material.

Several competing factors affect the photovoltaic conversion efficiency of thin-film nanoporous Si compared to bulk. Decreasing the volume fraction of Si in the nanostructures reduces the reflectivity on the front surface and increases the fraction of solar photons that enter the material. Moreover, quantum confinement by the nanopores enables pore-electron scattering and enhances the absorption of solar photons. In addition, the increased band gap of nanoporous Si results in a higher fraction of converted photon energy (Equation 3.4) and increased converted power density. On the other hand, larger band-gap values in the nanostructures blueshift the absorption edge and reduce the absorption of long-wavelength photons. To explore how these competing effects affect the photovoltaic conversion efficiency of thin-film Si, we calculated the electrical power of all 20 structures for a material thickness of 100 nm using Equation 3.2. The relative converted electrical power for the nanoporous structures compared to bulk Si is shown in Figure 2.8 as a function of pore radius and spacing. The data show that the introduction of nanopores can indeed improve the efficiency over the bulk. Among all the nanostructures studied, structure ***B*** ($L = 3a_{\text{Si}}$ and $R = 4.26$Å) exhibits the highest converted electrical power density (Equation 3.2), which is

about 2.5 times that of bulk Si for the considered thin-film thickness of 100 nm. If, in addition, we assume the effect of an antireflective coating to suppress the surface reflectivity of both bulk Si and structure *B*, the efficiency ratio decreases from 2.5 to 1.9 but the absolute efficiency of structure *B* increases from 4.1% to 5.9%. The structures with the smallest pore spacing show the highest conversion efficiencies for this material thickness. For fixed pore spacing the converted power first increases with increasing pore radius, due to the enhanced pore-electron scattering and increased converted electrical energy, followed by a decrease due to the blueshift of the absorption threshold that cancels out the other advantages of nanostructuring. The optimized photovoltaic conversion efficiency is achieved for small pore spacing and a radius-to-spacing ratio around 0.25 to 0.30. We note that excitonic effects have a significant effect on the efficiency of nanoporous Si and increase the converted power by as much as a factor of 2.5. We also note that phonon-assisted absorption, which is the only absorption mechanism of visible light in bulk Si, has not been considered for the nanoporous structures. If electron-phonon scattering is also considered for the nanostructures (in addition to electron-pore scattering) then the conversion efficiency is expected to increase further.

Our data can identify which photon wavelengths contribute the most to the produced electrical power for each Si structure. As an example, Figure 2.9 presents a comparison of the converted power density of nanoporous structures *A* and *B* with bulk Si analyzed in terms of absorbed photon wavelength for a material thickness of 100 nm. The location of the peak of the converted spectral irradiance for each structure is determined from the combined wavelength dependence of the solar irradiance, the reflectivity, and the absorption coefficient. The spectral peak for nanoporous Si structure *B* occurs at a longer wavelength than structure *A* and bulk Si because the absorption spectrum for structure *B* exhibits a peak at 2.7 eV (460 nm) (Figure 2.7b) which corresponds to large values of the solar irradiance.

In thin-film nanoporous Si structures the effect from Fabry-Perot resonance may not be neglected and reflections between the front and back surface should also be considered. In this case, the photovoltaic conversion efficiency is defined as

$$P = \int_0^{\lambda_{\max}} W(\lambda)[1 - R(\lambda) - T(\lambda)]C(\lambda)\,\mathrm{d}\lambda \tag{2.12}$$

where $R(\lambda)$ and $T(\lambda)$ are the reflectivity and transmissivity

$$R(\lambda) = \left| r_1 - \frac{t_1^2 r_2 e^{-i\delta}}{1 - r_1 r_2 e^{-i\delta}} \right|^2, \tag{2.13}$$

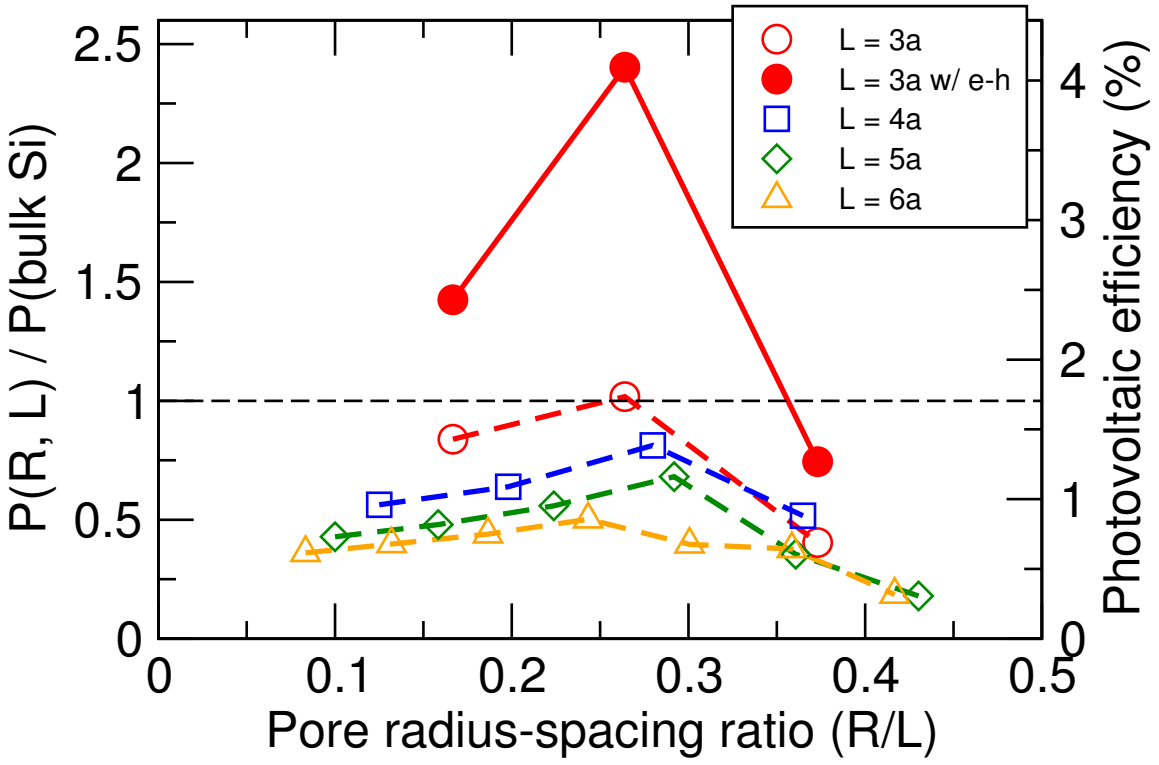

Figure 2.8: Relative converted electrical power produced in nanoporous Si relative compared to the bulk as a function of pore radius and spacing. A thin-film material thickness of 100 nm is assumed. The data show that nanoporous Si structures with pore spacing on the order of 3 times the lattice constant of bulk Si (16.3 Å) can exceed the photovoltaic efficiency of an equivalent bulk Si structure. Excitonic effects have only been considered for the smallest nanopore structures due to the computational cost of the calculations. Phonon-assisted optical processes that further increase the absorption coefficient have not been included in the absorption spectra of the nanostructures.

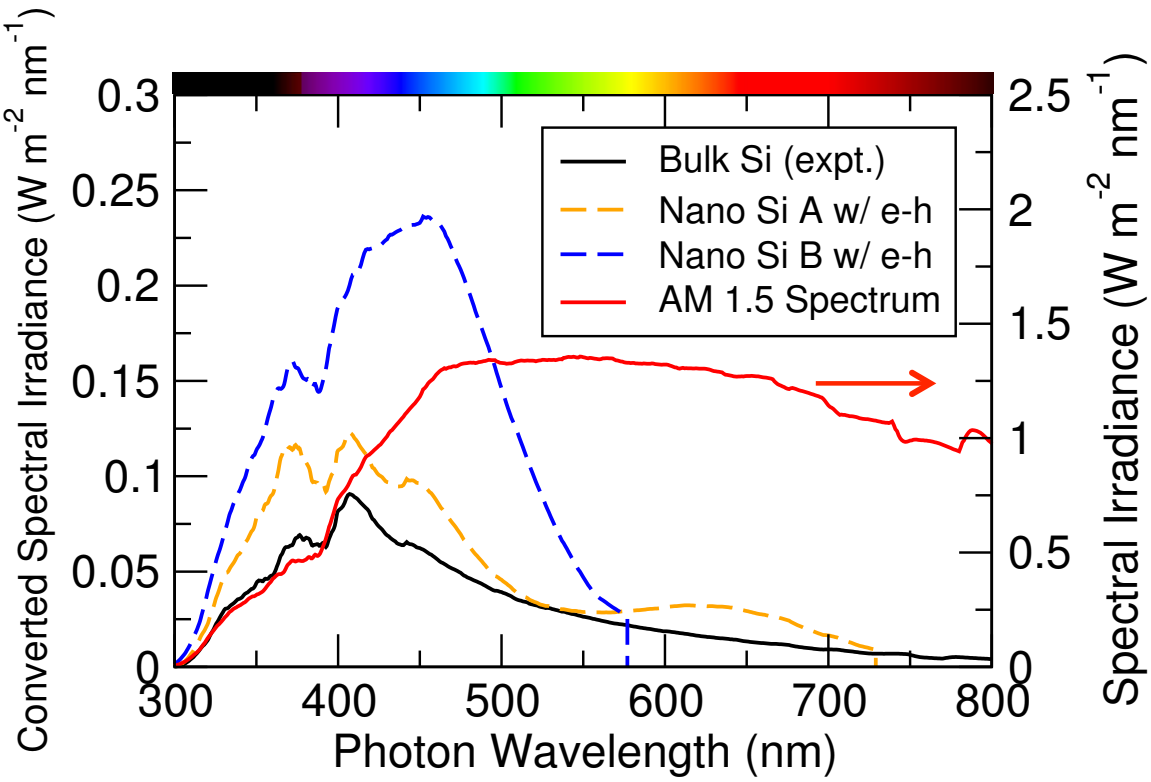

Figure 2.9: Converted spectral irradiance per unit area for nanoporous Si structures *A* and *B* and compared to bulk Si. The integrated area under each curve yields the converted electrical power per unit area for each structure. A material thickness of 100 nm is assumed.

and

$$T(\lambda) = \left| \frac{-t_1 t_2 e^{-i\delta}}{1 - r_1 r_2 e^{-i\delta}} \right|^2 . \tag{2.14}$$

The quantities $r_{1,2}$ and $t_{1,2}$ are the amplitude factors of the reflected and transmitted field at the front and back surface. The phase factor δ is defined as

$$\delta = \frac{2\pi \tilde{n} d}{\lambda}, \tag{2.15}$$

where $\tilde{n}$ is the complex refractive index. Thin-film effects introduce oscillations in the efficiency curves (Figure 2.10) due to the periodicity of the reflectivity and transmissivity with material thickness. The advantages of nanoporous Si compared to the bulk material for energy conversion are more pronounced in the 100-nm thickness regime. The nanoporous Si structure *B* shows the largest enhancement of conversion efficiency over bulk Si by a factor of 2.7 at the two peaks that correspond to thickness of 25 nm and 135 nm. Assuming the solar irradiance based on the direct standard AM 1.5 spectrum, nanoporous Si structure *B* has a photovoltaic conversion efficiency of 1.5% for a material thickness of 25 nm and 6.3% at a thickness of 135 nm. We note that a full investigation of solar-cell efficiency requires knowledge of the impact of defects on the device performance, as well as a number of other efficiency loss mechanisms (e.g., non-radiative recombination, energy loss at interfaces, etc.). However, defect simulations for these nanostructures are challenging, while the nature and concentration of defects depends on the growth conditions of the sample. In the present study we focus on the fundamental energy-conversion properties, therefore the efficiency we estimate constitutes an upper limit value. Nevertheless, our predictive calculations show that nanoporous Si with pore size and spacing on the scale of a few nanometers can indeed exhibit improved photovoltaic performance over bulk Si and can yield a theoretical maximum conversion efficiency of a few percent in thin-film solar-cell applications.

2.3 Conclusions

In conclusion, we used first-principles methods to calculate the electronic and optical properties of nanoporous Si with pore spacing and radius on the order of a few nanometers. We found that the inclusion of nanoscale pores increases the electronic band gaps due to quantum confinement and results in quasi-direct gaps for most examined structures. The visible-range absorption coefficient is greatly improved in nanoporous Si with small pore

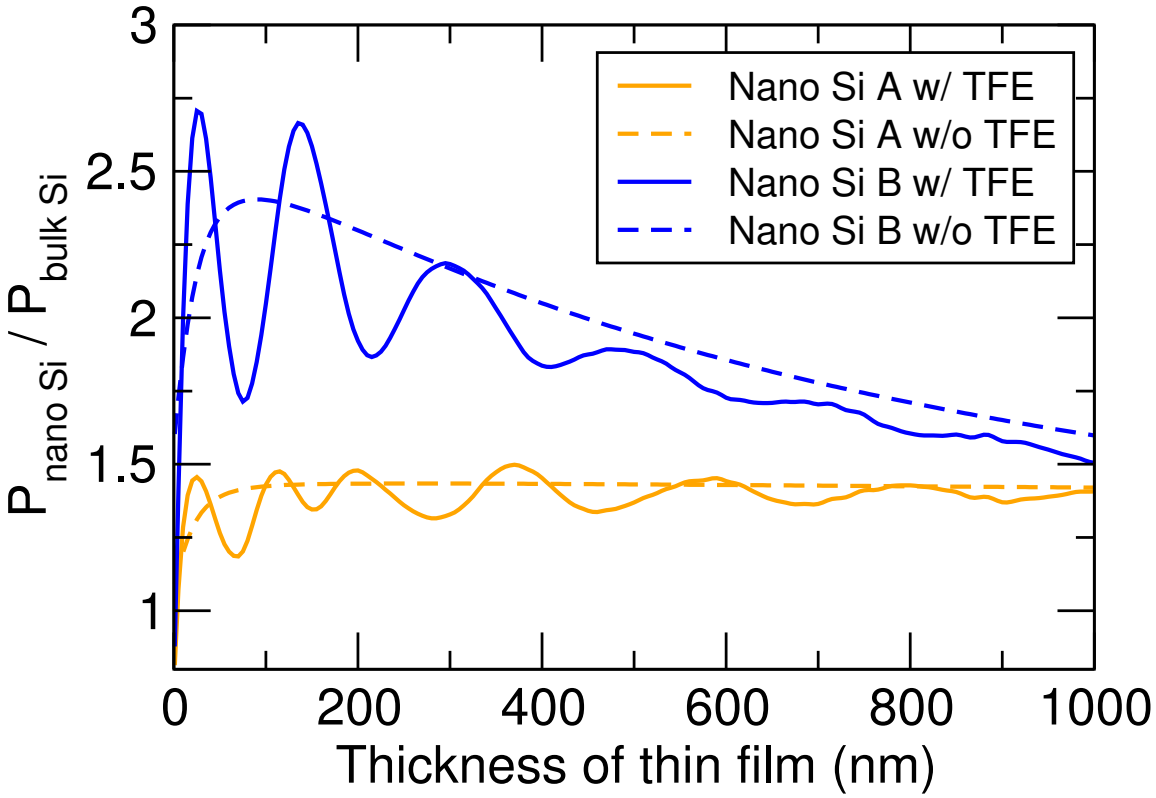

Figure 2.10: Converted electrical power produced in nanoporous Si structures *A* and *B* as a function of materials thickness relative to bulk Si including thin-film effects. The conversion efficiency for structure *B* has pronounced maxima for a thin-film thickness of 25 nm and 135 nm.

spacings and appropriately chosen pore sizes. Though quantum confinement reduces the wavelength range for the absorption of solar photons, the enhanced absorption coefficient as well as the reduced reflectivity and increased band gap improve the photovoltaic efficiency compared to bulk Si by a factor of 2.7 and yields a theoretical maximum conversion efficiency of 6.3% for thin-film (135 nm thick) solar cells.

Therefore, the enhanced electronic and optical properties of nanoporous Si make it a promising material for thin-film photovoltaic applications.

CHAPTER 3

Strong Visible-Light Absorbance in Few-Layer SnSe and GeSe

SnSe and GeSe are layered compound semiconductors that can be exfoliated to form two-dimensional materials. In this work, we use predictive calculations based on density functional and many-body perturbation theory to study the electronic and optical properties of single-layer, double-layer, and bulk SnSe and GeSe. The fundamental band gap is direct in single-layer and double-layer GeSe, but indirect in single-layer and double-layer SnSe. Moreover, the interplay of spin-orbit coupling and lack of inversion symmetry in the monolayer structures results in anisotropic spin splitting of the energy bands, with potential applications in directionally dependent spin transport. We also show that single-layer and double-layer SnSe and GeSe exhibit unusually strong optical absorbance in the visible range. Our results suggest that single-layer and double-layer SnSe and GeSe are promising materials for ultra-thin-film photovoltaic applications with theoretical upper bounds to the conversion efficiency that approach the efficiency records realized in organic and dye-sensitized solar cells.

Electrons in two-dimensional materials such as the transition metal dichalcogenides (TMDs) display an array of unique properties that enable novel electronic and optoelectronic applications. Unlike graphene, TMD monolayers have sizable band gaps that enable the fabrication of semiconductor devices including transistors, light emitters, and solar cells. TMDs undergo an indirect-to-direct band-gap transition if their thickness is reduced to a monolayer, as confirmed with optical measurements and first-principles calculations for MoS_2. [78, 79] The direct band gaps of TMD monolayers make them suitable for optoelectronic devices, for example light-emitting diodes (LEDs) and lasers. [80, 81, 82] Moreover, TMD monolayers have a strong optical absorbance in the visible range and can be used to fabricate solar cells with light-to-electricity conversion efficiencies of $\sim$0.5%.[81] Theoretical calculations also predict that the extraordinary absorbance of TMDs enables ultrathin ($\sim$1 nm) solar cells based on a stack of graphene and MoS_2 with an energy conversion efficiency of up to 1%.[83] In addition to their unusual optical properties, atomically thin TMDs display interesting spin physics that is promising for spin-transport applications. For example, the combined effects of spin-orbit coupling and inversion-symmetry breaking in TMD monolayers results in a strong coupling of the spin and valley degrees of freedom[84] that can be combined in spintronic and valleytronic devices.

Similar to TMDs, several IV-VI compounds including GeSe and SnSe also crystallize in layered structures with weak bonding between the layers. SnSe was recently demonstrated to be an exceptionally promising thermoelectric material with a record figure of merit at high temperature.[5, 85] SnS, a material similar to SnSe, is promising for thin-film solar cells because of its optimal bandgap ($\sim$1.3 eV) and high absorption coefficient.[86] While atomically thin TMD compounds have been the subject of extensive research, little is known about the properties of few-layer IV-VI materials. Tritsaris *et al.* studied few-layer SnS and found its optoelectronic properties to be tunable with the number of layers.[87] Recently, Li *et al.* synthesized 1-nm-thick SnSe nanosheets with a lateral size of $\sim$300 nm using a colloidal route.[88] In addition, density functional calculations show that single-layer IV-VI compounds are stable in either a distorted NaCl or litharge structure with formation energies comparable to single-layer MoS_2,[89] which indicates that mechanical exfoliation of bulk IV-VI materials may also be a possible route to produce atomically thin samples.

In this work, we perform first-principles calculations based on density functional theory (DFT) and many-body perturbation theory to analyze the electronic and optical properties of few-layer SnSe and GeSe. The fundamental band gaps are found to be direct in single-layer and double-layer GeSe, but indirect in SnSe few-layer structures. Our analysis reveals that the interplay of spin-orbit coupling with the symmetry of the monolayer

structures results in anisotropic spin-orbit splitting of the bands that can find applications in directionally dependent spin-transport devices. We also found that the optical absorbance in the visible range is high for the few-layer structures, reaching values as high as 47% for bilayer SnSe with a thickness of just 1 nm. Our results suggest that few-layer SnSe and GeSe are promising materials for ultra-thin-film flexible photovoltaic applications with an upper limit to the conversion efficiency that rivals the record efficiencies of organic and dye-sensitized solar cells. This work has been published in Nano Letters.[26]

3.1 Methodology

Our first-principles computational methodology is based on the combination of DFT with many-body perturbation theory, which yields excellent results for the electronic and optical properties of inorganic materials and nanostructures.[90] All calculations use the generalized gradient approximation[91] for the exchange-correlation potential. The structure was optimized using the projector-augmented waves and a plane-wave cutoff of 300 eV as implemented in the Vienna Ab initio Simulation Package.[41, 92] We calculated the quasiparticle band structures with the one-shot GW method[65] and the BerkeleyGW code.[1] To calculate electron wave functions for subsequent GW calculations, we used norm-conserving pseudopotentials[64] and a plane-wave cutoff of 50 Ry as implemented in Quantum-ESPRESSO.[40] The static dielectric function was calculated with a 20 Ry plane-wave cutoff and extended to finite frequency using a generalized plasmon-pole model.[65] The Coulomb-hole term was calculated using the static-remainder approach[66] and a sum over unoccupied bands up to 8 Ry above the valence band maximum (VBM). Spin-orbit coupling corrections to the GW eigenvalues were calculated in a non-self-consistent way by evaluating the off-diagonal elements of the spin-orbit part of the Hamiltonian and diagonalizing the resulting matrix.[93] For the bulk systems, we sampled the Brillouin zone using a grid of $6\times6\times4$ to determine the polarizability matrices and quasiparticle energies. For the few-layer systems, we used a shifted k-point grid of $8\times8\times1$ for the polarizability matrices and a $16\times16\times1$ grid for the quasiparticle energies. We truncated the Coulomb interaction in the few-layer systems along the directions perpendicular to the layers to remove the artificial interaction between adjacent periodic simulation cells.[94] We used maximally localized Wannier functions[95, 96] to interpolate the quasiparticle energies and spin-orbit coupling matrix elements to fine meshes in the first Brillouin zone as in Ref. [97] to determine the band structures and band extrema. We calculated the exciton binding energies and optical absorption spectra with the Bethe-Salpeter equation method as implemented in BerkeleyGW.[45] For the bulk systems, the electron-hole interaction kernel was interpo-

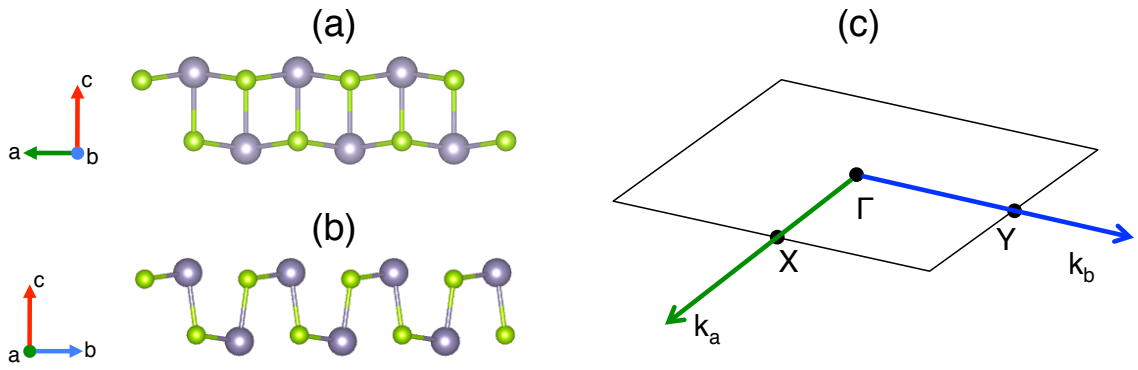

Figure 3.1: Crystal structure of single-layer SnSe showing the (a) zigzag (parallel to a) and (b) armchair (parallel to b) directions, and (c) the corresponding Brillouin Zone.

lated on a 24×24×12 k-point grid. For the few-layer systems, we recalculated the polarizability matrices and electron-hole interaction kernel using a k-point grid of 32×32×1 to capture the long-range variations of the screening. These computational parameters converge the lattice constants to within 1%, the GW eigenvalues to less than 0.1 eV, and the exciton binding energies to less than 50 meV. The detailed procedures and results of the convergence tests for these computational parameters are discussed in the Supporting Information. We have previously performed similar calculations with this methodology for PbI_2 and the obtained results are in good agreement with experiment.[98]

3.2 Results and Discussion

3.2.1 Structure

SnSe and GeSe are the compound analogues of elemental phosphorene and crystallize in a similar layered structure. The symmetry group of their low-temperature crystal structure is *Pnma* and resembles a distorted NaCl arrangement. Figure 3.1 shows the structure of single-layer SnSe along the in-plane zigzag and armchair directions, as well as the corresponding Brillouin Zone with the high-symmetry X and Y points denoted. Although the bulk crystal has an inversion point, the inversion symmetry is broken in the monolayer structures. We will show later that the combination of this lack of inversion symmetry along with spin-orbit coupling breaks the spin degeneracy of the monolayer band structure and leads to directionally dependent spin-orbit-induced spin splitting of the band structure.

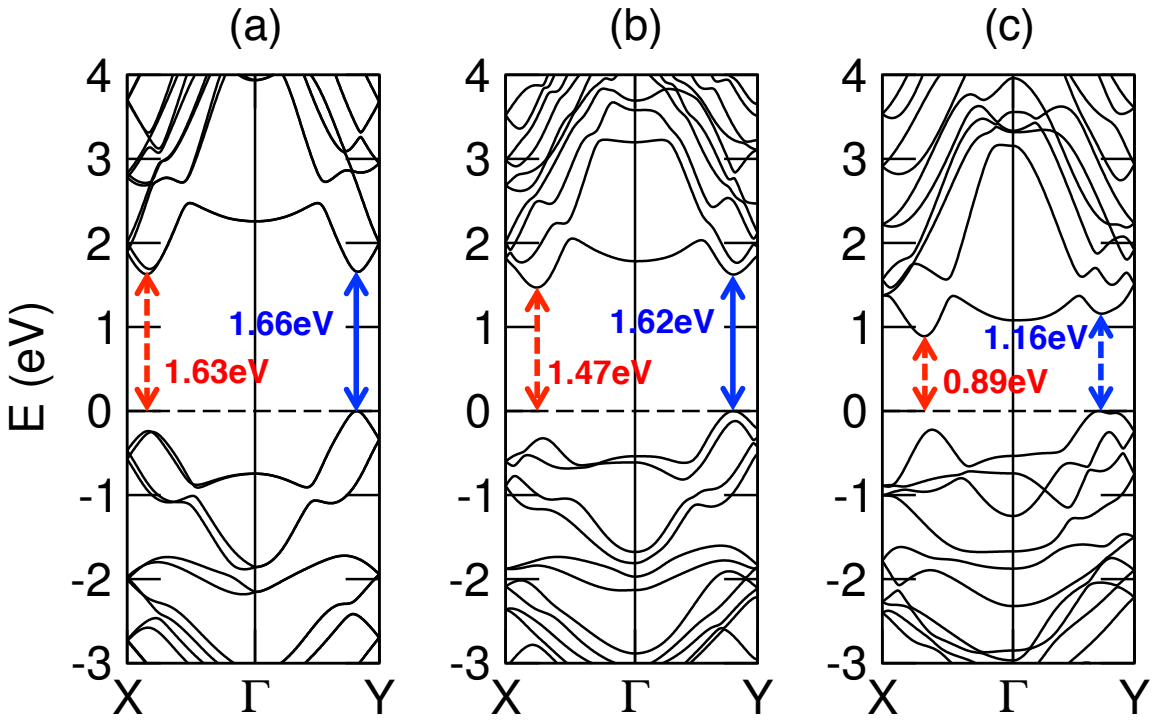

Figure 3.2: Band structures of (a) single-layer, (b) double-layer, and (c) bulk SnSe. The energies of the transitions from the valence-band maximum (VBM) to the two conduction-band minima (CBM) along and Γ–Y are denoted. Solid arrows indicate direct transitions and dashed arrows indicate indirect transitions. The minimum direct gap in single-layer and double-layer SnSe is located along Γ–Y (solid arrows), but in bulk SnSe the smallest direct gap (1.14 eV) is located along Γ–X (not shown). The SnSe monolayer is an indirect-gap material, but the energy difference between the indirect gap (1.63 eV) and the minimum direct gap (1.66 eV) is small. The monolayer lacks inversion symmetry, and thus spin-orbit coupling breaks the spin degeneracy of the band structure. Although the spin symmetry is broken along the Γ–X direction, the bands are spin-degenerate along Γ–Y. This is due to the different symmetry of the monolayer structure along the armchair and zigzag directions, leading to directionally dependent spin splitting and spin-transport properties.

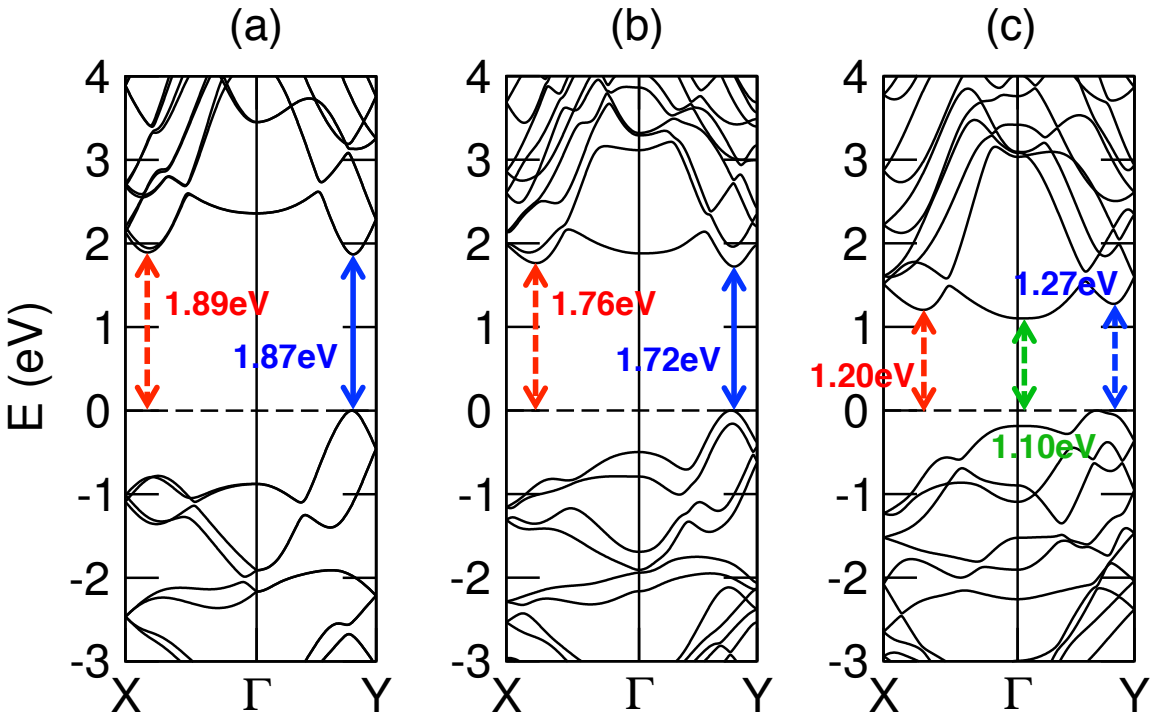

Figure 3.3: Band structures of (a) single-layer, (b) double-layer, and (c) bulk GeSe. The energies of the transitions from the valence-band maximum (VBM) to the three conduction-band minima (CBM) along the Γ–X and Γ–Y directions are denoted. Solid arrows indicate direct transitions and dashed arrows indicate indirect transitions. The minimum direct gap in single-layer and double-layer GeSe occurs along Γ–Y (solid arrows). The smallest direct gap of bulk GeSe (1.29 eV) also occurs along Γ–Y (not shown). The GeSe monolayer is a direct-gap material, but there is only a small energy difference between the direct (1.87 eV) and the indirect gap (1.89 eV). The monolayer lacks inversion symmetry, and thus spin-orbit coupling breaks the band spin degeneracy, except for points along the Γ–Y direction.

3.2.2 Band structure

The calculated band structures of bulk SnSe and GeSe, including quasiparticle and spin-orbit coupling corrections, are shown in Figs. 3.2 and 3.3. The band gap of bulk SnSe is indirect, with the valence-band maximum along Γ–Y and the conduction-band minimum along Γ–X. The conduction band displays two local minima along Γ–Y, one near Γ and one closer to Y. The bands of bulk SnSe show strong non-parabolicity and warping, as discussed in the context of the thermoelectric properties of this material.[85] The value of the bulk SnSe gap (0.89 eV) is in good agreement with optical-absorption measurements (0.90 eV[99]). The gap of bulk GeSe is also indirect, with the valence-band maximum and the conduction-band minimum at different points along Γ–Y, the conduction-band minimum being close to Γ. Local conduction-band minima appear at energies 0.10 eV and 0.17 eV higher than the global minimum along Γ–X and Γ–Y, respectively. The bulk GeSe gap (1.10 eV) is also in good agreement with optical-absorption measurements (1.10 eV[100], 1.08 eV[101]).

The calculated band structures of single-layer and double-layer SnSe and GeSe are also shown in Figs. 3.2 and 3.3. One local conduction-band minimum is located along each of the Γ–X and Γ–Y directions of the few-layer structures while the valence band maximum is along Γ–Y. The minimum gap is found to be direct in single-layer and double-layer GeSe, and indirect in single-layer and double-layer SnSe. However, the difference between the indirect gap and the smallest direct gap of the monolayers is small, on the order of 20–30 meV, which is within the typical 0.1 eV accuracy of the computational method. It is therefore plausible that the nature of the gaps for the single-layer structures (direct or indirect) may not be properly determined by our computational results. On the other hand, the small energy difference between the two conduction-band minima along Γ–X and Γ–Y in these single-layer materials indicate that the nature of the gap may be tunable from direct to indirect or vice versa by the application of external controls (e.g., strain). Both band gaps increase as the number of atomic layers in the structure decreases due to quantum confinement. For the single-layer structures, the spin-orbit coupling interaction splits the spin-degenerate bands due to the lack of inversion symmetry. However, the bands are spin degenerate along Γ–Y due to the symmetry of the crystal. As a result, the spin-orbit-induced splitting of the bands is strongly anisotropic, with potential applications for directionally dependent spin transport. The anisotropic spin-transport properties may be further tuned by the application of in-plane strain, similar to the effect of strain on controlling the anisotropic electrical conductance in phosphorene.[102] The splitting of the conduction-band minimum along Γ–X is 70 meV in SnSe and 50 meV in GeSe. This band splitting due to spin-orbit coupling and lack of inversion symmetry has also been reported

Table 3.1: The exciton binding energies (in eV) of single-layer, double-layer and bulk SnSe and GeSe.

	1-layer	2-layer	bulk
SnSe	0.27	0.20	<0.01
GeSe	0.32	0.23	<0.01

Table 3.2: The full-width at half-maximum (fwhm) of the exciton wave function squared of single-layer and double-layer SnSe and GeSe along the zigzag (a) and armchair (b) axis.

	1-layer		2-layer	
	a (Å)	b (Å)	a (Å)	b (Å)
SnSe	40	40	48	49
GeSe	34	34	42	41

for MoS_2 monolayers and other TMDs, with similarly large energy splitting values.[103]

3.2.3 Excitons

In addition to increasing the band-gap energy, the strong quantum confinement in the few-layer structures also results in strong excitonic effects. Although the exciton binding energy is small in bulk materials (less than 10 meV according to our calculations), it increases to 0.27 eV in SnSe and 0.32 eV in GeSe single layers (Table 3.1), which indicates that excitons are thermally stable at room temperature in the few-layer structures. The exciton binding energies in these nanometer-thick IV-VI materials are smaller than the exciton binding energies of similarly confined III-V semiconductors (e.g., 1.4 eV in 1-nm thick InN nanowires[104]) due to the heavier electron effective mass of the IV-VI compounds.[85] Although the effect of spin-orbit coupling was not taken into account in evaluating the excitonic effects, we expect it to only have a minor effect in the calculated values since it only reduces the direct band gap energies by less than 40 meV in all the systems we considered. Figure 3.4 shows the electron wave function of the lowest-energy exciton in single-layer SnSe. The electron part of the exciton wave function displays the Sn p_y orbital character (oriented along the b axis) of the conduction band. We used the full-width at half-maximum (fwhm) of the envelope function to evaluate the size of exciton (Table 3.2). For both SnSe and GeSe, the excitons are more localized in the single-layer structures than in the double layers, and they exhibit a similar width along the zigzag and the armchair directions. We also found excitons to be systematically smaller in GeSe than in SnSe materials, which is consistent with the trend of the exciton binding energies (Table 3.1).

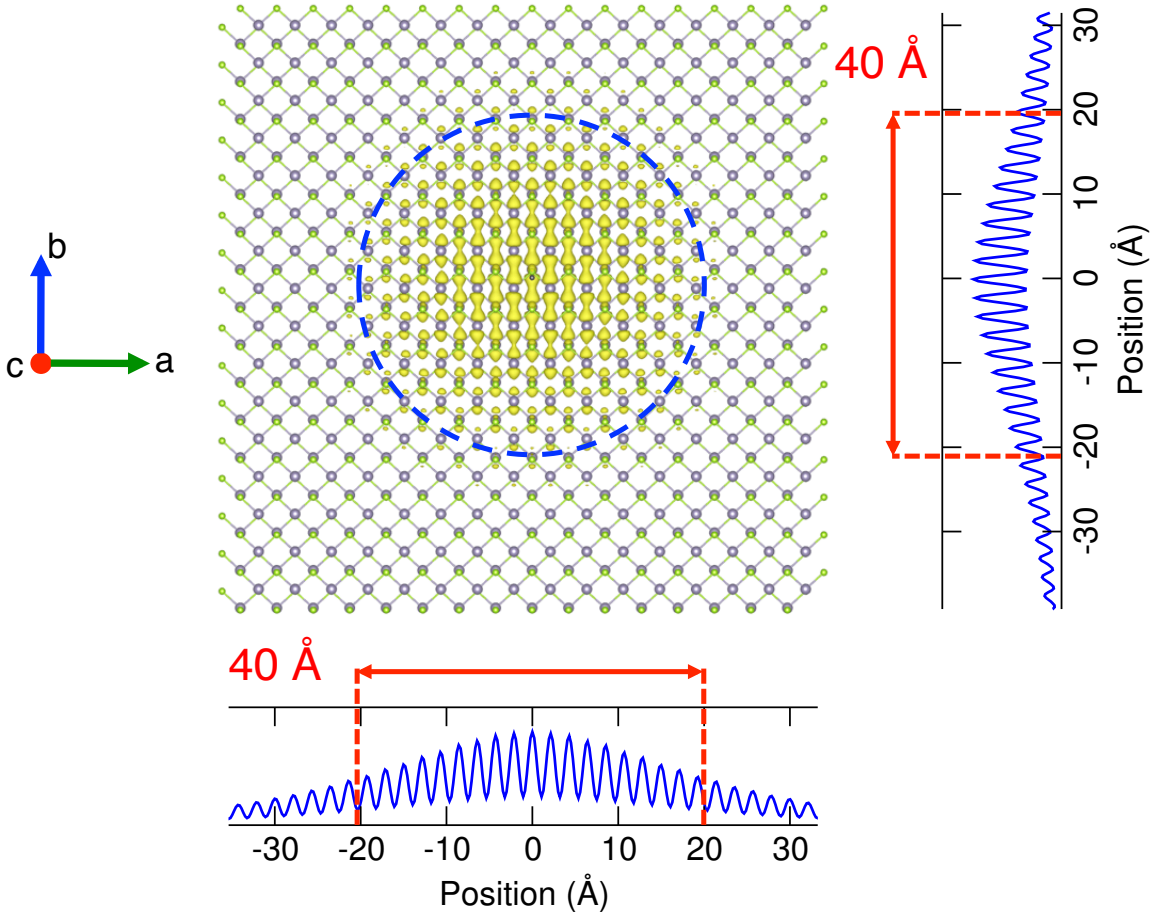

Figure 3.4: The electron part of the exciton wave function squared of the lowest-energy exciton in single-layer SnSe. The hole position is fixed at (0,0). The exciton wave function has a full width at half maximum of 40 Å along both in-plane directions.

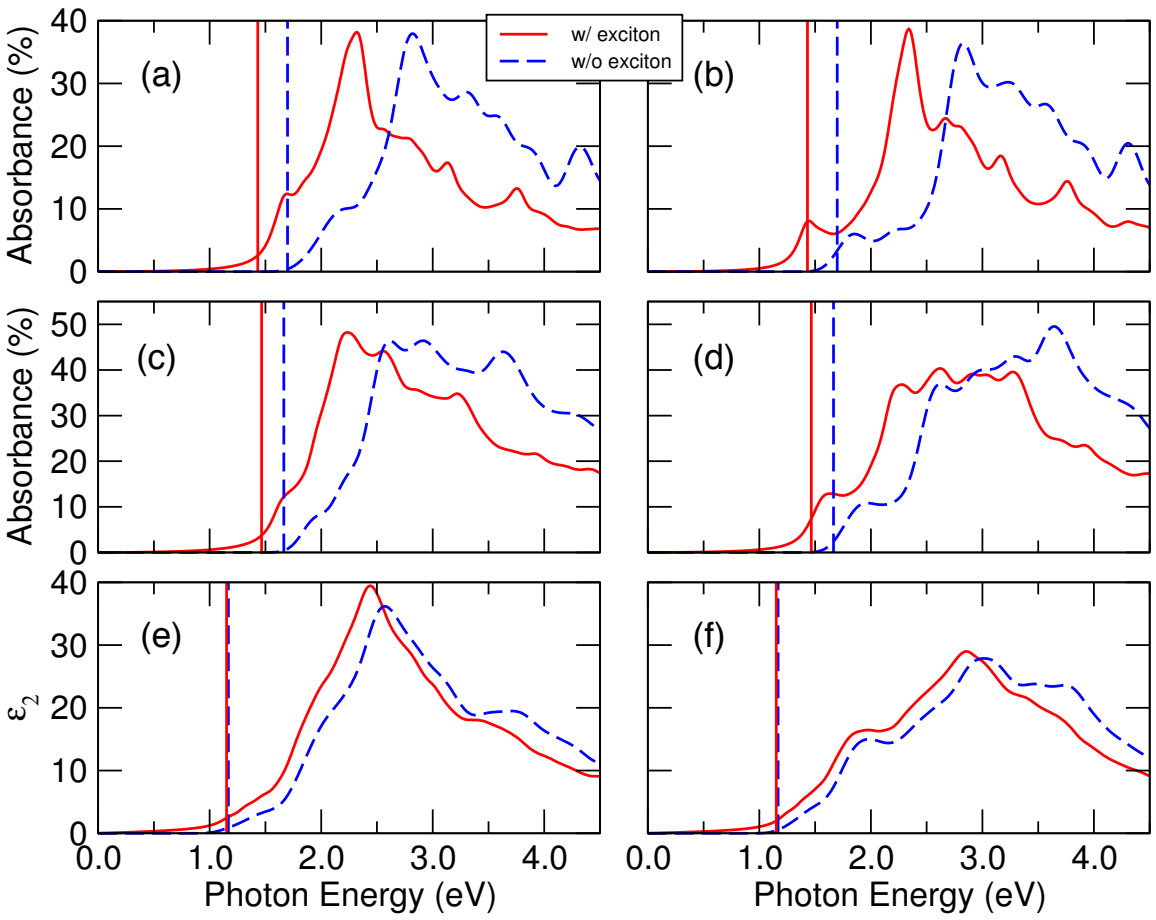

Figure 3.5: Optical absorption spectra of (a, b) single-layer, (c, d) double-layer, and (e, f) bulk SnSe for light polarized along the zigzag (left side) and armchair (right side) directions. The solid red lines and dashed blue lines are the spectra with and without excitonic effects included, correspondingly. The vertical lines indicate the onset of optical absorption for the corresponding curve.

3.2.4 Visible-light absorbance

The few-layer structures of SnSe and GeSe are unusually strong absorbers of visible radiation. Figures 3.5 and 3.6 show the optical absorption spectra of single-layer, double-layer and bulk SnSe and GeSe as a function of photon energy and polarization. The absorbance of the few-layer structures A as a function of photon energy E is calculated according to

$$A(E) = 1 - e^{-\alpha(E)d} = 1 - e^{-\frac{2\pi E}{hc}\epsilon_2 d}, \tag{3.1}$$

where α is the absorption coefficient, ϵ_2 is the imaginary part of the dielectric function, and d is the thickness of the simulation cell perpendicular to the layers. Similar to black phosphorus,[105] the absorption spectra differ for light polarized along the zigzag or arm-

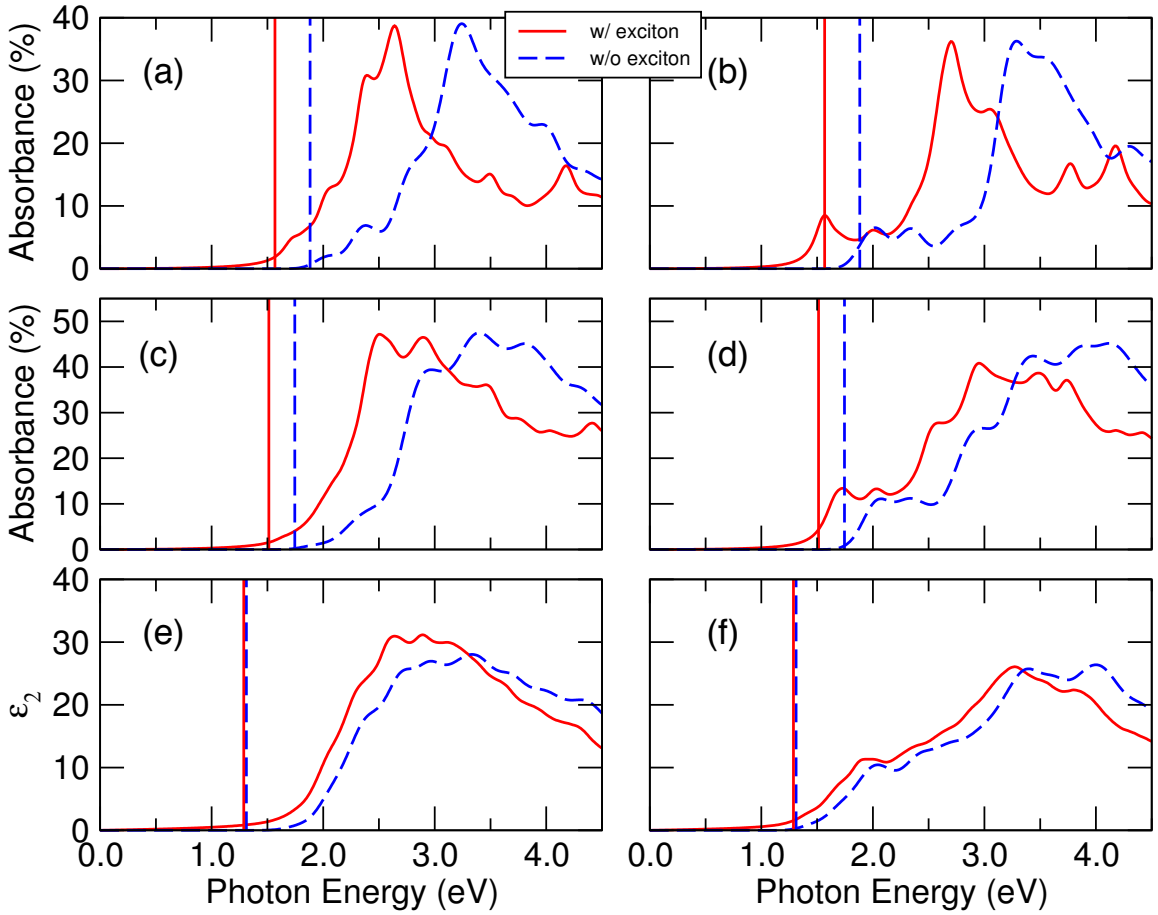

Figure 3.6: Optical absorption spectra of (a, b) single-layer, (c, d) double-layer, and (e, f) bulk GeSe for light polarized along the zigzag (left side) and armchair (right side) directions. The solid red lines and dashed blue lines are the spectra with and without excitonic effects included, correspondingly. The vertical lines indicate the onset of optical absorption for the corresponding curve.

chair directions due to the in-plane anisotropy of the materials. We also note that both the direct band gap and the optical gap (i.e., the lowest direct exciton energy) of the two materials blueshift as the number of layers decreases in both SnSe and GeSe. The amount of blueshift is determined by the combined effects of enlarged band gap due to quantum confinement and stronger electron-electron interactions, and increased exciton binding energy due to larger spatial overlap of electron and hole wave functions in the few-layer structures. The visible-light absorbance of the few-layer materials is found to be remarkably large, approaching values up to 38% percent in single-layer and 47% percent in double-layer SnSe. We attribute the high absorbance in the few-layer structures to the nature of the atomic orbitals that form the band extrema of these materials. Since the group-IV cations occur in the 2+ charge state, the lowest conduction bands consist of cation p orbitals (Ge $4p$ or Sn $5p$), while the filled Se valence $4p$ orbitals form the topmost valence bands. Since there are three p orbitals per cation that are directional in space, they give rise to three anisotropic bands per cation atom in the unit cell, each with large effective mass along the directions perpendicular to the p-orbital orientation axis. The band characters of these IV-VI materials is in contrast to direct-gap III-V semiconductors such as GaAs and GaN, for which the s-orbital character of the conduction-band minimum at Γ results in a unique, isotropic conduction band with a small electron effective mass. As a consequence of the larger number of bands that occur near the band extrema and their larger directionally-averaged effective masses, the joint density of states is larger in IV-VI than in III-V compounds and results in a larger probability of optical transitions across the gap, and hence a larger absorption coefficient.

3.2.5 Photovoltaic conversion efficiency

The combination of the unusually strong optical absorbance in the visible range and the values of the semiconducting gap of few-layer SnSe and GeSe makes them promising for efficient ultrathin solar-cell applications. We used the method we developed elsewhere[106] to calculate the theoretical upper limit to the conversion efficiency of sunlight to lowest exciton energy for these ultrathin materials (Table 3.3). The estimated upper limit to the converted power P is based on the overlap between the solar spectrum and the absorbance:

$$P = \frac{\int_0^{\lambda_{\max}} W(\lambda) A(\lambda) C(\lambda)\, \mathrm{d}\lambda}{\int_0^{\infty} W(\lambda)\, \mathrm{d}\lambda}, \tag{3.2}$$

Table 3.3: The upper limit of the energy conversion efficiency of sunlight to lowest-energy excitons for single-layer and double-layer SnSe and GeSe.

	1-layer	2-layer
SnSe	7.1	10.4
GeSe	5.2	7.2

where λ is the photon wavelength, λ_{max} is the longest wavelength that can be absorbed by the few-layer SnSe and GeSe and is determined by the lowest-exciton energy (E_{o}),

$$\lambda_{\text{max}} = \frac{hc}{E_{\text{o}}}, \tag{3.3}$$

and $W(\lambda)$ is the solar spectral irradiance at Air Mass 1.5.[77] $A(\lambda)$ is the directionally averaged absorbance of the few-layer structures plotted in Figs. 3.5 and 3.6, and the term $C(\lambda)$ is the conversion factor to account for the fraction of the photon energy converted to lowest-exciton energy (i.e., the thermalization loss),

$$C(\lambda) = \lambda \frac{E_{\text{o}}}{hc}. \tag{3.4}$$

Although the absorbance of SnSe and GeSe few-layer structures is comparable, SnSe materials have consistently larger conversion efficiencies than their GeSe counterparts because of the larger overlap between their absorbance and the solar spectrum. The typical upper limit to the energy conversion efficiency for few-layer GeSe and SnSe takes values of a few percent and can be as high as 10.4% for bilayer SnSe. This remarkable efficiency upper limit it is achieved with a SnSe material thickness of just 1 nm and is comparable to the current efficiency records realized with organic and dye-sensitized solar-cell technologies. Our results therefore indicate that ultrathin SnSe is a promising material for efficient thin-film flexible solar cells.

3.3 Conclusions

In summary, we determined the quasiparticle band structures and optical properties of single-layer, double-layer, and bulk SnSe and GeSe using first-principles calculations. Single-layer and double-layer GeSe have a direct band gap, while the gaps of the SnSe monolayer and bilayer are indirect. Spin-orbit coupling and lack of inversion symmetry in the monolayers results in directionally dependent splitting of the energy bands and anisotropic spin-transport properties. The exciton binding energy is approximately 300 meV in both monolayer materials, which results in thermally stable excitons at room tem-

perature. We also uncovered the strong absorbance of few-layer SnSe and GeSe in the visible range that reaches values as large as 47%, which suggests potential applications in efficient, ultrathin, and flexible photovoltaic devices with upper bounds to the conversion efficiency that rivals organic and dye-sensitized devices.

CHAPTER 4

Free-Carrier Absorption in n-Type Silicon

The absorption of light by free carriers in semiconductors such as silicon results in intra-band electron or hole excitations, and competes with optical transitions across the band gap. Free-carrier absorption therefore reduces the efficiency of optoelectronic devices such as solar cells because it does not generate electron-hole pairs and results in energy loss. In this work, we use first-principles calculations based on density functional theory to investigate direct and indirect free-carrier absorption in n-type silicon. We determine the free-carrier absorption coefficient as a function of carrier concentration and compare to experiment. We also identify the dominant mechanisms that contribute to free-carrier absorption processes, and analyze the results to evaluate the impact of this loss mechanism on the efficiency of silicon solar cells.

Silicon is an earth-abundant material of great importance in semiconductor electronics such as solar cells. However, Si has an indirect band gap and optical transitions across its minimum gap require the assistance of phonons.[48] This results in a low absorption coefficient in the visible range and increases the material thickness and cost for photovoltaic applications. In Si solar cells, Si is doped to introduce free carriers for high conductivity, and the free carriers can also absorb photons in a variety of ways. The weak cross-gap light absorption in the visible range associated with the electron-phonon scattering is thus in competition with the absorption of light by free carriers. The free-carrier absorption processes may include the dissipative process in the plasmon oscillations, as well as one-particle transitions from a filled conduction-band state to a higher one.

Figure 4.1 shows the GW band structure of Si, which has a calculated indirect band gap of 1.27 eV. When free electrons in the conduction band absorb photons, they may undergo either direct or indirect transitions, provided energy and momentum are conserved in the absorption process. In the case of indirect absorption, additional momentum is supplied by a scattering process. We will consider three important indirect processes here: those mediated by phonons, those due to the scattering by ionized impurities, and those due to the scattering by plasmons. The latter two are especially important in heavily doped Si.

Free-carrier absorption is usually treated by the Drude model. This model works well for intraband absorption processes in the infrared but fails for absorption in the visible range where the bands deviate from parabolicity. Moreover, the Drude model is based on the scattering time approximation and the scattering time is usually derived by fitting to experimental data, and thus the model is not adequate for an accurate determination of free-carrier absorption of a novel material. A first-principles method has been developed and calculated results have been previously reported for nitrides[107, 108] and SnO_2[109, 110] with a focus on phonon- and charged-impurity-assisted absorption. In this work we go beyond the previous work by (i) addressing five different free-carrier absorption processes, including plasmon dissipative process, direct transition, and phonon-, charged-impurity-, and plasmon-assisted transitions, (ii) discussing the comparison between theoretical results and experiment, and (iii) predicting the free-carrier absorption above the band gap of Si and the subsequent energy loss in silicon solar cells.

4.1 Methodology

4.1.1 Formalism

The imaginary part of dielectric function for the plasmon dissipative process is calculated using a linearized Boltzmann Equation with a relaxation time approximation[111]:

$$\epsilon_2(\omega) = \frac{4\pi\sigma}{\omega(1+\omega^2\tau^2)}, \tag{4.1}$$

where σ is the conductivity and τ is the relaxation time of carriers. Fermi's golden rule is used to calculate the direct and indirect absorption coefficients. For direction absorption, the imaginary part pf dielectric function is expressed as:

$$\epsilon_2(\omega) = \frac{16\pi^2 e^2}{\omega^2} \sum_{ij\boldsymbol{k}} |\boldsymbol{e} \cdot \langle i\boldsymbol{k}|\boldsymbol{v}|j\boldsymbol{k}\rangle|^2 \delta(\hbar\omega - \epsilon_{i\boldsymbol{k}} + \epsilon_{j\boldsymbol{k}}), \tag{4.2}$$

where $\boldsymbol{v}$ is the velocity operator along the direction of the polarization of light $\boldsymbol{e}$, and $\hbar\omega$ is the photon energy. i and j indicate the band number indices, and $\boldsymbol{k}$ the wave vectors. For the phonon-assisted absorption, the absorption coefficient is expressed as:

$$\alpha_{\text{el-ph}}(\omega) = 2\frac{4\pi^2 e^2}{\omega c n_r(\omega)} \frac{n_{\text{I}} Z}{N_{\boldsymbol{k}} N_{\boldsymbol{q}}} \sum_{\nu ij\boldsymbol{kq}} |\boldsymbol{e} \cdot (\boldsymbol{S}_1 + \boldsymbol{S}_2)|^2 \times P\delta(\epsilon_{j,\boldsymbol{k}+\boldsymbol{q}} - \epsilon_{i\boldsymbol{k}} - \hbar\omega \pm \hbar\omega_{\nu\boldsymbol{q}}), \tag{4.3}$$

where Z and n_{I} are the charge and concentration of the defects, c is the speed of light and n_r is the refraction index. The generalized matrix elements $\boldsymbol{S}_1$ and $\boldsymbol{S}_2$ and the statistics factor P are

$$\boldsymbol{S}_1(\boldsymbol{k},\boldsymbol{q}) = \sum_m \frac{\boldsymbol{v}_{im}(\boldsymbol{k}) g^{\text{el-ph}}_{mj,\nu}(\boldsymbol{k},\boldsymbol{q})}{\epsilon_{m\boldsymbol{k}} - \epsilon_{i\boldsymbol{k}} - \hbar\omega}, \tag{4.4}$$

$$\boldsymbol{S}_2(\boldsymbol{k},\boldsymbol{q}) = \sum_m \frac{g^{\text{el-ph}}_{im,\nu}(\boldsymbol{k},\boldsymbol{q}) \boldsymbol{v}_{mj}(\boldsymbol{k}+\boldsymbol{q})}{\epsilon_{m,\boldsymbol{k}+\boldsymbol{q}} - \epsilon_{i\boldsymbol{k}} \pm \hbar\omega_{\nu\boldsymbol{q}}}, \tag{4.5}$$

$$P = (n_{\nu\boldsymbol{q}} + \frac{1}{2} \pm \frac{1}{2})(f_{i\boldsymbol{k}} - f_{j,\boldsymbol{k}+\boldsymbol{q}}), \tag{4.6}$$

where $\boldsymbol{v}_{ij}(\boldsymbol{k})$ are the velocity matrix elements, $g^{\text{el-ph}}_{ij,\nu}(\boldsymbol{k},\boldsymbol{q})$ are electron-phonon coupling matrix elements, and $n_{\nu\boldsymbol{q}}$ and $f_{i\boldsymbol{k}}$ are the phonon and electron occupation numbers. The upper (lower) sign corresponds to phonon emission (absorption). The expressions for the charged-impurity- and plasmon-assisted absorption are similar to that for the phonon-assisted absorption with the phonon frequencies set to zero and are expressed as:

$$\alpha_{\text{impurity}}(\omega) = 2\frac{4\pi^2 e^2}{\omega c n_r(\omega)} \frac{n_{\text{I}}^2 Z^2 V}{N_{\boldsymbol{k}} N_{\boldsymbol{q}}} \sum_{ij\boldsymbol{kq}} |\boldsymbol{e}\cdot(\boldsymbol{S}_1+\boldsymbol{S}_2)|^2 \times \delta(\epsilon_{j,\boldsymbol{k}+\boldsymbol{q}} - \epsilon_{i\boldsymbol{k}} - \hbar\omega), \tag{4.7}$$

$$\alpha_{\text{plasmon}}(\omega) = 2\frac{4\pi^2 e^2}{\omega c n_r(\omega)} \frac{n_{\text{I}}^2 Z^2 V}{N_{\boldsymbol{k}} N_{\boldsymbol{q}}} \sum_{ij\boldsymbol{kq}} |\boldsymbol{e}\cdot(\boldsymbol{S}_1+\boldsymbol{S}_2)|^2 \times P\delta(\epsilon_{j,\boldsymbol{k}+\boldsymbol{q}} - \epsilon_{i\boldsymbol{k}} - \hbar\omega), \tag{4.8}$$

where V is the volume of cell. The generalized matrix elements ($\boldsymbol{S}_1$ and $\boldsymbol{S}_2$) are again given by Eqs. 4.4 and 4.5 but with the $g^{\text{el-ph}}_{ij,\nu}(\boldsymbol{k},\boldsymbol{q})$ replaced by the charged-impurity and plasmon matrix elements:

$$g^{\text{impurity}}_{ij}(\boldsymbol{k},\boldsymbol{q}) = \frac{1}{V}\langle i,\boldsymbol{k}|\frac{4\pi e^2 Z}{\epsilon(q)(q^2+\lambda^2)}|j,\boldsymbol{k}+\boldsymbol{q}\rangle, \tag{4.9}$$

$$g^{\text{plasmon}}_{ij}(\boldsymbol{k},\boldsymbol{q}) = \langle i,\boldsymbol{k}|\frac{4\pi e q}{\epsilon(q)(q^2+\lambda^2)}\frac{\sqrt{\hbar\omega_{\text{plasmon}}}}{\sqrt{2V}}|j,\boldsymbol{k}+\boldsymbol{q}\rangle, \tag{4.10}$$

where λ is the screening length, and $\epsilon(q)$ is a model dielectric function[112] given by

$$\epsilon(q) = 1 + \left[\frac{1}{\epsilon(0)-1} + d(\frac{q}{\lambda_{\text{TF}}})^2 + \frac{\hbar^2 q^4}{4m^2\omega^2_{\text{plasmon}}}\right]^{-1}. \tag{4.11}$$

Here d is a parameter taken to be 1.563, λ_{TF} the Thomas-Fermi screening length, and ω_{plasmon} the plasmon frequency. The screening length λ corresponds to Debye screening in the nondegenerate case (Fermi energy lower than the conduction band minimum) and to Thomas-Fermi screening in the degenerate case.

4.1.2 Computational details

We studied the electronic properties of Si using first-principles calculations based on density functional and many-body perturbation theory. We calculated the ground-state charge density and electronic wave functions using the generalized gradient approximation[38, 91] for the exchange-correlation potential. We used the plane-wave pseudopotential method[63]

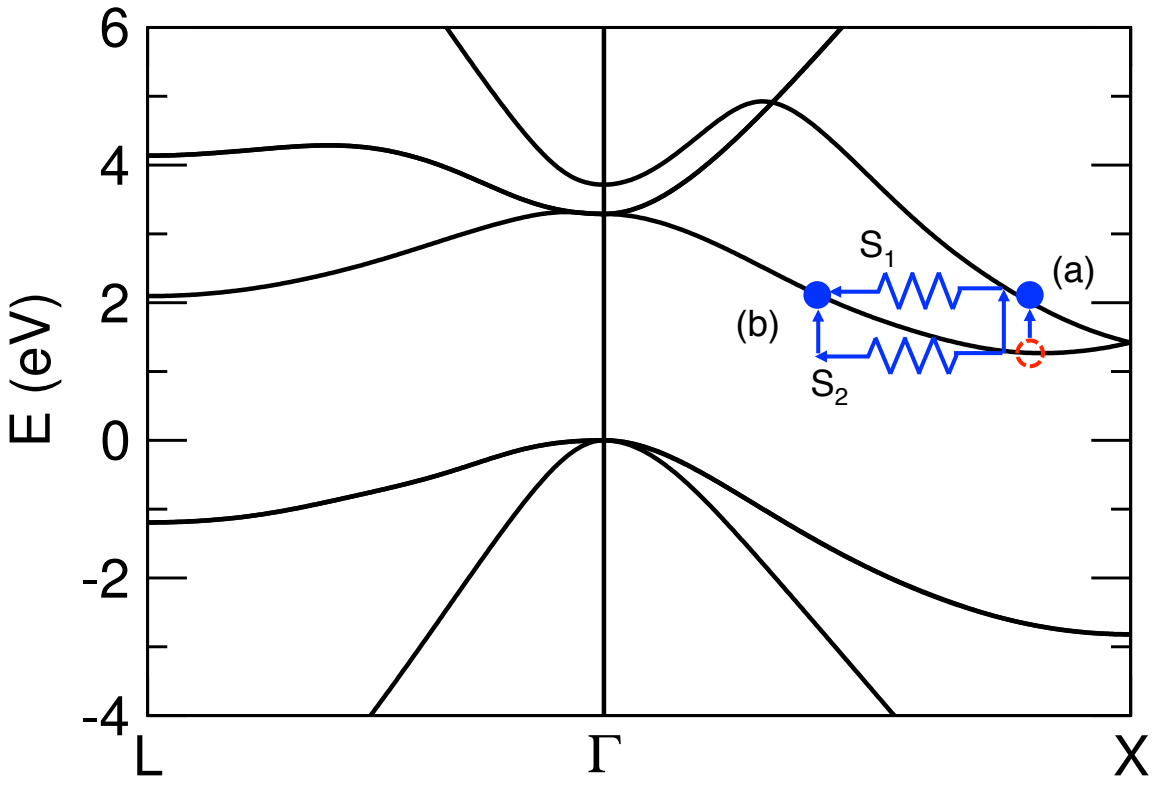

Figure 4.1: Si band structure depicting different free-carrier absorption processes: (a) direct and (b) indirect absorption. Indirect absorption can proceed along two paths with generalized optical matrix elements $\boldsymbol{S}_1$ and $\boldsymbol{S}_2$.

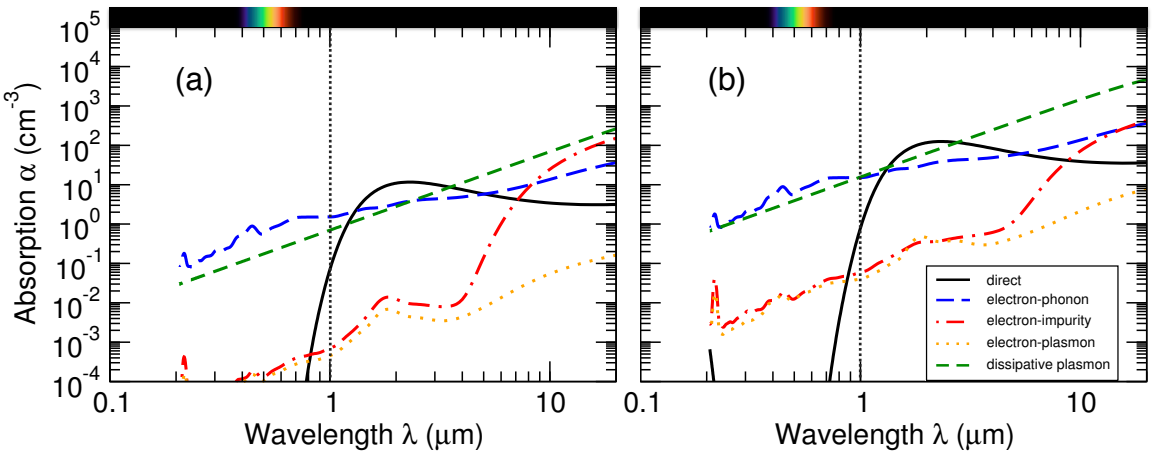

Figure 4.2: Contributions to the free-carrier absorption at the electron concentrations of (a) 10^{18}cm^{-3} and (b) 10^{19}cm^{-3} at 300K.

with norm-conserving pseudopotentials[113] and a plane-wave cutoff of 40 Ry as implemented in the Quantum-ESPRESSO code[40].

The quasiparticle band structure of Si was calculated using the one-shot GW method[65] and the BerkeleyGW code[1]. The static dielectric function was calculated with a 20 Ry plane-wave cutoff and extended to finite frequency using the generalized plasmon-pole model of Hybertsen and Louie[65]. The Coulomb-hole self-energy term was calculated using a sum over unoccupied bands up to 9 Ry above the valence band maximum using the static-remainder approach[66]. The quasiparticle energies were determined on an 8×8×8 grid and interpolated in the BZ using maximally localized Wannier function formalism[95, 96]. Subsequently, we interpolated the quasiparticle energies on a fine mesh of 120×120×120 to determine the direct absorption coefficient coefficient with Fermi's golden rule.

The phonon dispersion and electron-phonon coupling matrix elements were calculated for Si with density-functional perturbation theory[114] on a 40×40×40 grid of phonon $\boldsymbol{q}$ vectors in the first BZ. For each phonon vector the electron-phonon matrix elements were determined using electron wave functions at $\boldsymbol{k}$ and $\boldsymbol{k}+\boldsymbol{q}$ on an 8×8×8 grid. Imaginary part of the electron-phonon self-energies[115] was used for broadening of the δ function and the energy denominators. For the impurity scattering and plasmon scattering, the coupling matrix elements were calculated on the same grid of phonon $\boldsymbol{q}$ vectors. For indirect absorptions, we assume that all the free carriers are located at the conduction band minimum and thus eliminated the sum over $\boldsymbol{k}$ in Eq. 4.3, 4.7, and 4.8.

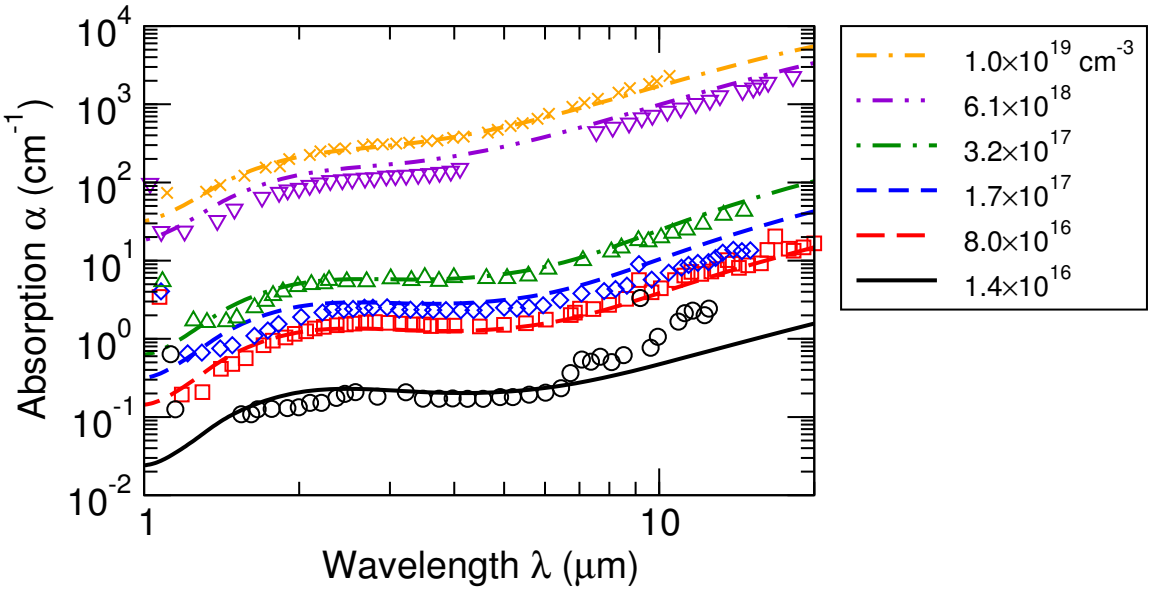

Figure 4.3: Calculated values (lines) for the free-carrier absorption coefficient are in very good agreement with the experimental results[3] (symbols) for n-type Si at 300K.

4.2 Results and Discussions

Figure 4.2 shows different contributions to free-carrier absorption in Si, including dissipative plasmon absorption, direct absorption, and phonon-, charged-impurity-, and plasmon-assisted indirect absorption, at two different carrier concentrations. The vertical dashed line indicates the calculated band gap of silicon (1.27 eV). Different absorption processes are found to dominate in different wavelength ranges. At a carrier concentration of 10^{18}cm^{-3} (FIG. 4.2(a)), the phonon-assisted absorption is a little larger than the dissipative plasmon absorption in the ultraviolet and visible range, while the other contributions are much smaller. At longer wavelengths below the band gap energy, the direct transition starts to dominate, and the dissipative plasmon and phonon-assisted absorption become comparable, about one order smaller than the direct transition. At even longer wavelengths and photon energies below 100 meV, the dissipative plasmon absorption dominates the absorption, and the charged-impurity assisted absorption also starts to have an important effect. When the carrier concentration is ten times larger, the curves seem to be shifted up together, approximately by a rigid shift.

Figure 4.3 compares the calculated free-carrier absorption coefficient of Si with experiment [3] at various electron concentrations. The calculated values are the sum of different contributions, including dissipative plasmon absorption, direct absorption, and phonon-, charged-impurity-, and plasmon-assisted indirect absorption. Our calculated values have good agreement with experiment at various wavelengths and electron concentrations. This

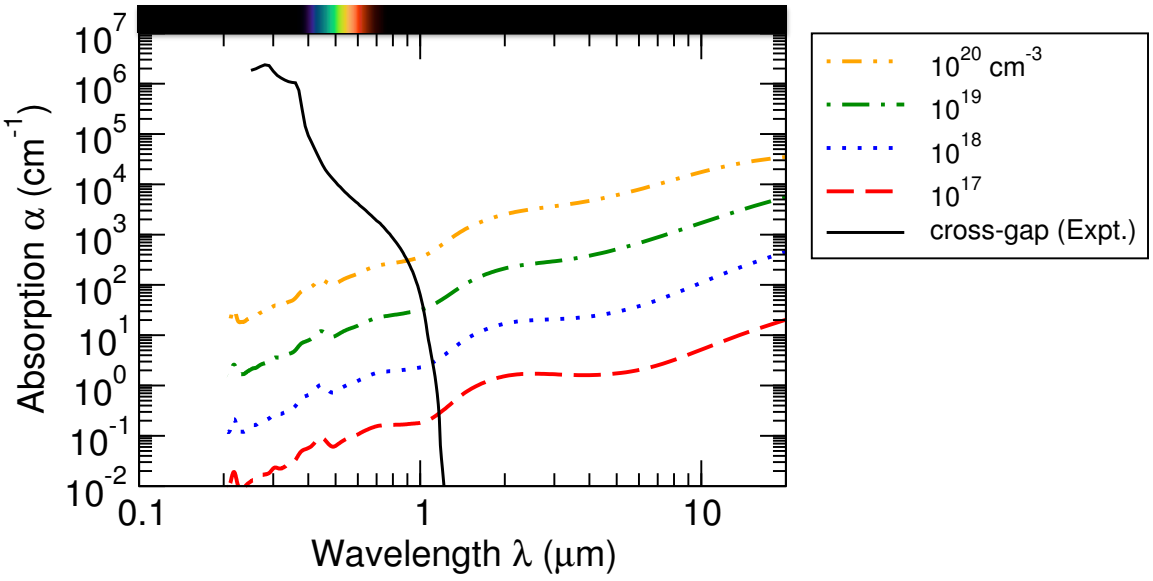

Figure 4.4: Calculated free-carrier absorption coefficient at different electron concentrations compared to cross-gap absorption from experiment[4].

convinces us that we correctly identified the most important absorption processes that contribute to the overall result.

When comparing theory to experiment, we focus on photon energies lower than the band gap of Si, as it is hard to separate the contribution of free-carrier absorption from that of cross-gap absorption in experiment for photon energies larger than the band gap. Since free-carrier absorption competes with cross-gap absorption while it does not generate electron-hole pairs, it is important to be able to predict the contribution of free-carrier absorption above the band gap and thus better understand the energy loss from it in Si solar cells. Figure 4.4 shows the calculated free-carrier absorption coefficient at different electron concentrations as well as the cross-gap absorption from experiment[4]. Free-carrier absorption is much smaller than cross-gap absorption at wavelengths smaller than or within the visible range, but it becomes comparable to or even larger than cross-gap absorption when the photon energy gets closer to the band gap of Si (photon wavelength of 800-1000 nm), especially at high doping concentrations. Therefore, heavily doped Si contacts in Si solar cells absorb a significant fraction of solar photons in the 800-1000 nm range through free-carrier absorption, which reduce the overall efficiency of solar cells by an amount depending on the doping and material thickness. Our calculated results can therefore be applied to model the absorption loss in silicon solar cells due to free-carrier absorption.

4.3 Conclusions

In summary, we discussed plasmon dissipative process, direct transition, and phonon-, charged-impurity-, and plasmon-assisted transitions in n-type Si. Each process creates different features at different wavelengths, which highlights the importance of first-principles calculations for the accurate determination of the free-carrier absorption coefficient. The calculated results are in good agreement with experiment and validates the successful identification of the dominant free-carrier absorption processes. Free-carrier absorption is found to be comparable or even larger than the cross-gap absorption at photon energies close to the band gap for heavily dopes Si, and is thus a nonnegligible source of energy loss in Si solar cells.

CHAPTER 5

Thermoelectric transport properties of p-type SnSe

We used density functional and many-body perturbation theory to calculate the quasiparticle band structures and electronic transport parameters of p-type SnSe both for the low-temperature *Pnma* and high-temperature *Cmcm* phases. The *Pnma* phase has an indirect band gap of 0.829 eV while the *Cmcm* has a direct band gap of 0.464 eV. Both phases exhibit multiple local band extrema within an energy range comparable to the thermal energy of carriers from the global extrema. We calculated the electronic transport coefficients as a function of doping concentration and temperature for single-crystal and polycrystalline materials to understand previous experimental measurements. The electronic transport coefficients are highly anisotropic and are strongly affected by bipolar transport effects at high temperature. Our results indicate that SnSe exhibits optimal thermoelectric performance at high temperature when doped in the 10^{19}–10^{20} cm^{-3} range.

Thermoelectric materials enable the direct conversion of heat to electricity and can be used to recover usable energy from waste heat. The efficiency of thermoelectric energy conversion is determined by the dimensionless figure of merit of the material, $ZT = S^2\sigma T/(\kappa_{\mathrm{L}} + \kappa_{\mathrm{el}})$, where S is the Seebeck coefficient, σ is the electrical conductivity, T is the absolute temperature, and κ_{L} and κ_{el} are the lattice and electronic contributions to the thermal conductivity. High ZT values occur in materials with high electrical conductivity, high Seebeck coefficient, and low thermal conductivity, such as p-type IV-VI compounds (i.e., PbSe, PbTe, and their alloys) with reported ZT values as high as 1.8.[15, 14, 116] SnSe is another IV-VI compound that has attracted little attention as a thermoelectric material. Recently, Zhao *et al.* reported figure-of-merit values as high as 2.6 in single-crystal samples of unintentionally doped p-type SnSe.[5] SnSe undergoes a phase transition at 813 K from the low-temperature phase (*Pnma* space group) to the high-temperature *Cmcm* phase (Fig. 5.1). The highest ZT values were found near and above this phase-transition temperature of 813 K.

In this work we present the quasiparticle band structures and thermoelectric transport coefficients of both the low-temperature (*Pnma*) and high-temperature (*Cmcm*) phases of SnSe. In Section 6.1 we discuss our first-principles methodology for the calculation of the band structures and transport coefficients. In Section 6.2 we present and discuss our findings. In Section 6.2.1 we report values for the band gaps, band-extrema locations, and carrier effective masses for both phases. We found multiple local band extrema that lie close in energy to the the band edges and need to be considered when calculating the thermoelectric transport properties. In Section 5.2.2 we calculate the Seebeck coefficient and electrical conductivity of both SnSe phases and compare to recent experimental measurements. In Section 5.2.3 we report the carrier-density and temperature dependence of the electronic transport coefficients. The transport coefficients are very different along the perpendicular direction (*a* axis) and the two in-plane directions (*b* and *c* axes). Bipolar transport effects were found to play an important role in carrier transport at high temperatures. We predict that SnSe shows good thermoelectric performance at high temperature when doped in the 10^{19}–10^{20} cm^{-3} range. This work has been published in Nano Letters.[26]

5.1 Methodology

We studied the electronic properties of SnSe using first-principles calculations based on density functional and many-body perturbation theory. We calculated the ground-state charge density and electronic wave functions using the generalized gradient approximation[38, 91] for the exchange-correlation potential. We used the plane-wave pseudopotential method[63]

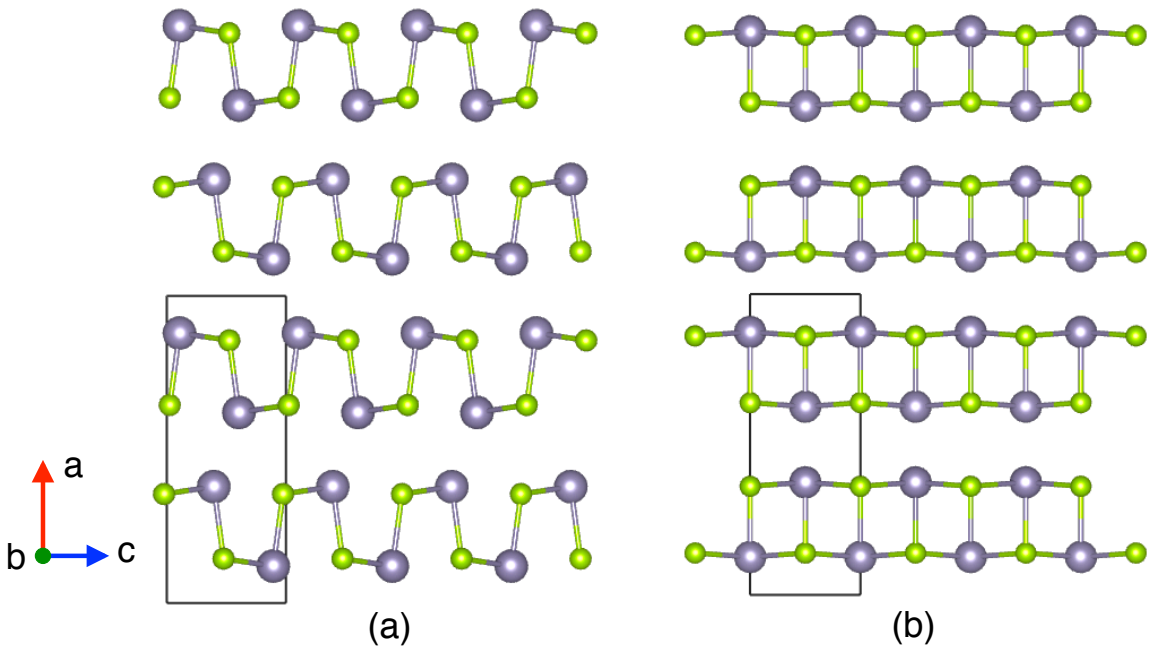

Figure 5.1: Crystal structures of (a) the low-temperature (*Pnma*) phase and (b) the high-temperature (*Cmcm*) phase of SnSe. The black borders indicate the conventional unit cells of the two phases.

with norm-conserving pseudopotentials[113] and a plane-wave cutoff of 200 Ry as implemented in the Quantum-ESPRESSO code[40]. The electrons from the outermost valence shell (5*s* and 5*p*) as well as those from the semicore atomic shell (4*s*, 4*p*, and 4*d*) are included for Sn. The crystal structures of the two phases are shown in Fig. 5.1 along the *b* axis.

We used the experimentally measured values for the lattice vectors and atomic positions of SnSe at 300K for the low-temperature *Pnma* phase (a = 11.50 Å, b = 4.45 Å, c = 4.153 Å) and at 813 K for the high-temperature *Cmcm* (a = 4.31 Å, b = 6.24 Å, c = 4.31 Å) phase.[117] The *Cmcm* phase, which has higher symmetry than the *Pnma* phase, was studied using its primitive 4-atom unit cell instead of the conventional 8-atom cell (Fig. 5.1). The Brillouin zone was sampled using a Monkhorst-Pack grid[118] of $6\times6\times2$ for the low-temperature phase and $6\times6\times4$ for the high-temperature phase.

We calculated the quasiparticle band structure of SnSe using the one-shot GW method[65] and the BerkeleyGW code[1]. The static dielectric function was calculated with a 20 Ry plane-wave cutoff and extended to finite frequency using the generalized plasmon-pole model of Hybertsen and Louie[65]. The Coulomb-hole self-energy term was calculated using a sum over unoccupied bands up to 16 Ry above the valence band maximum using the static-remainder approach[66]. Corrections due to spin-orbit coupling interaction[93]

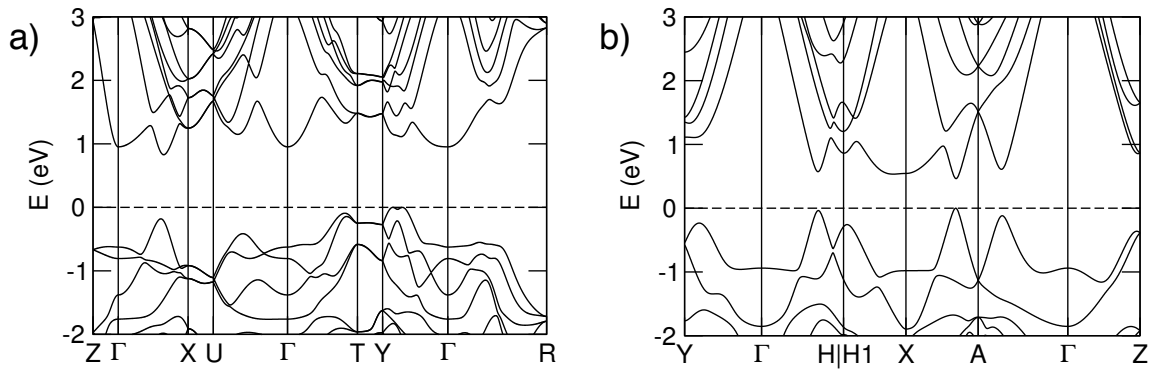

Figure 5.2: Quasiparticle band structures of (a) the low-temperature (*Pnma*) phase and (b) the high-temperature (*Cmcm*) phase of SnSe. *Pnma*-SnSe has an indirect band gap of 0.829 eV, while the band gap of *Cmcm*-SnSe is direct with a magnitude of 0.464 eV. Both phases exhibit multiple local band extrema that lie close in energy to the global extrema.

were calculated in a non-self-consistent way using plane waves up to a cut-off energy of 50 Ry. We used the maximally localized Wannier function formalism[95, 96] to interpolate the quasiparticle energies and spin-orbit coupling matrix elements to arbitrary points in the first Brillouin zone[119]. Subsequently, we interpolated the quasiparticle energies on fine meshes in the first Brillouin zone ($120\times120\times60$ for *Pnma*-SnSe and $120\times120\times80$ for *Cmcm*-SnSe) to determine the thermoelectric transport coefficients of p-type SnSe with the Boltzmann transport equation in the constant-relaxation-time approximation.[120, 121]

5.2 Results and discussion

5.2.1 Band structure

The calculated band structures of *Pnma*-SnSe and *Cmcm*-SnSe, including quasiparticle and spin-orbit coupling corrections, are shown in Figs. 5.2(a) and 5.2(b). The band gap of *Pnma*-SnSe is found to be indirect with a magnitude of 0.829 eV, while *Cmcm*-SnSe has a direct band gap with a magnitude of 0.464 eV. The Brillouin-zone positions, energies, and multiplicities of the band extrema of *Pnma*-SnSe and *Cmcm*-SnSe are summarized in Table 5.1. All energies are referenced to the valence-band maximum (VBM) of each phase. In *Pnma*-SnSe, the position of the VBM is at (0.00, 0.35, 0.00) along the Γ–Y direction of the first Brillouin zone. There is also a local valence-band maximum at (0.00, 0.42, 0.00) that lies within 1 meV lower in energy than the VBM. The conduction-band minimum (CBM) is located at (0.33, 0.00, 0.00) along the Γ–X direction. The calculated band gap (0.829 eV) is in good agreement with optical-absorption measurements (0.86 eV[5] and

0.898 eV[99]). We note that the optical-absorption measurements include excitonic effects that were not included in our calculations. The smallest direct transition energy was found to be 1.03 eV and occurs at (0.32, 0.00, 0.00), which is close to the CBM location. In *Cmcm*-SnSe, both the VBM and CBM are located at (0.34, 0.50, 0.00) along the X–A direction. In addition, the band structure exhibits a local valence-band maximum, VBM1 at (0.00, 0.20, 0.39) along the Γ–H direction, located just 31 meV lower in energy than the global VBM. A local conduction-band minimum, CBM1 is found at (0.00, 0.54, 0.08) along the X–H1 direction, located 70 meV higher in energy than the global CBM.

Figures 5.3 and 5.4 show a set of constant-energy surfaces of the valence and conduction bands for both SnSe phases plotted within the first Brillouin zone. The plots demonstrate the multiple local extrema for both phases. The local extrema reside within an energy range of $k_{\mathrm{B}}T$ (k_{B} is the Boltzmann constant) from the band edges for temperatures near the phase-transition temperature (813 K) around which the highest ZT values have been reported. Therefore, all local extrema need to be taken into account when analyzing the transport properties of n-type and p-type SnSe.

The effective-mass parameters are also reported for both phases in Table 5.1. To determine the principal axes of the effective mass tensors. we fit the energy isosurfaces using a three-dimensional ellipsoid function. Our results show that the a, b, and c crystallographic axes coincide with the principal axes of the effective mass ellipsoids within less than two degrees. The effective mass at each extremum is highly anisotropic. With the exception of the CBM1 local minimum of the *Cmcm* phase, the effective mass has a larger value along the a axis, perpendicular to the atomic layers, than either of the in-plane directions b and c. This is due to the two-dimensional nature of the material, which favors electron transport within the atomic layers than perpendicular to them. Although the CBM has a larger effective mass along the *a* axis than the VBM for both phases, electrons have a smaller density-of-states effective mass than holes around the band gap based on the density of states plot (Fig. 5.5). This is because the energy window over which the conduction band is parabolic is narrower than 10 meV above the CBM, while the conduction band shows significant nonparabolicity and warping at higher energies. For this reason, the transport properties are not simply predicted from the effective-mass model, and their calculation requires the full band structure in the entire Brillouin zone.

5.2.2 Transport coefficients

Figures 5.6(a) and 5.6(b) show the calculated Seebeck coefficients for single-crystal *Pnma*-SnSe and *Cmcm*-SnSe as a function of crystal direction and temperature. The calculated

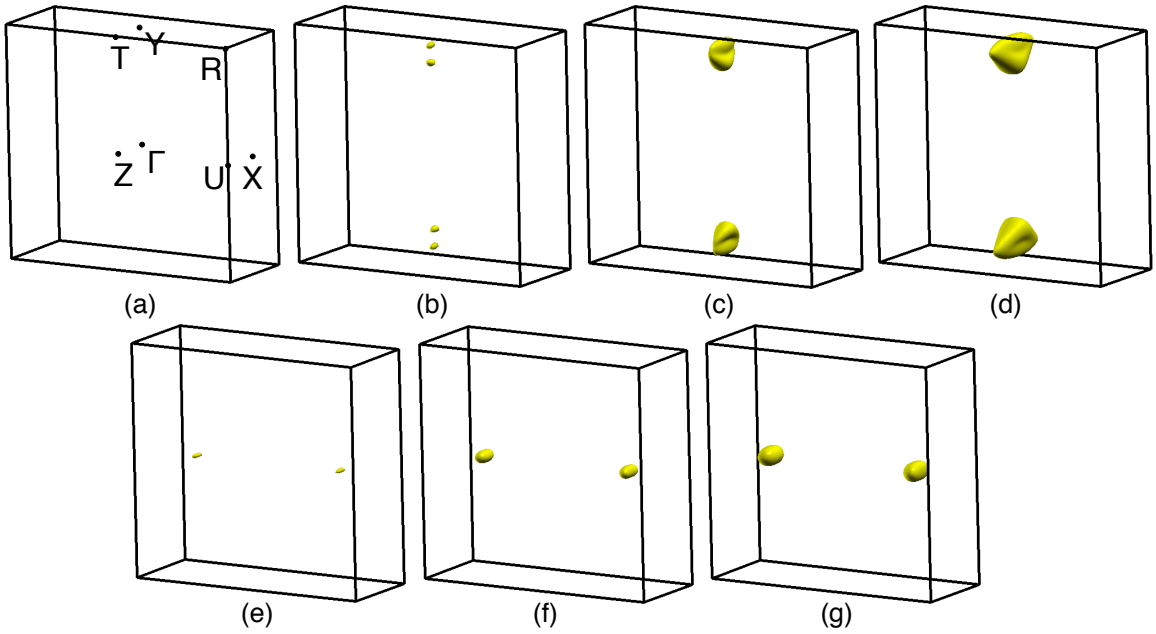

Figure 5.3: (a) The first Brillouin zone of the low-temperature (*Pnma*) phase of SnSe. (b∼d) Constant-energy surfaces of the highest valence band with an energy of (b) 10 meV, (c) 50 meV, (d) 100 meV lower than the VBM energy. (e∼g) Constant-energy surfaces of the lowest conduction band with an energy of (e) 10 meV, (f) 50 meV, (g) 100 meV higher than the CBM energy.

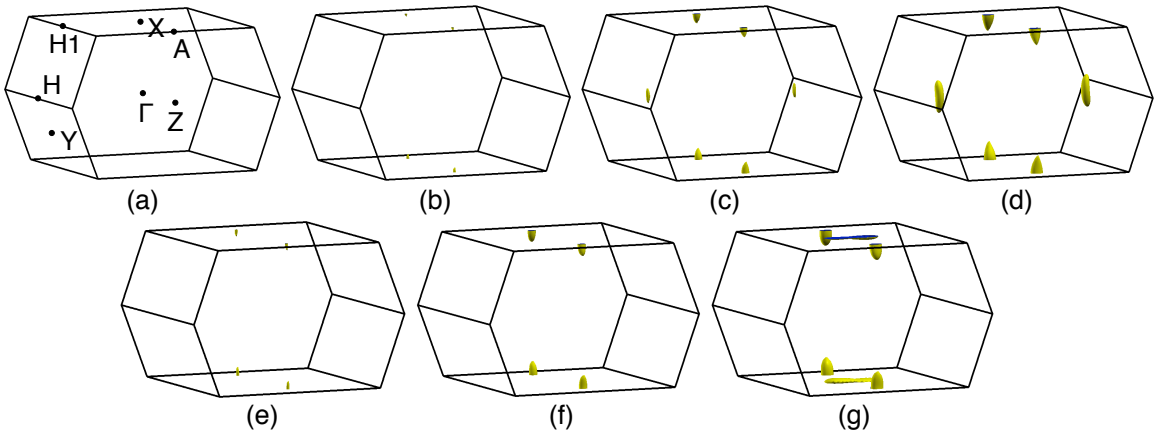

Figure 5.4: (a) The first Brillouin zone of the high-temperature (*Cmcm*) phase of SnSe. (b∼d) Constant-energy surfaces of the highest valence band with an energy of (b) 10 meV, (c) 50 meV, (d) 100 meV lower than the VBM energy. (e∼g) Constant-energy surfaces of the lowest conduction band with an energy of (e) 10 meV, (f) 50 meV, (g) 100 meV higher than the CBM energy.

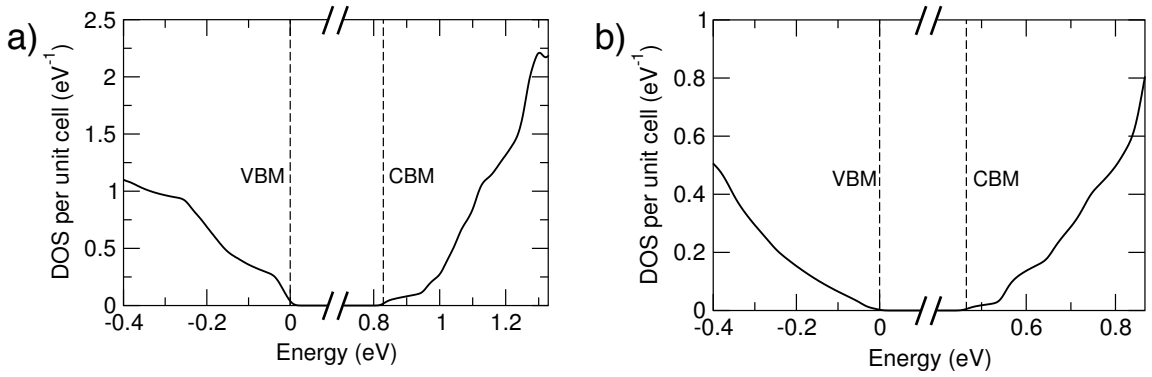

Figure 5.5: Density of states of (a) the low-temperature (*Pnma*) phase and (b) the high-temperature (*Cmcm*) phase of SnSe around the band gap.

data are also compared to the experimental values reported by Zhao *et al.* for single-crystal samples[5]. For these calculations we assumed a doping concentration (i.e., net free-carrier concentration) of 6×10^{17} cm^{-3}, which agrees with the experimental Hall measurements at 300 K.[5] Although the two phases of SnSe are stable in different temperature regimes, we present theoretical results for the transport coefficients for both phases at all temperatures for completeness. In the 300–600 K temperature range the calculated Seebeck coefficients for the *Pnma* phase increase with temperature and are in good agreement with the experimental data [Fig. 5.6(a)]. For temperatures in the range of 600–813 K electrons are thermally excited across the gap and induce bipolar transport, which reduces the Seebeck coefficient. Our theoretical Seebeck-coefficient data for the *Pnma* phase along the b and c axes are larger than experiment in this temperature regime because our theory predicts that the onset of bipolar transport occurs at higher temperatures than experiment [Fig. 5.6(a)]. This is because we have not included the effect of temperature on the calculated band structure, which in general decreases the band gap with increasing temperature and reduces the temperature onset of bipolar transport. The theoretical Seebeck coefficient for the *Pnma* phase along the a axis decreases rapidly as a function of temperature above 600 K and eventually changes sign around 840 K, which is above the phase-transition temperature of 813 K. We attribute the rapid decrease and sign reversal of the Seebeck coefficient along the a axis in this temperature range to the increasing negative contribution of thermally excited electrons to the Seebeck coefficient under bipolar-transport conditions. The calculated Seebeck coefficient data for the *Cmcm* phase in Fig. 5.6(b) show that bipolar transport sets in at lower temperatures than in *Pnma*-SnSe because *Cmcm*-SnSe has a lower band gap. Moreover, our calculations predict that for the experimental doping level of 6×10^{17} cm^{-3} the sign of the Seebeck coefficient along the a direction becomes negative for temperatures above 600 K, and in particular in the 813–1000 K temperature range where the *Cmcm* phase

is stable. The experimental Seebeck coefficient values for the *Cmcm* phase along the b and c directions are larger than our calculated results, while no sign reversal of the Seebeck coefficient along the a direction is observed experimentally. We discuss the potential origins of this discrepancy later in this Section.

We also calculated the Seebeck coefficients of polycrystalline *Pnma*-SnSe as a function of carrier density and temperature and compared to experiment. The Seebeck coefficients for polycrystalline *Pnma*-SnSe are evaluated by calculating the directional average along the *a*, *b*, and *c* axes weighted by the electrical conductivity according to Parker's work[122]: $S_{\text{avg}} = (S_a\sigma_a + S_b\sigma_b + S_c\sigma_c)/(\sigma_a + \sigma_b + \sigma_c)$. This equation results from the directional average of the transport tensors $\boldsymbol{L}^{(0)}$ and $\boldsymbol{L}^{(1)}$ [121]. The calculated Seebeck data are plotted as a function of hole concentration for two temperatures (300 K and 750 K) in Fig. 5.7(a). The calculated coefficients are found to be in very good agreement with the recent experimental work by Chen *et al.* for p-type polycrystalline SnSe doped with Ag.[6] As the hole concentration increases from 10^{17} to 10^{20} cm^{-3}, the Fermi energy decreases down to 83 meV and 33 meV below the VBM at 300K and 750K, correspondingly. Figure 5.7(b) indicates the states within the energy window of $\pm$ k$_B$T around the Fermi energy for a hole concentration of 10^{20} cm^{-3} at 300 K and 750 K for *Pnma*-SnSe along the Y–Γ–X path, which includes the three topmost local valence band maxima. The Figure shows that topmost two local valence-band maxima have a larger contribution to electronic transport than the third highest valence-band maximum both at 300 K and at 700 K.

Figures 5.6(c) and 5.6(d) show the calculated electrical conductivity divided by the scattering time for the *Pnma* and *Cmcm* phases of single-crystal SnSe as a function of temperature and crystal direction. The net free-carrier concentration is taken to be 6×10^{17} cm^{-3}, which is the same as the calculation of Seebeck coefficients. The electrical conductivity is similar along the *b* and *c* axes but much smaller along the *a* axis. This trend is in good agreement with experiment[5] and stems from the anisotropic two-dimensional nature of the material. In the 300–700 K temperature range the calculated data for the *Pnma* phase do not depend strongly on temperature, indicating that the free-carrier concentrations do not change substantially in this temperature regime. For temperatures above 700 K bipolar transport sets in and both the number of thermally excited carriers and the electrical conductivity increase exponentially with temperature. The electrical conductivity for the *Cmcm* phase has a similar behavior to the *Pnma* phase, with the difference that due to the smaller band gap of *Cmcm*-SnSe bipolar transport starts to occur at lower temperatures around 500 K. The experimental data for the *Pnma* phase show a temperature dependence qualitatively similar to our calculations. The electrical conductivity decreases weakly with temperature in the 300–550 K range, while for temperatures above 550 K it

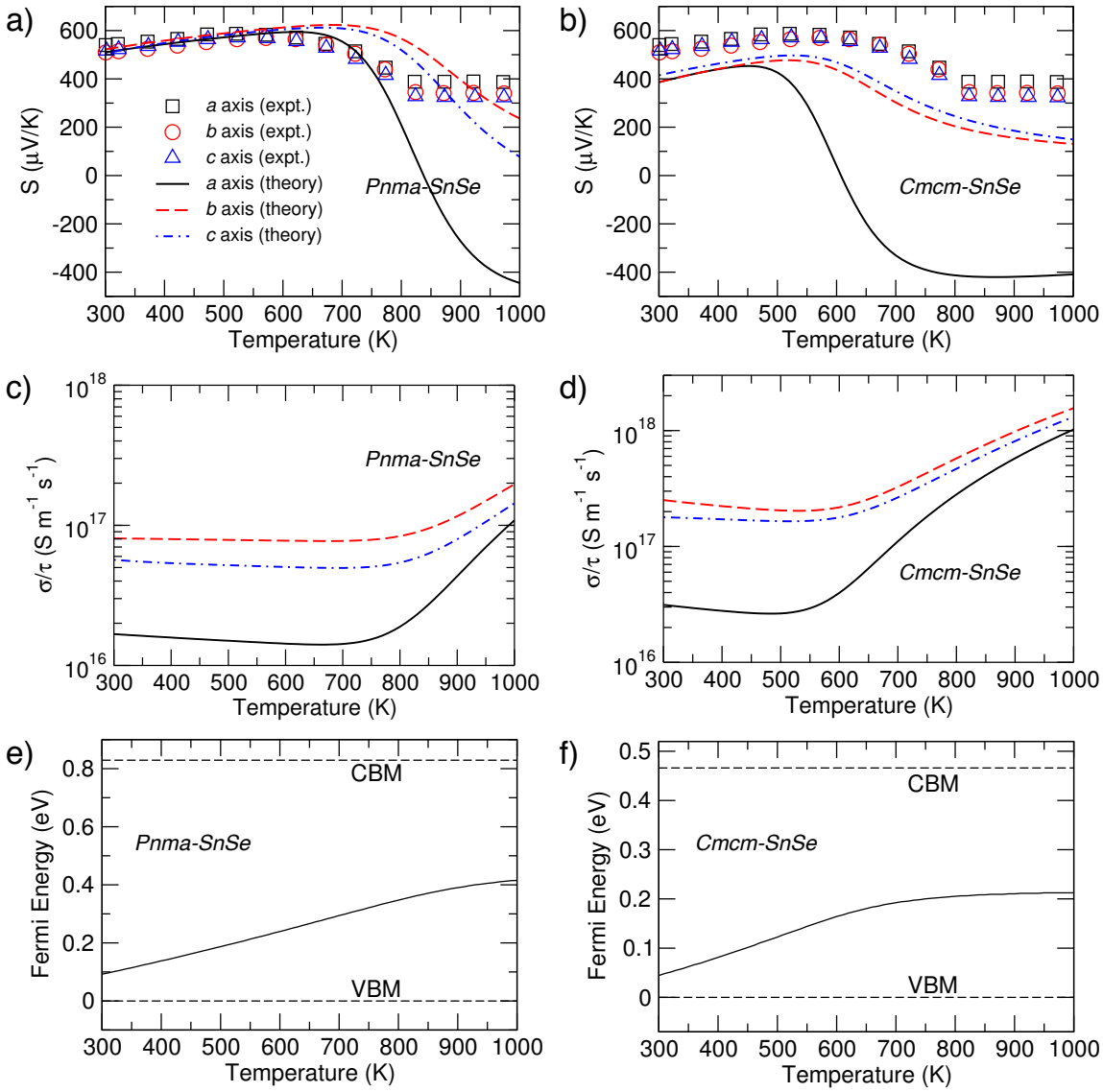

Figure 5.6: Calculated values (lines) for the Seebeck coefficient S (a, b), the electrical conductivity divided by the constant scattering time σ/τ (c, d), and the Fermi energy (e, f) of the low-temperature (*Pnma*) phase and high-temperature (*Cmcm*) phase of SnSe for a doping concentration (net free-carrier concentration) of $6.0\times10^{17}\text{cm}^{-3}$, which matches the experimental Hall coefficient measurements at 300 K in Zhao's work[5].

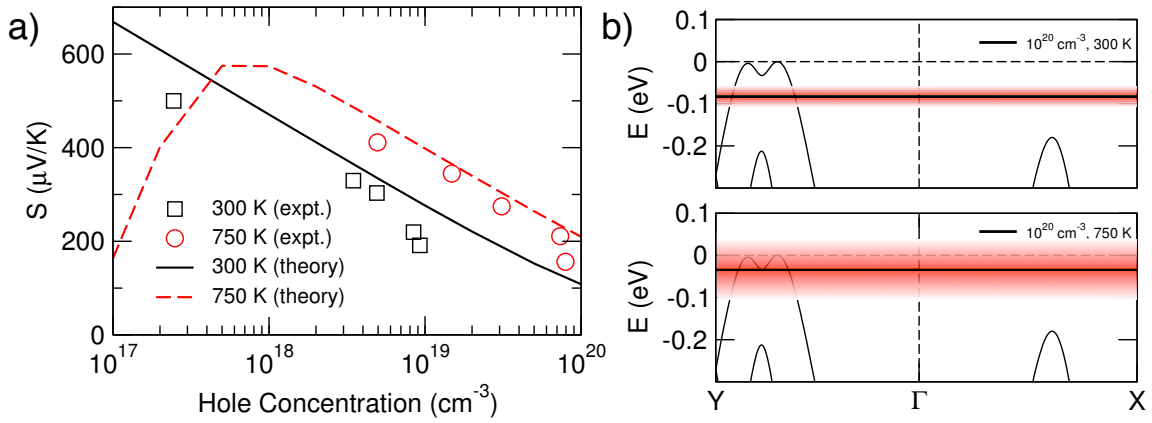

Figure 5.7: (a) Directionally averaged Seebeck coefficient of *Pnma*-SnSe as a function of net free-carrier concentration and temperature. The calculated data are in very good agreement with the experimental results for polycrystalline SnSe reported in Chen's work[6]. (b) Band structure of *Pnma*-SnSe along the Y–Γ–X path, which includes the three topmost local valence band maxima. The shaded regions indicate the energy window of $\pm$ k_BT around the Fermi energy for a hole concentration of 10^{20} cm^{-3} at 300 K (top panel) and 750 K (bottom panel).

increases exponentially as carriers are thermally excited across the gap. Remarkably, the experimental conductivity data for the *Cmcm* phase show a weak decrease with temperature above the phase-transition temperature of 813 K, in sharp contrast with the exponential increase observed for temperatures above 500 K in our calculations.

Figures 5.6(e) and 5.6(f) show the calculated Fermi energy for the *Pnma* and *Cmcm* phases of single-crystal SnSe as a function of temperature for a net free-hole concentration of 6×10^{17} cm^{-3}. The Fermi energy lies within the band gap for both phases at 300 K (0.1 eV above the VBM for *Pnma* and 0.05 eV above the VBM for *Cmcm*). As the temperature increases, electrons get thermally excited from the valence to the conduction band and the Fermi energy shifts towards the middle of the band gap. The Fermi energy of the *Cmcm* phase stabilizes near the middle of the gap for temperatures above 700 K, which signifies a comparable concentration of free electrons and holes and is consistent with the sign reversal of the Seebeck coefficient at these high temperatures. The *a* direction exhibits much stronger bipolar transport effects than the other two directions for both the *Pnma* and the *Cmcm* phases because the band velocity of the bottom conduction band along the *a* axis is much larger than that of the top valence band. We note that electrons have larger mobility than holes along the *a* axis despite their larger effective mass due to the warping of the bottom conduction band, as discussed in Section 6.2.1.

There are several discrepancies between our theoretical calculations and the experimental data for the Seebeck coefficient and electrical conductivity of SnSe above the phase-

transition temperature of 813 K. Although the calculated Seebeck coefficients are in very good agreement with the low-temperature *Pnma* phase experimental data, our calculations do not reproduce the approximately constant Seebeck coefficients reported experimentally for the *Cmcm* phase above 813 K.[5] Moreover, the origin of the experimentally observed behavior of the electrical conductivity for the *Cmcm* phase is not clear. We expect the number of thermally excited carriers for the *Cmcm* phase to increase exponentially with temperature above 500 K due to bipolar transport. It is not obvious what is the cause of the discrepancy between theory and experiment at high temperatures. On the one hand, the disagreement could be attributed to limitations of our computational method. Our calculations assume the relaxation time to be constant, isotropic, and the same for both electrons and holes. The relaxation time may be very different between electrons and holes, and it may also vary with direction, energy, and temperature. Moreover, we have not explicitly considered temperature effects on the energy eigenvalues. However, the good agreement between our calculated data and experiment for single-crystal and polycrystalline *Pnma*-SnSe suggests that our calculated band structures are accurate and the constant relaxation time is a valid approximation. On the other hand, the increasing temperature and the phase transition may affect the nature or concentration of defects and dopant impurities in the material and thus the net free-carrier concentration. Indeed, it is hard to identify a different reason why the conductivity does not continue to increase exponentially with temperature above the transition to the lower-band-gap *Cmcm* phase as reported experimentally.[5] Further evidence for this point is provided by our data for the upper limit of ZT discussed later.

5.2.3 Carrier-density and temperature dependence of transport coefficients

To further explore the optimal temperature and carrier concentration for the best thermoelectric performance, we calculated the thermoelectric transport properties of both *Cmcm* and *Pnma* phases of p-type SnSe as a function of temperature and net free-carrier concentration. Figure 5.8 shows the Seebeck coefficient as a function of temperature and carrier concentration along the *a*, *b*, and *c* axes. In the 300–600 K range the Seebeck coefficient data for the *Pnma*-SnSe phase are almost isotropic and increase with temperature. In this temperature range the Seebeck coefficients decrease at higher carrier concentrations due to the reduction of the asymmetry of the density of states around the Fermi level for higher doping levels. As temperature increases above 600 K, bipolar transport occurs and reduces the Seebeck coefficients. The bipolar transport sets in at lower temperatures for lower car-

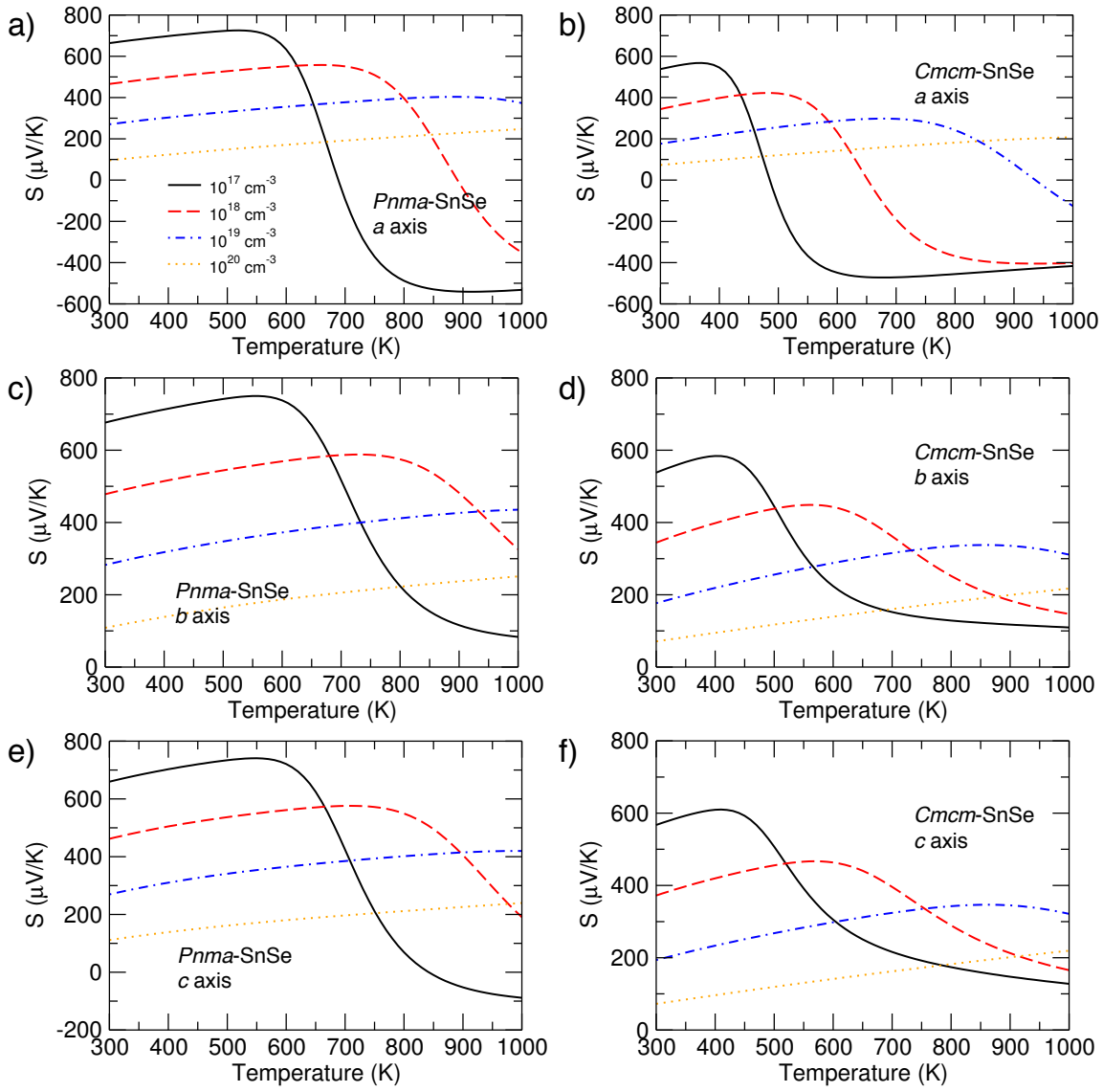

Figure 5.8: Seebeck coefficient as a function of temperature and carrier concentration for the low-temperature (*Pnma*) (a, c, e) and high-temperature (*Cmcm*) phases (b, d, f) of SnSe along the *a*, *b*, and *c* axes of the crystal structure. The Seebeck coefficients for the *Pnma*-SnSe phase are almost isotropic at low temperatures. Bipolar transport reduces the Seebeck coefficients at high temperatures in both phases, and even changes its sign from positive to negative at low carrier concentrations.

rier concentrations. The temperature that the bipolar transport begins increases from 550 K to 700 K as the carrier concentration increases from 10^{17} cm^{-3} to 10^{18} cm^{-3}. For a net free-carrier concentration of 10^{17} cm^{-3} the Seebeck coefficient along *a* and *c* axes changes sign as temperature increases, which implies that the thermally excited electrons start to dominate transport and the character of semiconductor changes from p-type to n-type. For temperatures above 813 K, SnSe transitions to the *Cmcm* phase and the calculated Seebeck coefficients are smaller than the *Pnma* phase. This is explained by the more important role of bipolar transport in the high-temperature *Cmcm* phase since it has a smaller band gap than the *Pnma* phase.

The calculated electrical conductivity of p-type SnSe divided by the scattering time (σ/τ) is plotted in Fig. 5.9 as a function of crystal phase, crystal direction, net free-carrier concentration, and temperature. The electrical conductivity is similar along the *b* and *c* axes but it is much smaller along the *a* axis. The thermally excited carriers dominate transport and the electrical conductivity increases exponentially with temperature for temperatures above the onset of bipolar transport. The temperature onset of bipolar transport increases as the doping concentration increases because a larger number of thermally excited carriers is needed to overcome the contribution by the doping carrier concentration to the electrical conductivity. For temperatures above the phase transition (i.e., greater than 813 K) the *Cmcm* phase is found to have much larger electrical conductivity than the *Pnma* phase because of the more important role of bipolar transport for *Cmcm*-SnSe.

The power factor of *Pnma* and *Cmcm* SnSe divided by the scattering time is evaluated according to $\mathrm{PF}/\tau = S^2\sigma/\tau$ and is shown as a function of crystal direction, temperature, and net free-carrier density in Fig. 5.10. The power factor shows dips along the a and c axes because the Seebeck coefficient changes sign from positive to negative and takes a zero value at the dip position. The highest values are observed along the *b* axis, while the values are slightly smaller along the *c* axis and much smaller along the *a* axis. This trend [$\mathrm{PF}(b) > \mathrm{PF}(c) > \mathrm{PF}(a)$] agrees with the experimental observations.[5] For high doping concentrations the power factor increases with increasing temperature. The highest power factor is found for the highest carrier concentration (10^{20} cm^{-3}) at the highest temperature (1000 K).

Figure 5.11 shows the electron contribution to the thermal conductivity divided by scattering time ($\kappa_{\mathrm{el}}/\tau$) for the two phases and the three crystal directions as a function of net free-carrier density and temperature. The electron thermal conductivity increases with increasing temperature and doping concentration. It takes higher values along the in-plane b and c directions than the perpendicular a direction, and it shows bipolar transport behavior similar to the electrical conductivity.

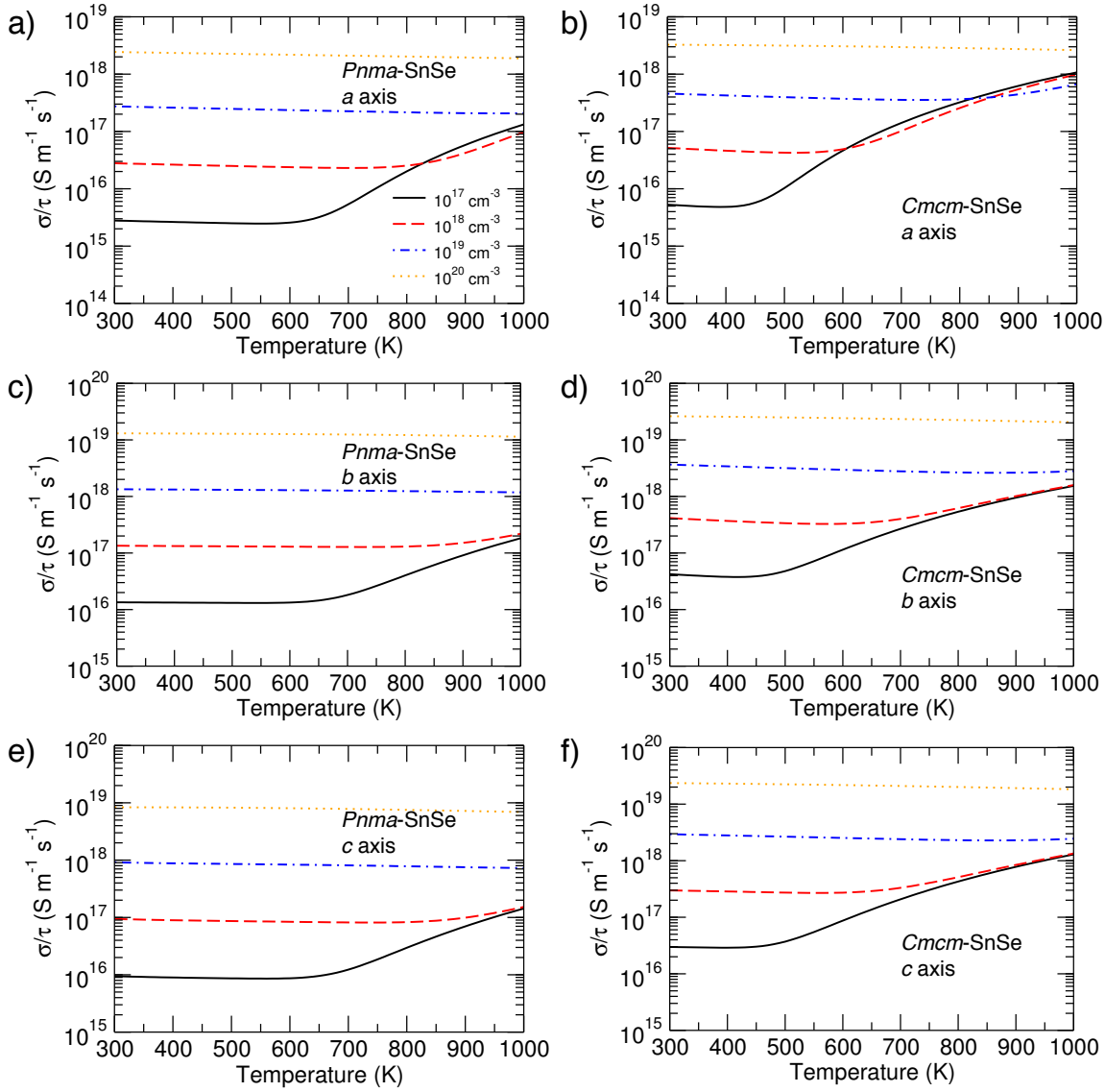

Figure 5.9: Electrical conductivity divided by the scattering time (σ/τ) as a function of temperature and carrier concentration for the low-temperature (*Pnma*) (a, c, e) and high-temperature (*Cmcm*) phases (b, d, f) of SnSe along the *a*, *b*, and *c* axes of the crystal structure. The electrical conductivity is similar along the *b* and *c* axes but it is much smaller along the *a* axis. The *Cmcm* phase is found to have larger electrical conductivity than the *Pnma* phase above 813 K (phase-transition temperature) because of the more important role of bipolar transport for *Cmcm*-SnSe.

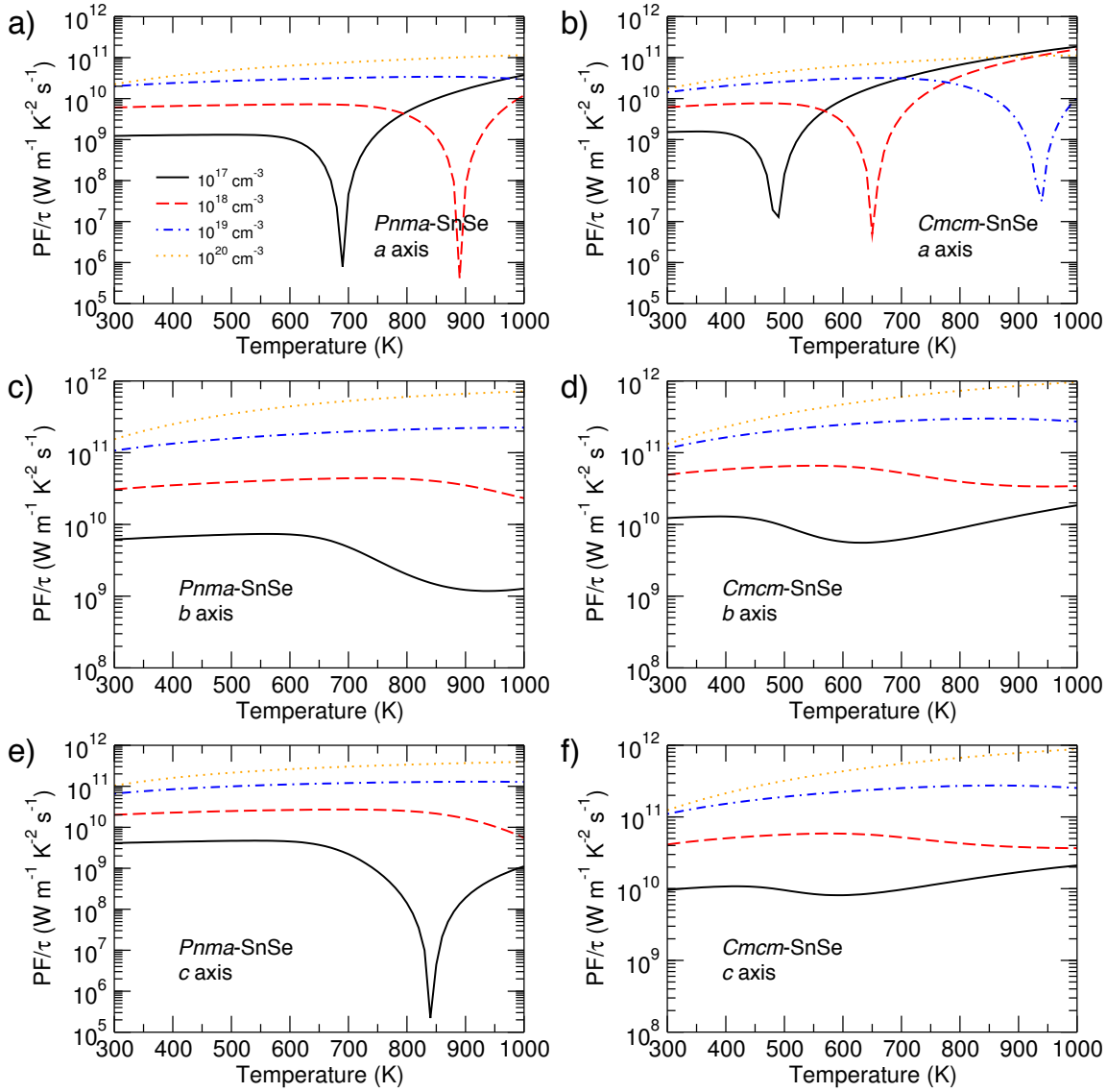

Figure 5.10: Power factor (PF) divided by the scattering time as a function of temperature and carrier concentration for the low-temperature (*Pnma*) (a, c, e) and high-temperature (*Cmcm*) phases (b, d, f) of SnSe along the *a*, *b*, and *c* axes of the crystal structure. The power factor shows dips along the a and c axes because the Seebeck coefficient changes sign from positive to negative and takes a zero value at the dip position. The highest values are observed along the *b* axis. The highest power factor is found for the highest carrier concentration (10^{20} cm^{-3}) at the highest temperature (1000 K).

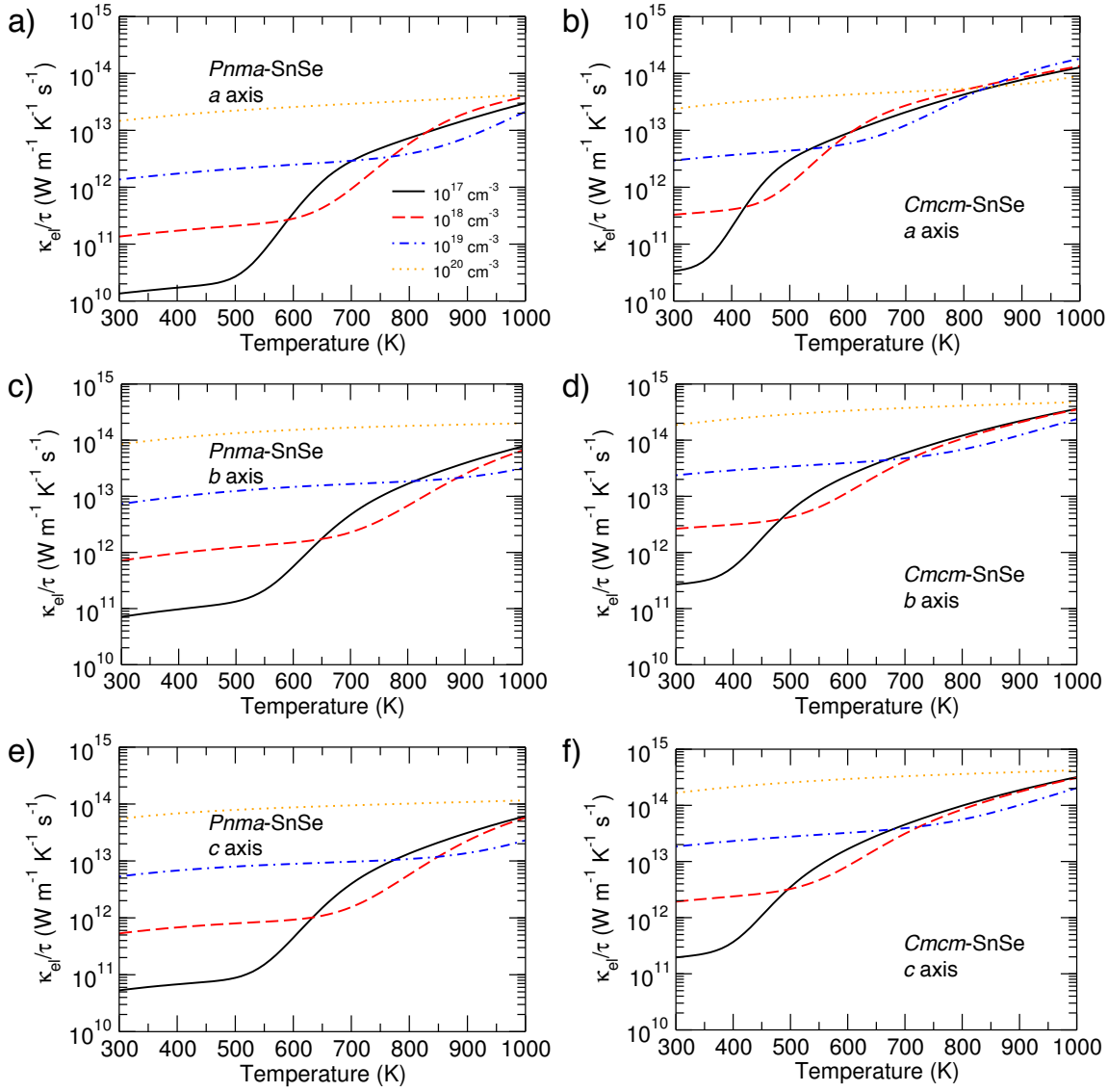

Figure 5.11: Electronic component of the thermal conductivity divided by the scattering time as a function for the low-temperature (*Pnma*) (a, c, e) and high-temperature (*Cmcm*) phases (b, d, f) of SnSe along the *a*, *b*, and *c* axes of the crystal structure. The electron thermal conductivity increases with increasing temperature and doping concentration. It takes higher values along the in-plane b and c directions than the perpendicular a direction, and it shows bipolar transport behavior similar to the electrical conductivity.

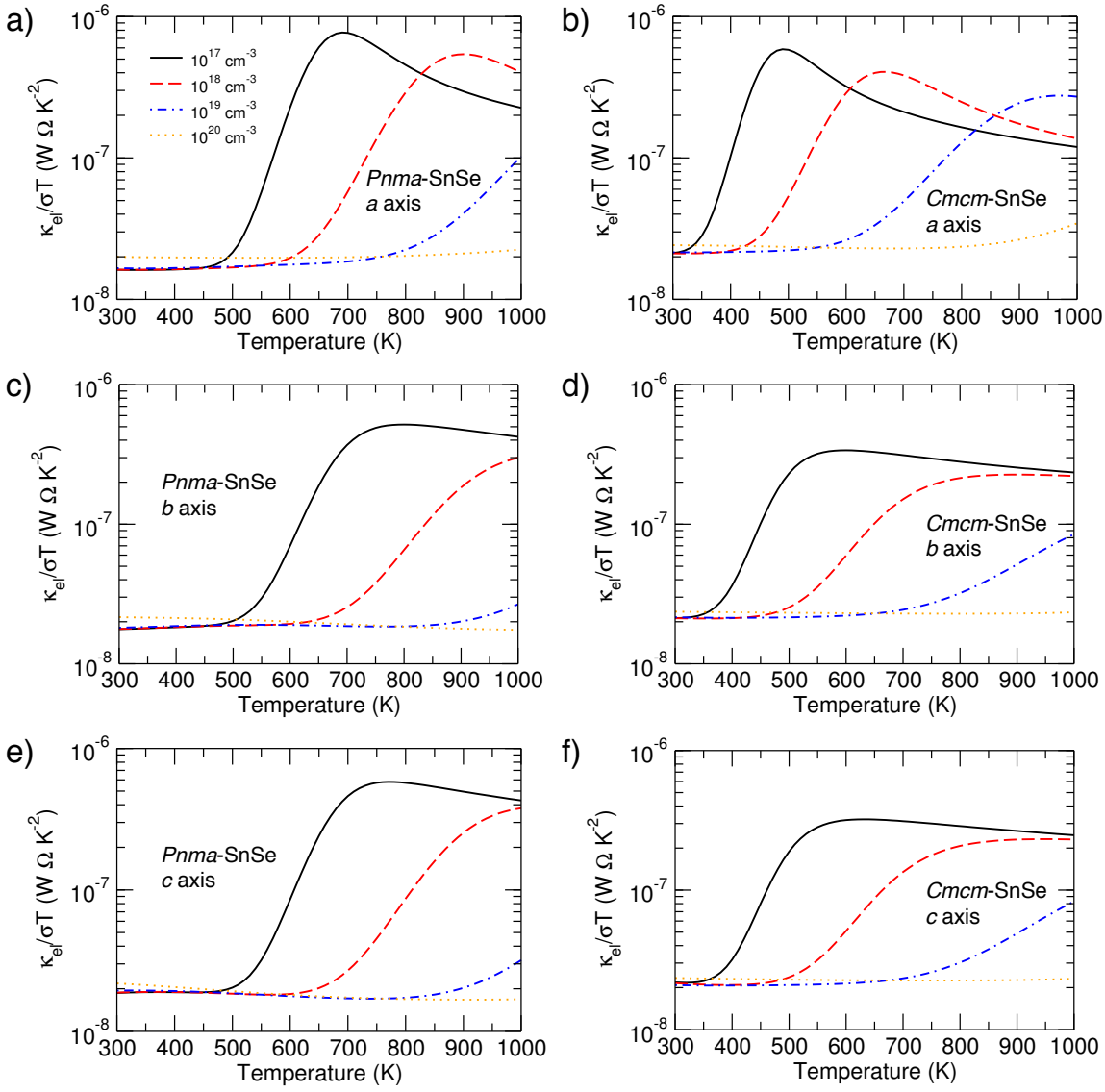

Figure 5.12: The ratio of κ_{el} to σT as a function of temperature and carrier concentration for the low-temperature (*Pnma*) (a, c, e) and high-temperature (*Cmcm*) phases (b, d, f) of SnSe along the *a*, *b*, and *c* axes of the crystal structure. The values for this ratio in the limit of low temperature and low doping concentration, 1.7–2.2$\times 10^{-8}$ W Ω K^{-2}, are typical for the Lorentz number of semiconductors for non-degenerate carriers. As the temperature increases, this ratio is greatly enhanced due to bipolar transport.

Figure 5.12 shows the ratio of the thermal conductivity to the electrical conductivity multiplied by the temperature, $\kappa_{\text{el}}/\sigma T$, as a function of direction, doping concentration, and temperature. The values for this ratio in the limit of low temperature and low doping concentration are 1.7×10^{-8} W Ω K^{-2}, 1.8×10^{-8} W Ω K^{-2}, and 1.9×10^{-8} W Ω K^{-2} for the *Pnma* phase along the *a*, *b*, and *c* axes, respectively, and 2.2×10^{-8} W Ω K^{-2} for the *Cmcm* phase along all three directions. These are typical values for the Lorentz number of semiconductors for non-degenerate carriers. As the temperature increases, bipolar transport increases the electronic thermal conductivity more than the electrical conductivity due to the bipolar diffusion term that is proportional to $\sigma_{\text{e}}\sigma_{\text{h}}/(\sigma_{\text{e}} + \sigma_{\text{h}})$, where σ_{e} and σ_{h} are the contributions to electrical conductivity by electrons and holes, respectively[123] and increases the value of this ratio. This bipolar diffusion becomes significant if electrons and holes have large and similar electrical conductivities. As shown in Fig. 5.12, the $\kappa_{\text{el}}/\sigma T$ ratio increases by as much as a factor of 47 along the a direction of the *Pnma* phase at high temperature for a doping concentration of 10^{17} cm^{-3}. A similar enhancement of the Lorenz number under bipolar transport has also been observed for bismuth telluride.[124] A constant value of (1–2.4)$\times10^{-8}$ W Ω K^{-2} for the Lorenz number is frequently used experimentally to estimate the lattice and electronic contributions to the thermal conductivity.[5] Our findings show that this assumption needs to be reexamined for SnSe if bipolar transport affects the values of the electrical and electronic thermal conductivity at high temperatures.

Figure 5.13 shows the ratio of $S^2\sigma T$ to κ_{el} for *Pnma*-SnSe and *Cmcm*-SnSe as a function of crystal direction, net free-carrier density, and temperature. This quantity is related to the figure of merit ZT according to

$$ZT = \frac{S^2\sigma T}{\kappa_{\text{el}}}\frac{\kappa_{\text{el}}}{\kappa_{\text{el}} + \kappa_{\text{L}}}. \tag{5.1}$$

The quantity $S^2\sigma T/\kappa_{\text{el}}$ is independent of the constant scattering time and is an upper limit to the figure of merit. It approaches ZT if the lattice contribution to the thermal conductivity is negligible compared to the electronic term. For low doping concentration and low temperature, the thermal conductivity is dominated by the lattice term and evaluating ZT requires knowledge of the lattice thermal conductivity and the electron scattering time. However, at high carrier concentration and high temperature the ratio $S^2\sigma T/\kappa_{\text{el}}$ approaches ZT because the lattice thermal conductivity decreases with temperature and takes a remarkably low value at a temperature above 700 K (0.20 W m^{-1} K^{-1})[5], while the electronic thermal conductivity increases with increasing temperature (due to bipolar transport) and increasing doping concentration. Our results for *Cmcm*-SnSe show that for net free-carrier concentration on the order of 10^{17}–10^{18} cm^{-3}, which is in the range of the experimental

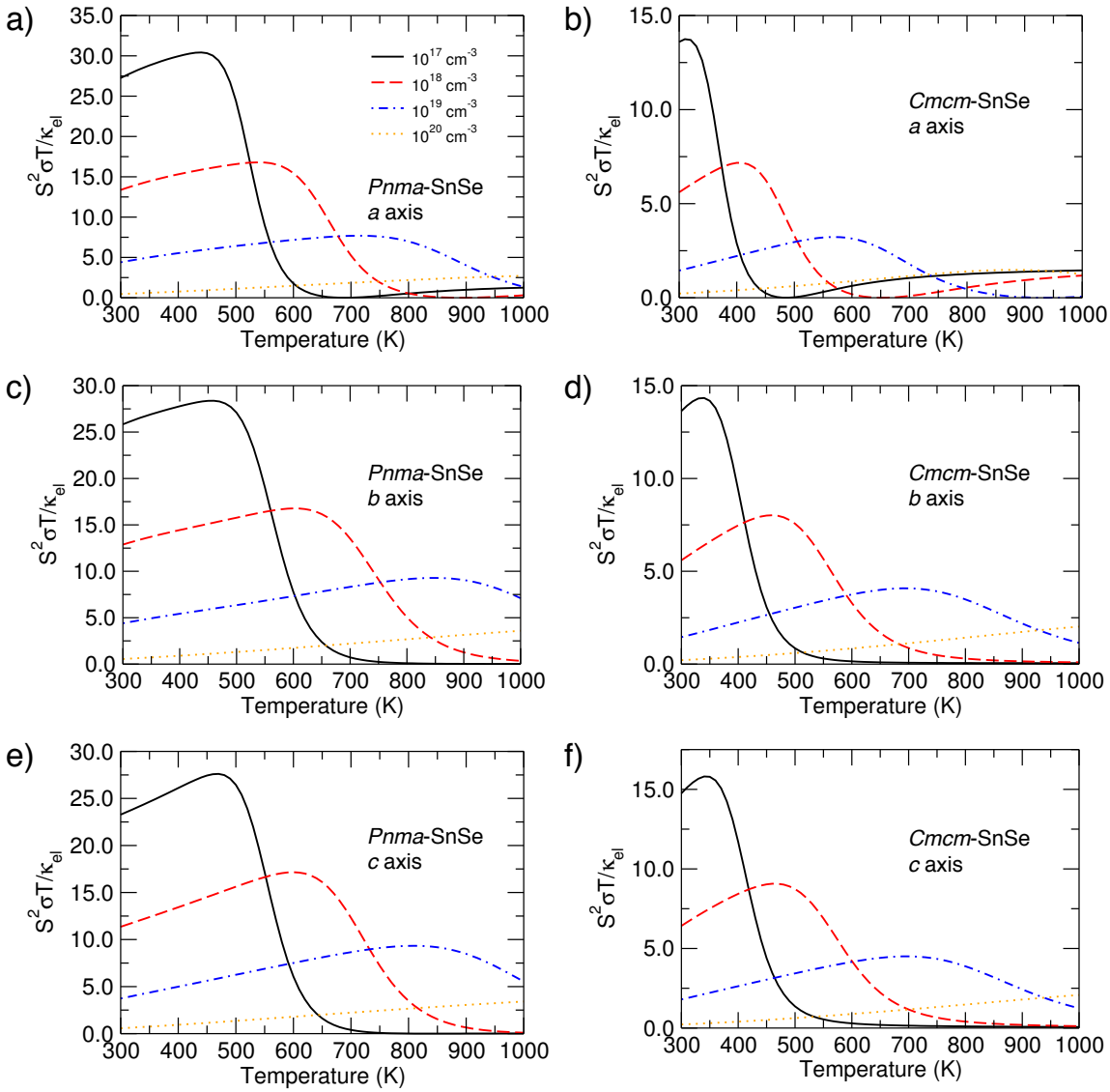

Figure 5.13: $S^2\sigma T/\kappa_{\mathrm{el}}$ as a function of temperature and carrier concentration for the low-temperature (*Pnma*) (a, c, e) and high-temperature (*Cmcm*) phases (b, d, f) of SnSe along the *a*, *b*, and *c* axes of the crystal structure. At high carrier concentration and high temperature, this ratio approaches ZT since the lattice thermal conductivity was found to take a remarkably low value at a temperature above 700 K from experiment.

Hall measurements of Zhao *et al.*,[5] the upper limit to ZT along the b and c axes is much smaller than the remarkably high ZT values (as much as 2.6) reported experimentally. This is an indication that the concentration of dopants in the experimental work of Zhao *et al.*[5] is larger than the Hall coefficients measured at room temperature (6×10^{17} cm^{-3}) as the temperature increases beyond the phase transition. For net free-hole concentrations in the 10^{19}–10^{20} cm^{-3} range and temperatures above 700 K the upper limit to ZT takes values substantially larger than 1 along the b and c axes, both for the *Pnma* and the *Cmcm* phase of SnSe. It is desirable to dope SnSe with acceptors in the range of 10^{19}–10^{20} cm^{-3} to optimize the figure of merit at high temperature.

5.3 Conclusions

We investigated the band structure and electronic transport properties of both the low-temperature *Pnma* and the high-temperature *Cmcm* phase of SnSe. We calculated the band gaps and carrier effective masses and we found that both phases exhibit multiple local band extrema near the band edges that need to be considered when evaluating the thermoelectric properties for this material. We determined the electrical conductivity to be highest along the *b* axis and smallest along the *a* axis for various carrier concentrations. The other transport properties also show a significant degree of anisotropy between the perpendicular direction (*a* axis) and the two in-plane directions (*b* and *c* axes). Bipolar effects strongly affect electronic transport at high temperatures and low carrier concentrations, and cause a sharp decrease and sign reversal of the Seebeck coefficients. The difference between our calculated transport properties and the experimental results in the range of low carrier concentration and high temperature may be attributed to the possible change of the nature or concentration of defects and dopant impurities in the material due to the increasing temperature and the phase transition. Our calculated transport coefficients shed light into recent experimental measurements that reported a remarkably high figure-of-merit value (2.6) for *Cmcm*-SnSe. Our results predict that SnSe would show optimal thermoelectric performance at high temperature when doped in the 10^{19}–10^{20} cm^{-3} range.

Table 5.1: Calculated values of the positions and energies of the conduction and valence band extrema, and effective masses along the *a*, *b*, and *c* axes for the low-temperature (*Pnma*) and high-temperatute (*Cmcm*) phase of SnSe. The positions (k1, k2, k3) are in crystal coordinates. The energies are referenced to the energy of the VBM for each phase.

	Multiplicity	(k1, k2, k3)	E (eV)	m_a^*	m_b^*	m_c^*
Pnma						
VBM	2	(0.00, 0.35, 0.00)	0.000	0.74	0.31	0.16
VBM1	2	(0.00, 0.42, 0.00)	0.000	0.90	0.12	0.15
CBM	2	(0.33, 0.00, 0.00)	0.829	2.40	0.11	0.15
Cmcm						
VBM	2	(0.34, 0.50, 0.00)	0.000	0.34	0.04	0.09
VBM1	2	(0.00, 0.20, 0.39)	-0.031	0.77	0.12	0.05
CBM	2	(0.34, 0.50, 0.00)	0.464	3.07	0.04	0.10
CBM1	2	(0.00, 0.54, 0.08)	0.534	0.06	0.82	1.52

CHAPTER 6

Quasiparticle band structures of Mg_2Si, Mg_2Ge, and Mg_2Sn

We apply density functional and many-body perturbation theory calculations to consistently determine and parameterize the relativistic quasiparticle band structures of Mg_2Si, Mg_2Ge, and Mg_2Sn. The quasiparticle band gaps, including spin-orbit coupling effects, are determined to be 0.728 eV, 0.555 eV and 0.142 eV for Mg_2Si, Mg_2Ge and Mg_2Sn, respectively. The inclusion of the semicore electrons of Mg, Ge, and Sn in the valence is found to be important for the accurate determination of the band gaps of Mg_2Ge and Mg_2Sn. We also developed a Luttinger-Kohn Hamiltonian and determined a set of band parameters to model the near-edge relativistic quasiparticle band structure consistently for all three compounds that can be applied for thermoelectric device simulations. Our calculated values for the Seebeck coefficient of all three compounds are in good agreement with available experimental data for a broad range of temperatures and carrier concentrations. Our results indicate that quasiparticle corrections are necessary for the accurate determination of Seebeck coefficients at high temperatures at which bipolar transport becomes important.

Mg_2X (X = Si, Ge, Sn) compounds are efficient thermoelectric materials composed of relatively inexpensive and Earth-abundant elements, and are thus promising for large-scale thermoelectric energy-conversion applications. Experimental results on these compounds and their alloys indicate favorable thermoelectric properties with large values of the Seebeck coefficient, high electrical conductivity, low thermal conductivity, and values for the dimensionless thermoelectric figure of merit (ZT) that can exceed unity. The figure of merit of unary Bi-doped n-type Mg_2Si reaches values up to 0.86 at 862 K,[7] but it improves drastically in $Mg_2Si_{1-x}Sn_x$ alloys. Values of ZT around 1.1 were measured in n-type $Mg_2Si_{1-x}Sn_x$ solid solutions in the 600-870 K temperature range,[125] and even higher ZT values (1.3) were subsequently reported for alloys with an optimal composition ($Mg_2Si_{0.3}Sn_{0.7}$) near 700 K.[17] The higher ZT values in $Mg_2Si_{1-x}Sn_x$ alloys are attributed both to the reduction of the thermal conductivity due to alloy-disorder scattering,[126] as well as to the convergence of two non-degenerate conduction bands (that are energy reversed in Mg_2Si and Mg_2Sn) for the particular $Mg_2Si_{0.3}Sn_{0.7}$ alloy composition.[17]

In addition to Mg_2Si and Mg_2Sn compounds and alloys, Mg_2X alloys incorporating Mg_2Ge have attracted attention for thermoelectric applications. Binary alloys of Mg_2Ge with Mg_2Sn (n-type $Mg_2Sn_{0.75}Ge_{0.25}$) have been reported to exhibit a $ZT = 1.4$ at 450 °C.[127] In addition, theoretical calculations have predicted that the thermoelectric figure of merit of n-type $Mg_2Ge_{0.5}Sn_{0.5}$ can exceed 2 at 1000 K for a free-electron concentration of 10^{20} cm^{-3}.[128] There is also evidence that the thermoelectric properties of $Mg_2Si_{1-x}Sn_x$ can be further improved by forming ternary alloys with Mg_2Ge. While binary $Mg_2Si_{1-x}Sn_x$ and $Mg_2Ge_{1-x}Sn_x$ alloys have been reported to exhibit miscibility gaps,[129] the immiscible gap is reduced in ternary $Mg_2Si_{1-x-y}Sn_xGe_y$.[130] A figure of merit of $ZT = 1.4$ was reported for Bi-doped n-type $Mg_2Si_{0.55}Sn_{0.4}Ge_{0.05}$ at 800 K,[131] while ZT values greater than 1.45 were found in $Mg_2Si_{0.3}Ge_ySn_{0.7-y}$ ($0 \leqslant y \leqslant 0.05$).[130] The high thermoelectric efficiency of ternary alloys has been attributed to the widening of the band gap of $Mg_2Si_{1-x}Sn_x$ by Ge substitution and the subsequent suppression of bypolar transport at high temperatures,[132] as well as increased conduction band degeneracy and reduced lattice thermal conductivity due to enhanced alloy-disorder scattering of phonons.[130]

The band structure and electronic properties of Mg_2X have also been investigated with atomistic calculations to provide theoretical understanding to the wide body of experimental data. Early results obtained with the empirical pseudopotential method (EPM) underestimate the band gap of Mg_2Si by approximately 0.2 eV but greatly overestimate the gaps of Mg_2Ge and Mg_2Sn.[133] Previous density functional theory (DFT) calculations using the local density approximation (LDA) exchange-correlation functional underestimate the band

gaps of Mg_2X compounds by up to 0.6 eV,[134, 135] due to the systematic underestimation of band gaps by the LDA functional. Moreover, calculations using the Korringa-Kohn-Rostoker (KKR) method and the LDA functional revealed the important role of relativistic corrections including spin-orbit coupling to the valence band structure and thermopower calculations of p-type Mg_2X materials.[136] However, the band-gap values obtained from KKR are also based on LDA and need to be adjusted to experimental values to yield accurate thermoelectric transport coefficients at high temperature.[137] DFT calculations based on the modified Becke-Johnson functional (m-BJ) yield accurate values for the gaps of Mg_2Si (0.58 eV) [138] and Mg_2Sn (0.3 eV)[139], although the reported Mg_2Sn results do not include the effect of spin-orbit coupling on the valence bands.[139] Band gaps calculated with the hybrid Heyd-Scuseria-Ernzerhof (HSE) functional are in good agreement but slighly smaller than experiment,[140] although the reported calculations did not include spin-orbit coupling effects. On the other hand, band structure calculations based on many-body perturbation theory and the all-electron GW method result in accurate gaps for Mg_2Si and Mg_2Ge that are less than 0.1 eV different from experiment.[141] Overall however, accurate band structures that include both quasiparticle and relativistic corrections have not been consistently determined for all three Mg_2Si, Mg_2Ge, and Mg_2Sn compounds.

The electron transport properties of Mg_2X have also been investigated theoretically with the Boltzmann transport equation. Numerous transport studies were based on band structures of compounds and alloys obtained from DFT calculations [139, 137, 136, 138]. However, the computational cost of DFT becomes prohibitive for calculations of structures with more than a few hundred atoms. On the other hand, effective band Hamiltonians (e.g., based on $k \cdot p$ theory or the effective-mass approximation) enable computationally efficient thermoelectric device simulations. Although $k \cdot p$ is the method of choice to simulate semiconductor electronic and optoelectronic devices, the reported transport simulations of Mg_2X materials are based on simple effective-mass models that do not capture the entire complexity of the bands. For example, isotropic and parabolic bands were used for the valence bands[142] and also for both the valence and the conduction bands[143]. However, the non-parabolicity and anisotropy of the bands become important at high doping and high temperature.[136] In particular, experiments have revealed that a single effective mass model is insufficient to fit the Seebeck coefficient data at carrier densities higher than 10^{20} cm^{-3}.[144] More accurate model Hamiltonians (e.g., based on $k \cdot p$ theory[145]) with parameters optimized to reproduce relativistic quasiparticle band structures consistently for all three Mg_2X compounds are therefore necessary for the accurate modeling of electronic transport properties.

In this work, we use first-principles calculations based on density functional and many-

body perturbation theory in the GW approximation to determine and parameterize the relativistic quasiparticle band structures of Mg_2Si, Mg_2Ge, and Mg_2Sn. We evaluate the effect of semicore electrons and spin-orbit coupling on the calculated GW band gaps. Our calculated band gaps, conduction-band energy differences, and spin-orbit splittings are in good agreement with available experimental data. Moreover, we fit the GW band structures of all three compounds with an effective Hamiltonian based on $k \cdot p$ theory to obtain a consistent parameterization of the near-edge band structures of all three compounds that includes quasiparticle and relativistic corrections. Our band structures accurately reproduce the available measured Seebeck coefficients for all three compounds, while our derived band parameterizations can be applied for the accurate and efficient modeling of electronic transport in Mg_2X thermoelectric materials and devices.

This manuscript is organized as follows. In Section 6.1 we discuss our computational methodology for the determination of the quasiparticle band structure of Mg_2X compounds. In Section 6.2 we present and discuss our calculated results. In Subsection 6.2.1 we discuss the features of the band structures of Mg_2X, we assess the importance of the various approximations involved in the calculations, and we compare to experimental results. In Subsection 6.2.2 we parameterize the quasiparticle band structure with a $k \cdot p$ model Hamiltonian that can be subsequently applied for large-scale device simulations. Last, in Subsection 6.2.3 we determine the Seebeck coefficients of Mg_2X as a function of carrier density and temperature, and we compare to available experimental data to validate the accuracy of our calculated band structures in predicting thermoelectric transport properties.

6.1 Methodology

We studied the electronic band structure and thermoelectric properties of Mg_2X compounds using first-principles calculations based on denisty functional theory (DFT) and many-body perturbation theory. We performed DFT calculations to obtain the ground-state charge density and electronic wave functions within the generalized gradient approximation with the Perdew-Burke-Ernzerhof (PBE) parameterization for the exchange-correlation potential.[91] We used the plane-wave pseudopotential method[63] as implemented in the Quantum-ESPRESSO code[40]. We employed norm-conserving pseudopotentials generated with the Atomic code and a plane-wave cutoff of 350 Ry, 500 Ry and 350 Ry for Mg_2Si, Mg_2Ge and Mg_2Sn, respectively[64]. We also examined the effect of semicore electons on the band structure by treating both the outermost-shell electrons (e.g., $5s$ and $5p$ for Sn) and those from the next complete atomic shell (i.e., the $4s$, $4p$, and $4d$ electrons

Table 6.1: Atomic parameters used to generate valence and semicore pseudopotentials: the orbitals treated as part of the valence and their electronic configuration, the cutoff radii for the s, p, and d pseudopotential components (r_s, r_p, and r_d, respectively), and the choice of the local component.

	Element	Valence orbitals	r_s	r_p	r_d	Local
Valence	Mg	$3s^2 3p^0 3d^0$	2.14	2.54	2.54	s
	Si	$3s^2 3p^2 3d^0$	1.75	1.93	1.50	d
	Ge	$4s^2 4p^{1.75} 4d^{0.25}$	1.98	2.18	2.46	d
	Sn	$5s^2 5p^{1.75} 5d^{0.25}$	2.33	2.39	2.69	s
Semicore	Mg	$2s^2 2p^6 3d^0$	0.60	0.60	0.60	s
	Ge	$3s^2 3p^6 3d^{10}$	0.60	0.60	0.60	s
	Sn	$4s^2 4p^6 4d^{10}$	0.80	0.80	0.80	p

of Sn) as valence electrons. A summary of the atomic parameters used for the generation of the pseudopotentials is presented in Table 6.1. Our subsequent GW results show that the semicore states of Mg, Ge, and Sn need to be included in the valence in order to obtain accurate values for the calculated band gaps of Mg_2Ge and Mg_2Sn. All calculations were performed for the experimentally measured values for the lattice parameters: 6.338 $\mathring{A}$, 6.393 $\mathring{A}$, and 6.760 $\mathring{A}$ for Mg_2Si, Mg_2Ge and Mg_2Sn, respectively[146]. The Brillouin zone was sampled using a 6×6×6 Monkhorst-Pack grid[118]. We calculated the quasiparticle band structure of Mg_2X compounds using the one-shot GW method[65] and the BerkeleyGW code[1]. The dielectric function was calculated at zero frequency and extended to finite frequency using the generalized plasmon-pole model of Hybertsen and Louie[65]. The Coulomb-hole self-energy term was calculated using the static-remainder approach[66]. The dielectric matrix cutoff and the number of bands used for the Coulomb-hole summation are shown in Table 6.2. These parameters were increased until a convergence of 10 meV in the resulting quasiparticle band gaps was achieved. Corrections due to spin-orbit coupling (SO) interaction[93] were calculated in a non-self-consistent way using plane waves up to a cut-off energy of 100 Ry. We used the maximally localized Wannier function formalism[95, 96] to interpolate the quasiparticle energies and spin-orbit coupling matrix elements to a fine mesh (120×120×120) in the first Brillouin zone, and then determined the Seebeck coefficients with the Boltzmann transport equation in the constant-relaxation-time approximation.[120, 121] This methodology has previously been applied to investigate the electronic and transport properties of SnSe[85], $Pb_7Bi_4Se_{13}$[97], and TiO_2[147].

Table 6.2: Values for the GW calculation parameters [wave-function plane-wave cutoff energy (psi cutoff), dielectric-matrix plane-wave cutoff energy (ε cutoff), and number of bands used in the Coulomb-hole self-energy term) used to converge the quasiparticle band gaps to within 10 meV for calculations employing the valence pseudopotential for Si and the semicore pseudopotentials for Mg, Ge, and Sn from Table 6.1.

Material	ψ cutoff (Ry)	ε cutoff (Ry)	# bands in CH sum
Mg_2Si	350	30	900
Mg_2Ge	500	30	1000
Mg_2Sn	350	30	1000

6.2 Results and discussion

6.2.1 Quasiparticle band structure

Our results for the band gaps of the Mg_2X compounds calculated using PBE and GW are summarized in Table 6.3 and compared to previous experimental and theoretical results. The band gaps (including the effects of spin-orbit coupling) are found to be 0.728 eV, 0.555 eV and 0.142 eV for Mg_2Si, Mg_2Ge and Mg_2Sn, respectively. The valence-band maximum is located at the Γ point and the conduction-band maximum lies at the X point for all materials. For Mg_2Sn, the underestimation of the band gap by PBE results in an indirect overlap of the valence and conduction bands, predicting an incorrect semimetallic nature for this material. The incorrect band occupations for Mg_2Sn were fixed by first shifting the conduction bands by 0.148 eV higher in energy. The value of the shift was chosen in a self-consistent way, such that the corrected PBE band gap is equal to the quasiparticle gap after GW corrections. A range of experimental band-gap values has been reported by various investigators for each Mg_2X compound[148, 149, 150, 151, 152, 153, 154, 155, 156, 157]. Typically, the shape of the absorption edge suggests a smaller gap while the temperature dependence of conductivity predicts a larger one. Our calculated band-gap values of Mg_2Ge and Mg_2Sn are found to be in much better agreement with those determined from absorption measurements.

We also examined the effect of spin-orbit coupling on the band gaps and valence-band splittings of Mg_2X. Mg_2Sn has the strongest spin-orbit coupling effect of the three Mg_2X compounds due to its large atomic number. The calculated spin-orbit splittings of the top valence band at the Γ point are in good agreement with the experimental data from electroreflectance measurements (Table 6.4)[152, 158].

The calculated band structures of Mg_2Si, Mg_2Ge and Mg_2Sn, including quasiparticle and spin-orbit coupling corrections, are shown in Figure 6.1. The lowest two conduction bands exhibit local minima at the X point of the Brillouin zone for all three compounds.

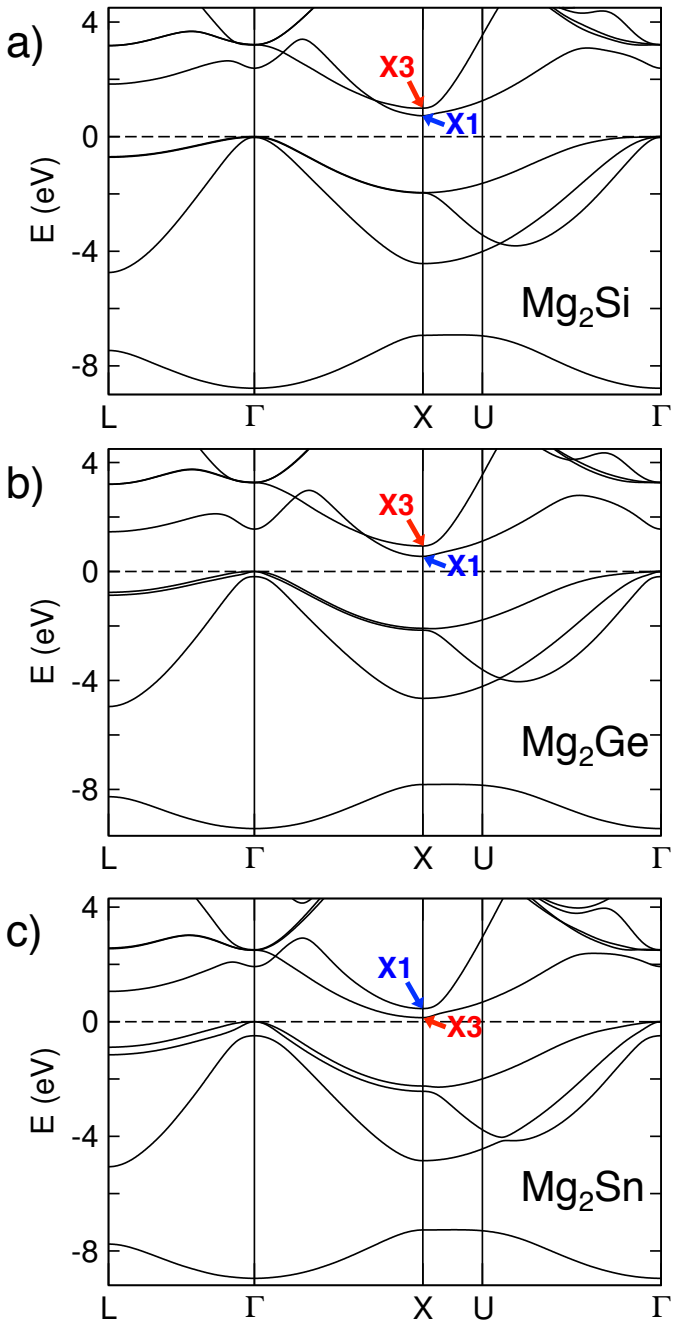

Figure 6.1: Quasiparticle band structures of Mg_2Si, Mg_2Ge, and Mg_2Sn with spin-orbit coupling effects included, using semicore pseudopotentials for Mg, Ge, and Sn. The X1 and X3 states at the X point are indicated with blue and red arrows, correspondingly.

Table 6.3: The quasiparticle band gap (in eV) calculated in the present work and measured by experiment. Here we used valence pseudopotentials for Si, and semicore pseudopotentials for Mg, Ge, and Sn. Our calculated values are compared to previous theoretical work, as well as experimental measurements using optical absorption or the temperature dependence of the electrical conductivity.

	Mg_2Si	Mg_2Ge	Mg_2Sn
This work, PBE	0.204	0.144	-0.138
This work, GW	0.739	0.619	0.309
This work, GW+L·S	0.728	0.555	0.142
Theory, EPM[133]	0.53	0.92	0.64
Theory, LDA[135]	0.118	0.166	0.026
Theory, m-BJ[138]	0.58	–	–
Theory, TB-mBJ[139]	0.6	–	0.3
Theory, HSE[140]	0.49	–	0.13
Theory, GW[141]	0.65	0.50	–
Experiment	0.62-0.77[148, 149, 150, 151, 157]	0.54-0.74[148, 150, 151, 152, 153, 157]	0.14-0.30[148, 151, 154, 155, 156]

Table 6.4: Spin-orbit splitting (in eV) of the top valence band of Mg_2X at Γ.

	Mg_2Si	Mg_2Ge	Mg_2Sn
This work, GW+L·S	0.032	0.190	0.492
Theory, KKR/LDA[136]	0.036	0.208	0.525
Experiment[158]	0.03	0.20	0.48

The two minima lie close in energy (the lower-energy one forming the global conduction band minimum) and correspond to states of different symmetry, either of the X1 type, formed by s orbitals of Si, Ge, or Sn, or of the X3 type, formed by s orbitals of Mg. For both Mg_2Si and Mg_2Ge the conduction-band minimum is the X1 state, but the order of the two bands is inverted for Mg_2Sn. The order of the two lowest conduction bands at the X point does not change upon the inclusion of quasiparticle correction and spin-orbit effects. This conduction-band reordering has also been highlighted in previous band-structure calculations of binary Mg_2X[133], and the large values of the Seebeck coefficient in alloys has been attributed to the convergece in energy of these two minima[17]. Our calculated values for the transition energy from state X1 to X3 is summarized in Table 6.5 for all three materials.

To further explore the effect of semicore electrons on the GW-calculated electronic structures, we also evaluated the band gaps of all three materials using pseudopotentials

Table 6.5: Energy difference between the two lowest conduction bands X1 and X3 ($E_{\mathrm{X3}} - E_{\mathrm{X1}}$, cf. Fig. 6.1) of Mg_2Si, Mg_2Ge, and Mg_2Sn, calculated using the semicore pseudopotentials for Mg, Ge, and Sn.

	Mg_2Si	Mg_2Ge	Mg_2Sn
This work, PBE	0.214	0.388	-0.305
This work, GW	0.265	0.381	-0.317

Table 6.6: Band-gap values (in eV) calculated with semicore electrons frozen in the core ("valence" pseudopotentials) or included in the valence ("semicore" pseudopotentials). Spin-orbit interaction effects are included. Only the valence electrons are used for the generation of the GPP model parameters.

Pseudopotentials	Mg_2Si	Mg_2Ge	Mg_2Sn
Semicore Mg + semicore X	/	0.555	0.142
Valence Mg + semicore X	/	0.521	0.010
Semicore Mg + valence X	0.728	0.414	-0.016
Valence Mg + valence X	0.710	0.391	-0.140

with all the semicore electrons frozen in the core. The band-gap values calculated with different combinations of valence and semicore pseudopotentials are summarized in Table 6.6. The inclusion of semicore orbitals in the pseudopotential of Ge and Sn is found to be necessary to determine accurate band gaps for Mg_2Ge and Mg_2Sn. The gaps are underestimated by at least 100 meV if the semicore s, p, and d electrons are treated as part of the frozen pseudopotential core instead of valence electrons. In comparison, the inclusion of semicore orbitals of Mg have a strong effect on the band gap of Mg_2Sn, but they do not play an important role in the band gaps of Mg_2Si and Mg_2Ge. To understand the origin of the important role of semicore Mg orbitals for the band gap of Mg_2Sn we project the conduction and valence band wave functions onto the semicore states. We find that Mg semicore states only contribute to the second lowest conduction state of Mg_2Si and Mg_2Ge at the X point (X3) but little to the lowest state (X1). Similarly, Mg semicore states contribute to the lowest conduction band of Mg_2Sn (X3) but not to the next-higher conduction band (X1). The different effect of the inclusion of semicore Mg orbitals on the GW band gap of the three materials is therefore a consequence the different contributions of these semicore states to the orbital characters of their bottom conduction bands.

We also examined the role of semicore electrons on the construction of the generalized plasmon-pole (GPP) model used in GW calculations. The valence charge density is needed as an input to the sum rules used to generate the parameters for the GPP model. For our GW calculations for all the Mg_2X systems, we examined three different choices for the charged density input to the GPP model: (i) using the outermost s and p electrons only ("valence"), (ii) using the outermost valence electrons plus the semicore d shell of the cations ("semicore d + valence"), and (iii) the outermost valence electrons plus the entire semicore shell for both Mg and for the cations ("semicore s, p, d + valence"). The results of the comparison of the three charge-density models for the band gap of Mg_2X are summarized in Table 6.7. The inclusion of Mg semicore orbitals in the plasmon-pole model has a minor effect of the band gap, as evidenced by the slight reduction of the band gap

Table 6.7: Calculated values of the band gap (in eV) of Mg_2X as a function of the number of electrons included in the construction of the generalized plasmon-pole model. Spin-orbit interaction effects are included. The calculations used valence pseudopotentials for Si, and semicore pseudopotentials for Mg, Ge, and Sn.

Electrons in charge density	Mg_2Si	Mg_2Ge	Mg_2Sn
Semicore s, p, d + valence	0.691	0.752	0.235
Semicore d + valence	/	0.740	0.271
Valence only	0.728	0.555	0.142

of Mg_2Si by only 37 meV. However, the inclusion of the semicore d electrons has a larger effect on the gap of Mg_2Ge and Mg_2Sn, increasing the gap by as much as 0.185 eV for the case Mg_2Ge. Inner semicore orbitals have a minor effect also in the case of Mg_2Ge and Mg_2Sn, e.g., decreasing the gap of Mg_2Sn by only 36 meV. We argue that including only the valence orbitals in the GPP model construction yields more realistic values for the gap than the inclusion of either the semicore d electrons or the entire semicore shell. Since the semicore electrons are strongly bound to their atoms, they do not screen the electric field as efficiently as valence electrons and should not be considered as part of the valence for the GPP sum rules[159, 160]. The dielectric functions calculated from the plasmon-pole model only using the valence electrons are found to have much better agreement with those determined from a full-frequency calculation in the present work (Table 6.7).

6.2.2 Band-structure parameterization with $k \cdot p$

To enable the accurate and consistent modeling of Mg_2X electronic and thermoelectric devices, we developed a parameterized Hamiltonian model based on $k \cdot p$ theory that can be employed for large-scale device simulations. The GW method provides accurate results and atomistic understanding for the band structures of materials, but its high computational cost prohibits its application for the large and complex structures needed for device simulations. To enable multi-scale device simulations we adopt and parameterize an effective-mass Hamiltonian derived from a generalized Luttinger-Kohn (LK) model[145] using the $k \cdot p$ method. The 6×6 Hamiltonian matrix describing the top three valence bands (doubly

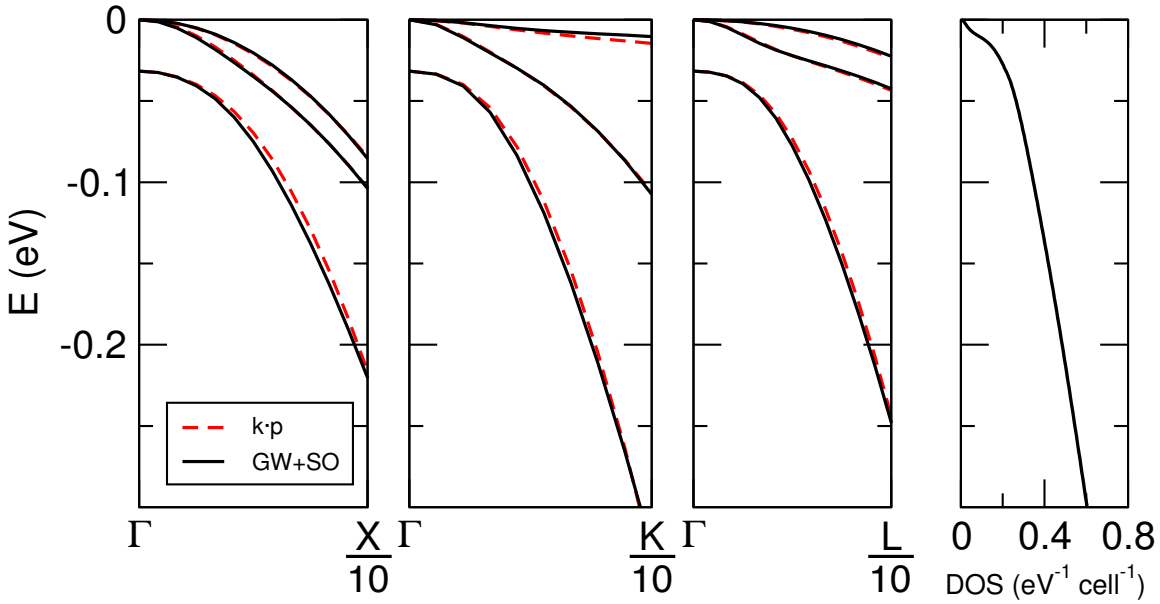

Figure 6.2: The top three valence bands of Mg_2Si along the Γ-X, Γ-K, and Γ-L directions as calculated with GW (including spin-orbit coupling effects, solid line) and parameterized with a $k \cdot p$ Hamiltonian (dashed line).

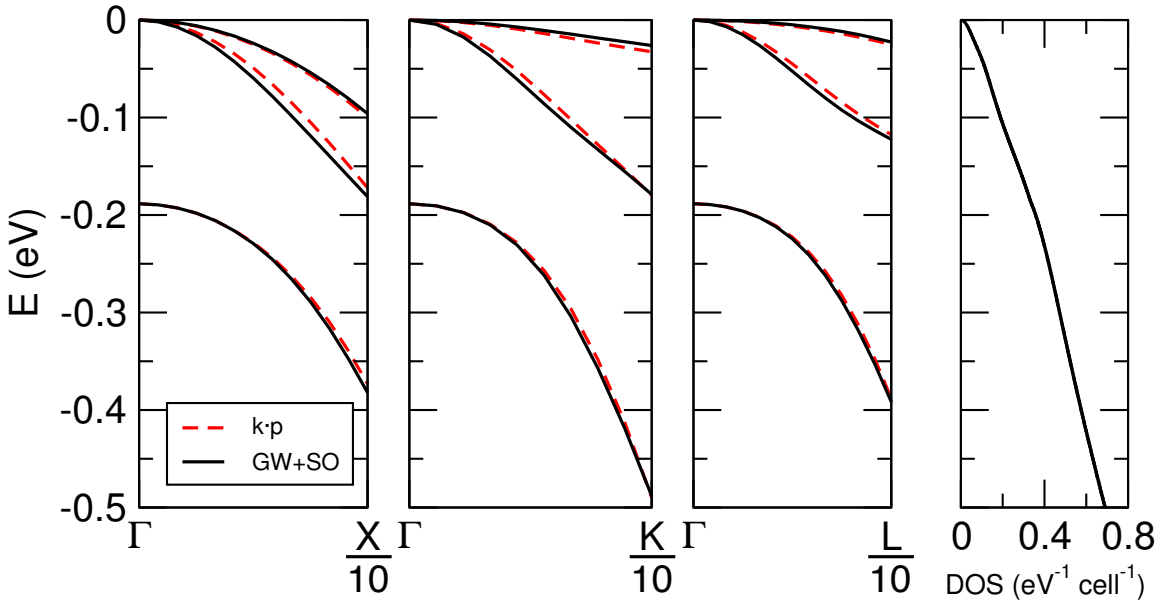

Figure 6.3: The top three valence bands of Mg_2Ge along the Γ-X, Γ-K, and Γ-L directions as calculated with GW (including spin-orbit coupling effects, solid line) and parameterized with a $k \cdot p$ Hamiltonian (dashed line).

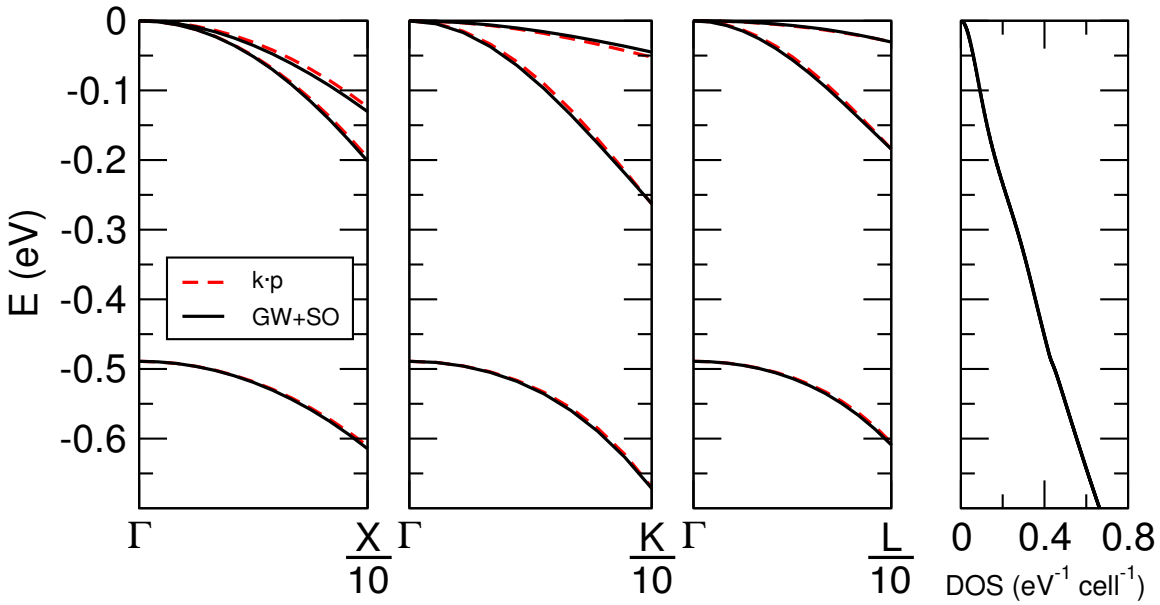

Figure 6.4: The top three valence bands of Mg_2Sn along the Γ-X, Γ-K, and Γ-L directions as calculated with GW (including spin-orbit coupling effects, solid line) and parameterized with a $k \cdot p$ Hamiltonian (dashed line).

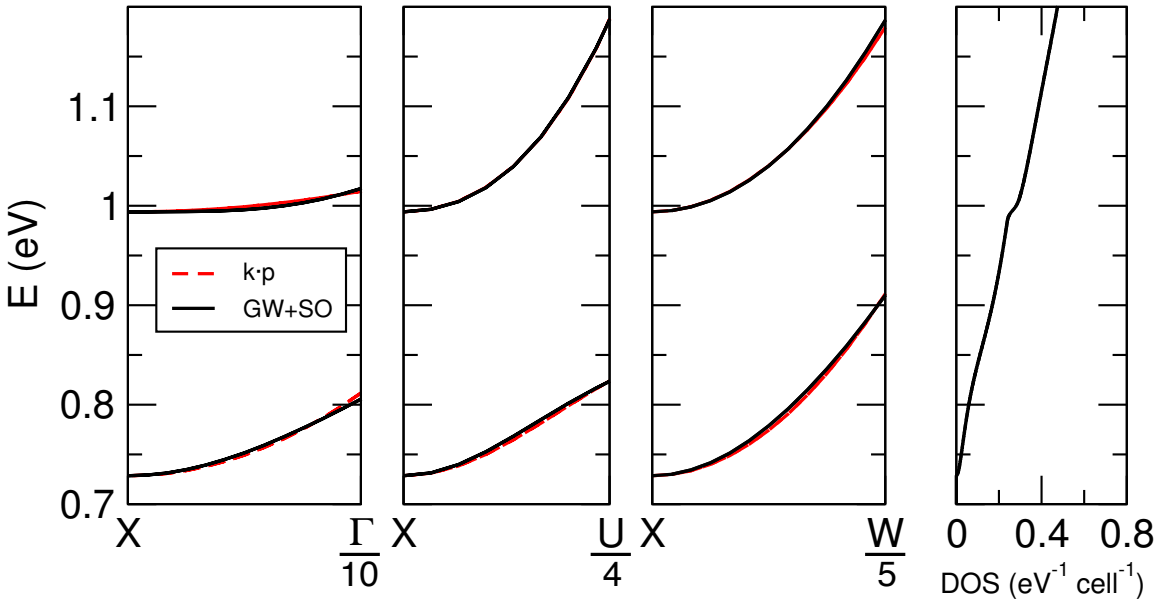

Figure 6.5: The two lowest conduction bands of Mg_2Si along the X-Γ, X-U, and X-W direction as calculated with GW (including spin-orbit coupling effects, solid line) and parameterized with a $k \cdot p$ Hamiltonian (dashed line).

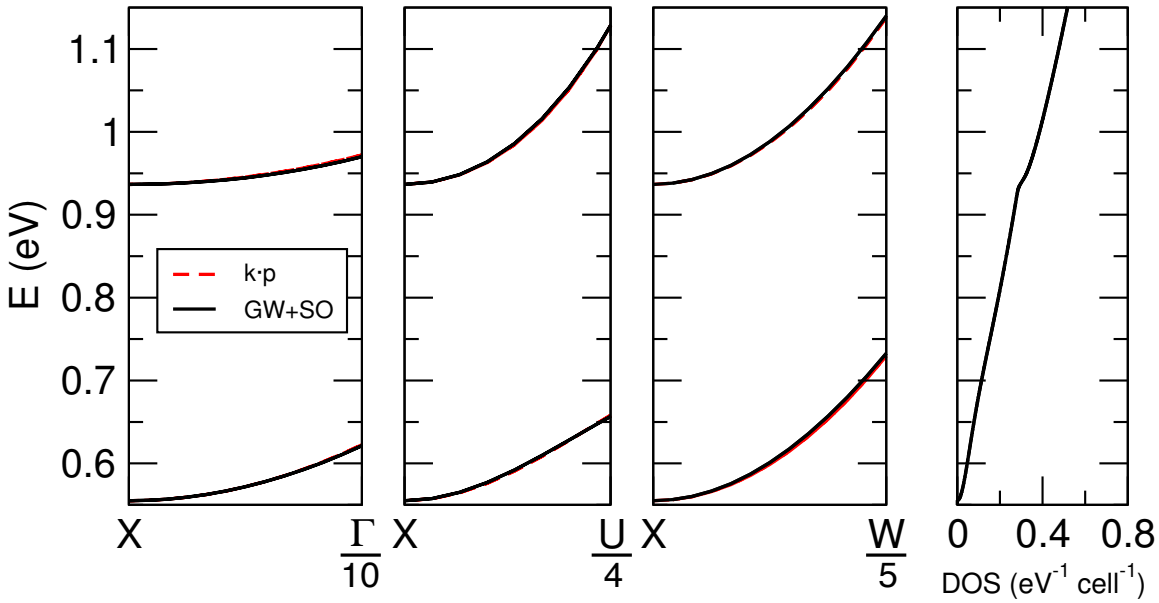

Figure 6.6: The two lowest conduction bands of Mg_2Ge along the X-Γ, X-U, and X-W direction as calculated with GW (including spin-orbit coupling effects, solid line) and parameterized with a $k \cdot p$ Hamiltonian (dashed line).

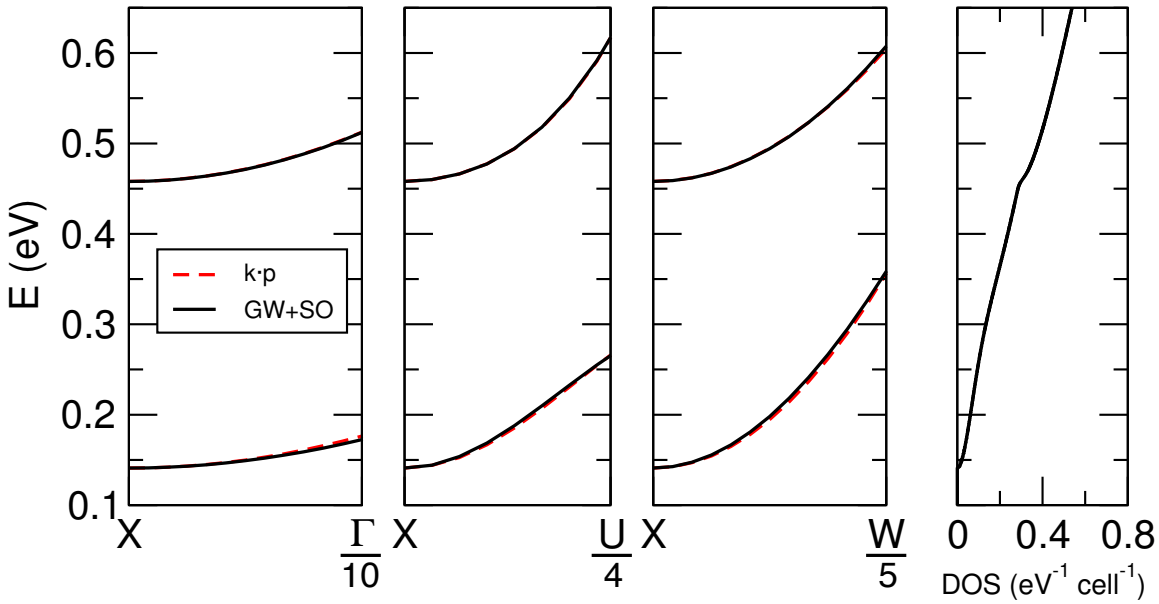

Figure 6.7: The two lowest conduction bands of Mg_2Sn along the X-Γ, X-U, and X-W direction as calculated with GW (including spin-orbit coupling effects, solid line) and parameterized with a $k \cdot p$ Hamiltonian (dashed line).

Table 6.8: Values of the $k \cdot p$ model parameters, band-structure effective masses for the heavy-hole (HH), light-hole (LH), and spin-orbit split-off (SO) valence bands along Γ-X, Γ-K, and Γ-L, and valence DOS effective masses for Mg_2Si, Mg_2Ge, and Mg_2Sn.

	Mg_2Si	Mg_2Ge	Mg_2Sn
$k \cdot p$ parameters			
γ_1	3.317	4.137	4.946
γ_2	0.532	0.710	0.596
γ_3	1.239	1.612	1.861
γ_1'	3.317	4.137	3.518
γ_2'	0.532	0.710	0.519
γ_3'	1.239	1.612	1.550
Heavy-hole band			
$m_{HH}^{\Gamma-X}$	0.444	0.368	0.266
$m_{HH}^{\Gamma-K}$	0.904	0.796	0.600
$m_{HH}^{\Gamma-L}$	1.192	1.095	0.817
Light-hole band			
$m_{LH}^{\Gamma-X}$	0.228	0.180	0.163
$m_{LH}^{\Gamma-K}$	0.181	0.142	0.122
$m_{LH}^{\Gamma-L}$	0.173	0.136	0.115
Split-off band			
$m_{SO}^{\Gamma-X}$	0.301	0.242	0.284
$m_{SO}^{\Gamma-K}$	0.301	0.242	0.284
$m_{SO}^{\Gamma-L}$	0.301	0.242	0.284
DOS effective mass			
m_{DOS}^{*}	0.914	0.863	0.595
α (eV^{-1})	119.458	23.469	4.091

Table 6.9: Values for the $k \cdot p$ model parameters, band-structure effective masses for the two lowest conduction bands along X-Γ, X-U, and X-W, and conduction DOS effective masses for Mg_2Si, Mg_2Ge, and Mg_2Sn.

	Mg_2Si	Mg_2Ge	Mg_2Sn
$k \cdot p$ parameters			
γ_4	2.221	1.834	1.078
γ_5	4.887	4.742	6.541
γ_6	0.555	0.961	1.658
γ_7	4.957	5.465	4.459
γ_8	8.350	8.361	8.926
Lowest conduction band			
$m_{CBM1}^{X-\Gamma}$	0.450	0.545	0.928
m_{CBM1}^{X-U}	0.205	0.211	0.153
m_{CBM1}^{X-W}	0.205	0.211	0.153
2nd lowest conduction band			
$m_{CBM2}^{X-\Gamma}$	1.802	1.041	0.603
m_{CBM2}^{X-U}	0.202	0.183	0.224
m_{CBM2}^{X-W}	0.202	0.183	0.224
DOS effective mass			
m^*_{DOS}	0.462	0.576	0.556
α (eV^{-1})	17.485	6.479	5.877

spin degenerate due to inversion symmetry) near the Γ point is given by:

$$\begin{pmatrix} H_{hh} & b & c & 0 & ib'/\sqrt{2} & -i\sqrt{2}c' \\ b^* & H_{lh} & 0 & c & -iq & i\sqrt{3}b'/\sqrt{2} \\ c^* & 0 & H_{lh} & -b & -i\sqrt{3}b'^*/\sqrt{2} & -iq \\ 0 & c^* & -b^* & H_{hh} & -i\sqrt{2}c'^* & -ib'^*/\sqrt{2} \\ -ib'^*/\sqrt{2} & iq & i\sqrt{3}b'/\sqrt{2} & i\sqrt{2}c' & H_{so} & 0 \\ i\sqrt{2}c'^* & -i\sqrt{3}b'^*/\sqrt{2} & iq & ib'/\sqrt{2} & 0 & H_{so} \end{pmatrix}, \quad (6.1)$$

where the matrix elements are given by

$$H_{hh} = \frac{\hbar^2}{2m_0}[(\gamma_1 + \gamma_2)(k_x^2 + k_y^2) + (\gamma_1 - 2\gamma_2)k_z^2], \quad (6.2)$$

$$H_{lh} = \frac{\hbar^2}{2m_0}[(\gamma_1 - \gamma_2)(k_x^2 + k_y^2) + (\gamma_1 + 2\gamma_2)k_z^2], \quad (6.3)$$

$$H_{so} = \frac{\hbar^2}{2m_0}[\gamma_1'(k_x^2 + k_y^2 + k_z^2)] + \Delta_0, \quad (6.4)$$

$$b = \frac{-\sqrt{3}i\hbar^2}{m_0}\gamma_3(k_x - ik_y)k_z, \tag{6.5}$$

$$b' = \frac{-\sqrt{3}i\hbar^2}{m_0}\gamma_3'(k_x - ik_y)k_z, \tag{6.6}$$

$$c = \frac{\sqrt{3}\hbar^2}{2m_0}[\gamma_2(k_x^2 - k_y^2) - 2i\gamma_3 k_x k_y], \tag{6.7}$$

$$c' = \frac{\sqrt{3}\hbar^2}{2m_0}[\gamma_2'(k_x^2 - k_y^2) - 2i\gamma_3' k_x k_y], \tag{6.8}$$

and

$$q = \frac{\sqrt{2}\hbar^2}{2m_0}[\gamma_2'(k_x^2 + k_y^2) - 2\gamma_2' k_z^2]. \tag{6.9}$$

The eigenvalues of this 6×6 generalized LK Hamiltonian are functions of the wave-vector k and represent the three two-fold spin-degenerate bands: the heavy-hole (HH), light-hole (LH), and spin-orbit split-off (SO) bands. To determine the Luttinger parameters γ_1, γ_2, γ_3, γ_1', γ_2', and γ_3', we fit the matrix eigenvalues to the calculated quasiparticle band energies near the Γ point. The effective masses of the three bands are then related to the Luttinger parameters along the $\Gamma - X$, $\Gamma - K$, and $\Gamma - L$ directions by

$$m_{HH}^{\Gamma-X} = \frac{1}{\gamma_1 - 2\gamma_2}, \tag{6.10}$$

$$m_{LH}^{\Gamma-X} = \frac{1}{\gamma_1 + 2\gamma_2}, \tag{6.11}$$

$$m_{SO}^{\Gamma-X} = \frac{1}{\gamma_1'}, \tag{6.12}$$

$$m_{HH}^{\Gamma-K} = \frac{1}{\gamma_1 - \sqrt{\gamma_2^2 + 3\gamma_3^2}}, \tag{6.13}$$

$$m_{LH}^{\Gamma-K} = \frac{1}{\gamma_1 + \sqrt{\gamma_2^2 + 3\gamma_3^2}}, \tag{6.14}$$

$$m_{SO}^{\Gamma-K} = \frac{1}{\gamma_1'}, \tag{6.15}$$

$$m_{HH}^{\Gamma-L} = \frac{1}{\gamma_1 - 2\gamma_3}, \tag{6.16}$$

$$m_{LH}^{\Gamma-L} = \frac{1}{\gamma_1 + 2\gamma_3}, \tag{6.17}$$

$$\tag{6.18}$$

and

$$m_{SO}^{\Gamma-L} = \frac{1}{\gamma_1'}. \tag{6.19}$$

For Mg_2Si and Mg_2Ge, we apply the constraint that $\gamma_1 = \gamma_1'$, $\gamma_2 = \gamma_2'$, and $\gamma_3 = \gamma_3'$ so that the Hamiltonian reduces to the original LK Hamiltonian without affecting the accuracy of the fit. The newly introduced parameters γ_1', γ_2', and γ_3' are, however, found to be necessary for Mg_2Sn to obtain reasonably good agreement between the band energies calculated from first principles and with the $k \cdot p$ method. Figures 6.2, 6.3, and 6.4 show the band structures of Mg_2Si, Mg_2Ge, and Mg_2Sn in the vicinity of the Γ point as determined by the 6×6 $k \cdot p$ Hamiltonian and compared to the original GW band structure. The Luttinger parameters and the effective-mass values are listed in Table 6.8. The heavy-hole and light-hole bands are found to be anisotropic, and the effective mass of the heavy-hole band is largest along the Γ-L direction. On the other hand, the effective mass of split-off band does not show any dependence on the direction of wave vectors.

Since the fundamental band gaps are indirect in Mg_2Si, Mg_2Ge, and Mg_2Sn, we ignore the interaction between the valence and conduction bands and analyze the two lowest conduction bands separately from the valence bands using a 2×2 $k \cdot p$ Hamiltonian,

$$\begin{pmatrix} H_1 & q \\ q & H_2 \end{pmatrix}, \tag{6.20}$$

where the Hamiltonian matrix elements are given by

$$H_1 = \frac{\hbar^2}{2m_0}[\gamma_4 k_x^2 + \gamma_5(k_y^2 + k_z^2)], \tag{6.21}$$

$$H_2 = \frac{\hbar^2}{2m_0}[\gamma_6 k_x^2 + \gamma_7(k_y^2 + k_z^2)] + \Delta_{12}, \tag{6.22}$$

$$q = \frac{\hbar^2}{2m_0}\gamma_8 k_y k_z, \tag{6.23}$$

$$m_{CBM1}^{X-\Gamma} = \frac{1}{\gamma_4}, m_{CBM2}^{X-\Gamma} = \frac{1}{\gamma_6}, \tag{6.24}$$

$$m_{CBM1}^{X-U} = \frac{1}{\gamma_5}, m_{CBM2}^{X-U} = \frac{1}{\gamma_7}, \tag{6.25}$$

and

$$m_{CBM1}^{X-W} = \frac{1}{\gamma_5}, m_{CBM2}^{X-W} = \frac{1}{\gamma_7}. \tag{6.26}$$

Figures 6.5, 6.6, and 6.7 show the conduction band structures of Mg_2Si, Mg_2Ge, and Mg_2Sn in the vicinity of the X point as determined by the 2×2 $k \cdot p$ Hamiltonian. The $k \cdot p$ parameters and the effective-mass values are listed in Table 6.9. The longitudinal effective masses were determined along the X-Γ direction, and the transverse effective masses were

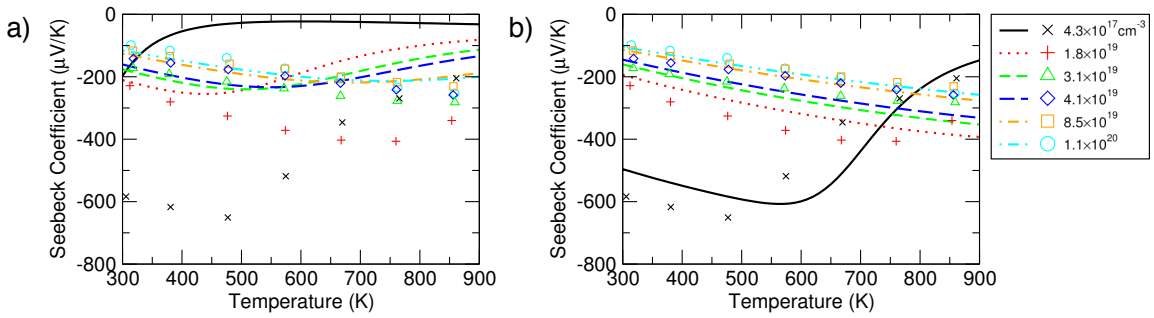

Figure 6.8: Experimental[7] (points) and calculated (lines) values for the temperature and carrier-density dependence of the Seebeck coefficient of n-type Mg_2Si. The calculations are based on (a) PBE and (b) GW band structures and include spin-orbit coupling effects. The results obtained with the GW band structure are in better agreement with experiment than those from PBE data.

determined to be the same along the X-U and X-W directions. The longitudinal effective mass was found to be larger in the second lowest conduction band than in the lowest one for Mg_2Si and Mg_2Ge, but larger in the lowest conduction band than in the second lowest one for Mg_2Sn, which is consistent with the energy reordering of the X1 and X3 states we observed in the band structure (FIG. 6.1).

We also calculated the density-of-states (DOS) effective mass, m^*_{DOS}, which is independent of the direction of wave-vectors, by fitting the DOS near the band extrema with the hyperbolic-band equation,

$$\text{DOS}(E) = \frac{V_{\text{cell}}}{2\pi^2}(2m^*_{\text{DOS}})^{\frac{3}{2}}E^{\frac{1}{2}}(1+\alpha E)^{\frac{1}{2}}, \tag{6.27}$$

where V_{cell} is the volume of the unit cell and α is a parameter with units of inverse energy to enable the fitting of the bands with a hyperbola. We derived the DOS effective masses by fitting the hyperbolic equation to the first hyperbolic region near the valence-band maximum and conduction-band minimum. The fitted DOS effective masses m^*_{DOS} and the hyperbola parameters α are listed in Table 6.8 and 6.9. The curvature of the DOS curves changes near the top of the split-off band (FIG. 6.2, 6.3, 6.4) and also near the bottom of the second lowest conduction band (FIG. 6.5, 6.6, 6.7).

6.2.3 Seebeck coefficients

We also determined the Seebeck coefficients of Mg_2X in the constant-relaxation-time approximation to validate the accuracy of our calculated relativistic quasiparticle band structures in predicting transport properties. Our calculated values for the Seebeck coefficient

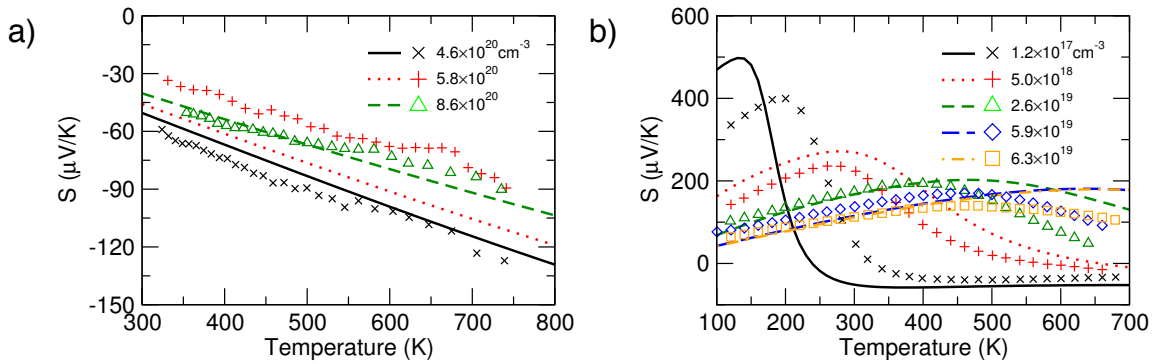

Figure 6.9: Experimental[8, 9] (points) and calculated (lines) values for the Seebeck coefficient of n-type (a) Mg_2Ge and (b) Mg_2Sn as a function of temperature and carrier density. The calculated results are based on GW band structures with spin-orbit effect included and are in good agreement with experimental values.

of Mg_2Si as a function of carrier concentration and temperature were calculated based on PBE and GW band structures and are shown in Fig. 6.8. The calculated data are also compared to the experimental values reported by Tani *et al.* for Bi-doped Mg_2Si.[7] The Seebeck values calculated from PBE show large deviations and wrong trends with temperature compared to experiment. Since PBE underestimates the band gap of Mg_2Si by more than 500 meV, it predicts that electrons get thermally excited across the gap and induce bipolar transport (which greatly reduces the Seebeck coefficient) at much lower temperatures than experiment [Fig. 6.8(a)]. In contrast, the GW data result in much better agreement with experiment for all measured temperatures and carrier concentrations [Fig. 6.8(b)]. In the 300-500 K temperature range, both the experimental and the GW Seebeck coefficients increase in absolute magnitude with temperature for all experimental carrier concentrations and are in good agreement with the experimental Seebeck data. For a free-electorn concentration of 4.3×10^{17} cm^{-3} bipolar transport sets in at approximately 600 K both for the GW and the experimental results. For higher-doped samples the onset of bipolar transport shifts to higher temperatures, since a higher concentration of thermally excited carriers is needed to compete with the doping density. The GW theoretical results slightly overestimate the magnitude of the Seebeck coefficient compared the experimental data at higher temperatures since the theory does not include the decrease of the band gap with increasing temperature and the corresponding stronger contribution of bipolar transport. However, the overall much better qualitative and quantitative agreement of the GW results with experiment compared to PBE demonstrates the important role of quasiparticle corrections to the band gap for the accurate determination of thermoelectric transport coefficients at high temperatures.

We also calculated the Seebeck coefficients for Mg_2Ge and Mg_2Sn using the same computational approach and compared them to available experimental data (Fig. 6.9).[8, 9] In spite of the overall good agreement with experiment for these two materials, two small discrepancies are observed between the theortical and experimental Seebeck coefficients of Mg_2Sn [Fig. 6.9(b)]. First, the calculated Seebeck coefficients show that bipolar transport sets in at a slightly lower temperature than experiment for the lowest reported carrier concentrations. Moreover, the theoretical values for the highest carrier concentration keep increasing with temperature at high temperatures while the experimental values reach a peak and subsequently decrease with increasing temperature. We also attribute these discrepancies to the temperature dependence of the band gap of Mg_2Sn, which we did not take into account in the calculation. The gap is expected to decrease by 0.10$\sim$0.19 eV from 100 K to 700 K as estimated from previously reported β coefficients of -1.7$\sim$-3.2 eV/K.[161, 155] Since the value of the gap of Mg_2Sn is small, even the slight overestimation of its value in our calculations strongly affects the thermally excited carrier concentration and the temperature onset of bipolar transport. Therefore, higher-order theoretical developments that properly account for the temperature dependence of quasi-particle band structures[162] are needed to further improve the predictive accuracy of the evaluated thermoelectric coefficients at high temperatures.

In addition, we calculated the Seebeck coefficients of both p-type and n-type Mg_2X (X = Si, Ge and Sn) for a range of carrier concentrations and temperatures from 300 K to 900 K. The calculated values for Mg_2Si [Fig. 6.10(a) and 6.10(b)] are similar to those of Mg_2Ge [Fig. 6.10(c) and 6.10(d)] at low temperatures as the two compounds have similar band structures. Since the calculated band gap of Mg_2Ge (0.555 eV) is smaller than Mg_2Si (0.728 eV), bipolar transport sets in at lower temperatures in Mg_2Ge. In Mg_2Sn, however, the Seebeck coefficients are greatly reduced by the strong bipolar transport because of its much smaller band gap (0.142 eV). Another observation is that all three materials behave as n-type semiconductors with negative values for the Seebeck coefficient in the limit of high temperature (900 K) and low carrier concentration (10^{17}cm^{-3}). Under these condictions, thermoelectric transport is bipolar and dominated by the intrinsic thermally excited electrons and holes, which occur at approximately equal concentrations. For bipolar transport, the Seebeck coefficient is given by the weighted average of the electron (S_n) and hole (S_p) Seebeck coefficients $S = (\sigma_n S_n + \sigma_p S_p)/(\sigma_n + \sigma_p)$, weighted by the corresponding electrical conductivities for electrons (σ_n) and holes (σ_p).[163] Our data show that the values for the electron and hole Seebeck coefficients are comparable in all three materials, therefore the dominant character under extreme bipolar transport is dominated by the carriers with the highest mobility. Since electrons have a lower overall effective mass that holes in all

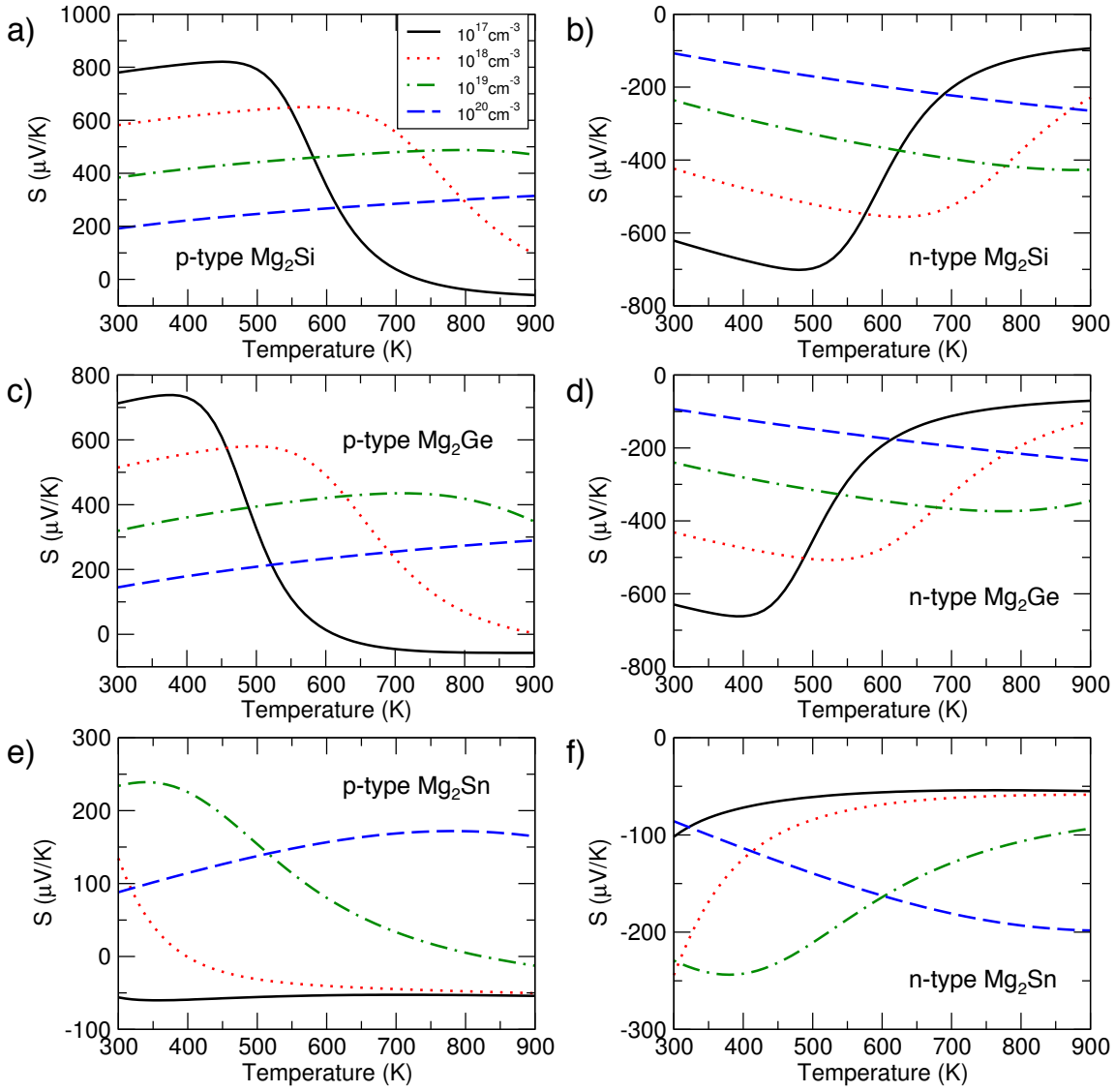

Figure 6.10: Calculated values for the Seebeck coefficient as a function of temperature and carrier concentration for p-type ((a), (c), and (e)) and n-type ((b), (d), and (f)) Mg_2Si, Mg_2Ge, and Mg_2Sn, respectively.

three compounds, the limiting value of the Seebeck coefficient at high temperature and low doping is dominated by the electrons and has a negative sign. The limiting value of the Seebeck coefficient is found to be largest in Mg_2Si ($\sim$100 μV/K) and smallest in Mg_2Sn ($\sim$50 μV/K), due to the stronger asymmetry between electron and hole effective mass in Mg_2Si.

6.3 Conclusions

In conclusion, we calculated the relativistic quasiparticle band structures of Mg_2Si, Mg_2Ge and Mg_2Sn using first-principles calculations based on density functional and many-body perturbation theory. We examined in detail the effects of core electrons and spin-orbit interaction on the band gap. The inclusion of semicore states in pseudopotentials of Mg, Ge, and Sn is found to be important for the accurate determination of the band gap of Mg_2Ge and Mg_2Sn. The band gaps are most accurately determined with spin-orbit coupling effect taken into account and including only the valence electrons in the construction of the generalized plasmon-pole model. Our calculated Seebeck coefficients based on relativistic quasiparticle band structures are in much better agreement with experiment than the results obtaiend from PBE. Our results highlight the important role of quasiparticle corrections to band structures in order to predict Seebeck coefficients at high temperatures and the onset of bipolar-transport effects. We also derived effective Hamiltonians that consistently parameterize the relativistic quasiparticle band structures of all three compounds. Our model Hamiltonians can therefore be applied to accurately simulate the electronic transport properties of Mg_2X compounds, alloys, and devices, including the regime of high temperatures needed for thermoelectric waste-heat recovery.

CHAPTER 7

Summary and Outlook

In conclusion, we applied predictive first-principles computational methods to investigate the properties of novel photovoltaic and thermoelectric materials for energy applications. We investigated the electronic and optical properties of nanoporous Si and few-layer SnSe and GeSe, free-carrier absorption in n-type Si, and thermoelectric transport properteis of p-type SnSe and Mg_2Si, Mg_2Ge, and Mg_2Sn. A summary of the important findings in these studies is as follows.

We used first-principles methods to calculate the electronic and optical properties of nanoporous Si with pore spacing and radius on the order of a few nanometers. We found that the inclusion of nanoscale pores increases the electronic band gaps due to quantum confinement and results in quasi-direct gaps for most examined structures. The visible-range absorption coefficient is greatly improved in nanoporous Si with small pore spacings and appropriately chosen pore sizes. Though quantum confinement reduces the wavelength range for the absorption of solar photons, the enhanced absorption coefficient as well as the reduced reflectivity and increased band gap improve the photovoltaic efficiency compared to bulk Si by a factor of 2.7 and yields a theoretical maximum conversion efficiency of 6.3% for thin-film (135 nm thick) solar cells. Therefore, the enhanced electronic and optical properties of nanoporous Si make it a promising material for thin-film photovoltaic applications. This work focuses on the Si nanostructures with cylindrical pores, and the same method could be applied to those with three-dimensional features as well, which should have stronger quantum confinement effect and could be a promising area to look into in future.

We determined the quasiparticle band structures and optical properties of single-layer, double-layer, and bulk SnSe and GeSe using first-principles calculations. Single-layer and double-layer GeSe have a direct band gap, while the gaps of the SnSe monolayer and bilayer are indirect. Spin-orbit coupling and lack of inversion symmetry in the monolayers results in directionally dependent splitting of the energy bands and anisotropic spin-transport

properties. The exciton binding energy is approximately 300 meV in both monolayer materials, which results in thermally stable excitons at room temperature. We also uncovered the strong absorbance of few-layer SnSe and GeSe in the visible range that reaches values as large as 47%, which suggests potential applications in efficient, ultrathin, and flexible photovoltaic devices with upper bounds to the conversion efficiency that rivals organic and dye-sensitized devices. We expect that even larger exciton binding energy and tunable band gaps could be achieved in SnSe/GeSe heterostructures and these new systems will be studied in the next step.

We discussed plasmon dissipative process, direct transition, and phonon-, charged-impurity-, and plasmon-assisted transitions in n-type Si. Each process creates different features at different wavelengths, which highlights the importance of first-principles calculations for the accurate determination of the free-carrier absorption coefficient. The calculated results are in good agreement with experiment and validates the successful identification of the dominant free-carrier absorption processes. Free-carrier absorption is found to be comparable or even larger than the cross-gap absorption at photon energies close to the band gap for heavily dopes Si, and is thus a nonnegligible source of energy loss in Si solar cells.

We investigated the band structure and electronic transport properties of both the low-temperature *Pnma* and the high-temperature *Cmcm* phase of SnSe. We calculated the band gaps and carrier effective masses and we found that both phases exhibit multiple local band extrema near the band edges that need to be considered when evaluating the thermoelectric properties for this material. We determined the electrical conductivity to be highest along the *b* axis and smallest along the *a* axis for various carrier concentrations. The other transport properties also show a significant degree of anisotropy between the perpendicular direction (*a* axis) and the two in-plane directions (*b* and *c* axes). Bipolar effects strongly affect electronic transport at high temperatures and low carrier concentrations, and cause a sharp decrease and sign reversal of the Seebeck coefficients. The difference between our calculated transport properties and the experimental results in the range of low carrier concentration and high temperature may be attributed to the possible change of the nature or concentration of defects and dopant impurities in the material due to the increasing temperature and the phase transition. Our calculated transport coefficients shed light into recent experimental measurements that reported a remarkably high figure-of-merit value (2.6) for *Cmcm*-SnSe. Our results predict that SnSe would show optimal thermoelectric performance at high temperature when doped in the 10^{19}–10^{20} cm^{-3} range. Our future work will focus on calculating the electronic structure of SnSe at high temperature, including lattice expansion and crystal disorder due to vibrations.

We calculated the relativistic quasiparticle band structures of Mg_2Si, Mg_2Ge and Mg_2Sn using first-principles calculations based on density functional and many-body perturbation theory. We examined in detail the effects of core electrons and spin-orbit interaction on the band gap. The inclusion of semicore states in pseudopotentials of Mg, Ge, and Sn is found to be important for the accurate determination of the band gap of Mg_2Ge and Mg_2Sn. The band gaps are most accurately determined with spin-orbit coupling effect taken into account and including only the valence electrons in the construction of the generalized plasmon-pole model. Our calculated Seebeck coefficients based on relativistic quasiparticle band structures are in much better agreement with experiment than the results obtaiend from PBE. Our results highlight the important role of quasiparticle corrections to band structures in order to predict Seebeck coefficients at high temperatures and the onset of bipolar-transport effects. We also derived effective Hamiltonians that consistently parameterize the relativistic quasiparticle band structures of all three compounds. Our model Hamiltonians can therefore be applied to accurately simulate the electronic transport properties of Mg_2X compounds, alloys, and devices, including the regime of high temperatures needed for thermoelectric waste-heat recovery.

BIBLIOGRAPHY

[1] Deslippe, J., Samsonidze, G., Strubbe, D. A., Jain, M., Cohen, M. L., and Louie, S. G., "BerkeleyGW: A massively parallel computer package for the calculation of the quasiparticle and optical properties of materials and nanostructures," *Computer Physics Communications*, Vol. 183, No. 6, 2012, pp. 1269 – 1289.

[2] Jellison, G. E., Chisholm, M. F., and Gorbatkin, S. M., "Optical functions of chemical vapor deposited thinfilm silicon determined by spectroscopic ellipsometry," *Applied Physics Letters*, Vol. 62, No. 25, 1993, pp. 3348–3350.

[3] Spitzer, W. and Fan, H. Y., "Infrared Absorption in n-Type Silicon," *Phys. Rev.*, Vol. 108, Oct 1957, pp. 268–271.

[4] Green, M. A., "Self-Consistent Optical Parameters of Intrinsic Silicon at 300 K Including Temperature Coefficients," *Solar Energy Materials and Solar Cells*, Vol. 92, No. 11, 2008, pp. 1305 – 1310.

[5] Zhao, L., Lo, S., Zhang, Y., Sun, H., Tan, G., Uher, C., Wolverton, C., Dravid, V. P., and Kanatzidis, M. G., "Ultralow thermal conductivity and high thermoelectric figure of merit in SnSe crystals," *Nature*, Vol. 508, No. 7496, 2014, pp. 373–377.

[6] Chen, C.-L., Wang, H., Chen, Y.-Y., Day, T., and Snyder, J., "Thermoelectric properties of p-type polycrystalline SnSe doped with Ag," *J. Mater. Chem. A*, 2014, pp. –, in press.

[7] ichi Tani, J. and Kido, H., "Thermoelectric properties of Bi-doped Mg_2Si semiconductors," *Physica B: Condensed Matter*, Vol. 364, No. 14, 2005, pp. 218 – 224.

[8] Gao, H., Zhu, T., Zhao, X., and Deng, Y., "Influence of Sb doping on thermoelectric properties of Mg2Ge materials," *Intermetallics*, Vol. 56, 2015, pp. 33 – 36.

[9] Chen, H. Y., Savvides, N., Dasgupta, T., Stiewe, C., and Mueller, E., "Electronic and thermal transport properties of Mg2Sn crystals containing finely dispersed eutectic structures," *physica status solidi (a)*, Vol. 207, No. 11, 2010, pp. 2523–2531.

[10] Nakamura, M., Kouji, Y., Chiba, Y., Hakuma, H., Kobayashi, T., and Nakada, T., "Achievement of 19.7% efficiency with a small-sized Cu(InGa)(SeS)2 solar cells prepared by sulfurization after selenizaion process with Zn-based buffer," *2013 IEEE 39th Photovoltaic Specialists Conference (PVSC)*, June 2013, pp. 0849–0852.

[11] Fraunhofer, I., "Photovoltaics report," *Disponible sur: http://www. ise. fraunhofer. de/en/downloads-englisch/pdf-files-englisch/photovoltaics-report-slides. pdf/view, rapport publié en*, 2014.

[12] Goldsmid, H., "XXVII. Thermoelectric Applications of Semiconductors," *International Journal Of Electronics*, Vol. 1, No. 2, 1955, pp. 218–222.

[13] Wood, C., "Materials for thermoelectric energy conversion," *Reports on Progress in Physics*, Vol. 51, No. 4, 1988, pp. 459.

[14] Pei, Y., LaLonde, A., Iwanaga, S., and Snyder, G. J., "High thermoelectric figure of merit in heavy hole dominated PbTe," *Energy Environ. Sci.*, Vol. 4, 2011, pp. 2085–2089.

[15] Heremans, J. P., Jovovic, V., Toberer, E. S., Saramat, A., Kurosaki, K., Charoenphakdee, A., Yamanaka, S., and Snyder, G. J., "Enhancement of Thermoelectric Efficiency in PbTe by Distortion of the Electronic Density of States," *Science*, Vol. 321, No. 5888, 2008, pp. 554–557.

[16] Liu, W., Zhang, Q., Yin, K., Chi, H., Zhou, X., Tang, X., and Uher, C., "High figure of merit and thermoelectric properties of Bi-doped $Mg_2Si_{0.4}Sn_{0.6}$ solid solutions," *Journal of Solid State Chemistry*, Vol. 203, 2013, pp. 333 – 339.

[17] Liu, W., Tan, X., Yin, K., Liu, H., Tang, X., Shi, J., Zhang, Q., and Uher, C., "Convergence of conduction bands as a means of enhancing thermoelectric performance of n-type $Mg_2Si_{1-x}Sn_x$ solid solutions," *Physical Review Letters*, Vol. 108, No. 16, apr 2012, pp. 166601.

[18] McAllister, A., berg, D., Schleife, A., and Kioupakis, E., "Auger recombination in sodium-iodide scintillators from first principles," *Applied Physics Letters*, Vol. 106, No. 14, 2015, pp. 141901.

[19] Bayerl, D. and Kioupakis, E., "Theoretical limits of thermoelectric figure of merit in n-type TiO_2 polymorphs," *Phys. Rev. B*, Vol. 91, Apr 2015, pp. 165104.

[20] Shi, G. and Kioupakis, E., "Quasiparticle band structures and thermoelectric transport properties of p-type SnSe," *Journal of Applied Physics*, Vol. 117, No. 6, 2015, pp. 065103.

[21] Bayerl, D. and Kioupakis, E., "Visible-Wavelength Polarized-Light Emission with Small-Diameter InN Nanowires," *Nano Letters*, Vol. 14, No. 7, 2014, pp. 3709–3714, PMID: 24527880.

[22] Bayerl, D., Islam, S., Jones, C. M., Protasenko, V., Jena, D., and Kioupakis, E., "Deep ultraviolet emission from ultra-thin GaN/AlN heterostructures," *Applied Physics Letters*, Vol. 109, No. 24, 2016, pp. 241102.

[23] Mengle, K. A., Shi, G., Bayerl, D., and Kioupakis, E., "First-principles calculations of the near-edge optical properties of -Ga2O3," *Applied Physics Letters*, Vol. 109, No. 21, 2016, pp. 212104.

[24] Shi, G. and Kioupakis, E., "Electronic and Optical Properties of Nanoporous Silicon for Solar-Cell Applications," *ACS Photonics*, Vol. 2, No. 2, 2015, pp. 208–215.

[25] Man, M. K., Deckoff-Jones, S., Winchester, A., Shi, G., Gupta, G., Mohite, A. D., Kar, S., Kioupakis, E., Talapatra, S., and Dani, K. M., "Protecting the properties of monolayer MoS2 on silicon based substrates with an atomically thin buffer," *Scientific reports*, Vol. 6, 2016, pp. 20890.

[26] Shi, G. and Kioupakis, E., "Anisotropic Spin Transport and Strong Visible-Light Absorbance in Few-Layer SnSe and GeSe," *Nano Letters*, Vol. 15, No. 10, 2015, pp. 6926–6931, PMID: 26393677.

[27] Toulouse, A. S., Isaacoff, B. P., Shi, G., Matuchová, M., Kioupakis, E., and Merlin, R., "Frenkel-like Wannier-Mott excitons in few-layer PbI_2," *Phys. Rev. B*, Vol. 91, Apr 2015, pp. 165308.

[28] Lee, J., Du, C., Sun, K., Kioupakis, E., and Lu, W. D., "Tuning Ionic Transport in Memristive Devices by Graphene with Engineered Nanopores," *ACS Nano*, Vol. 10, No. 3, 2016, pp. 3571–3579, PMID: 26954948.

[29] Lee, J., Lu, W., and Kioupakis, E., "Electronic properties of tantalum pentoxide polymorphs from first-principles calculations," *Applied Physics Letters*, Vol. 105, No. 20, 2014, pp. 202108.

[30] Senabulya, N., Feldberg, N., Makin, R. A., Yang, Y., Shi, G., Jones, C. M., Kioupakis, E., Mathis, J., Clarke, R., and Durbin, S. M., "Stabilization of orthorhombic phase in single-crystal ZnSnN2 films," *AIP Advances*, Vol. 6, No. 7, 2016, pp. 075019.

[31] Jokisaari, J. R., Bayerl, D., Zhang, K., Xie, L., Nie, Y., Schlom, D. G., Kioupakis, E., Graham, G. W., and Pan, X., "Polarization-Dependent Raman Spectroscopy of Epitaxial TiO2(B) Thin Films," *Chemistry of Materials*, Vol. 27, No. 23, 2015, pp. 7896–7902.

[32] Chung, K., McAllister, A., Bilby, D., Kim, B.-G., Kwon, M. S., Kioupakis, E., and Kim, J., "Designing interchain and intrachain properties of conjugated polymers for latent optical information encoding," *Chem. Sci.*, Vol. 6, 2015, pp. 6980–6985.

[33] Olvera, A., Shi, G., Djieutedjeu, H., Page, A., Uher, C., Kioupakis, E., and Poudeu, P. F. P., "Pb7Bi4Se13: A Lillianite Homologue with Promising Thermoelectric Properties," *Inorganic Chemistry*, Vol. 54, No. 3, 2015, pp. 746–755, PMID: 25089857.

[34] Chi, H., Kim, H., Thomas, J. C., Shi, G., Sun, K., Abeykoon, M., Bozin, E. S., Shi, X., Li, Q., Shi, X., Kioupakis, E., Van der Ven, A., Kaviany, M., and Uher,

C., "Low-temperature structural and transport anomalies in Cu_2Se," *Phys. Rev. B*, Vol. 89, May 2014, pp. 195209.

[35] Hohenberg, P. and Kohn, W., "Inhomogeneous Electron Gas," *Phys. Rev.*, Vol. 136, Nov 1964, pp. B864–B871.

[36] Kohn, W. and Sham, L. J., "Self-Consistent Equations Including Exchange and Correlation Effects," *Phys. Rev.*, Vol. 140, Nov 1965, pp. A1133–A1138.

[37] Perdew, J. P. and Zunger, A., "Self-interaction correction to density-functional approximations for many-electron systems," *Phys. Rev. B*, Vol. 23, May 1981, pp. 5048–5079.

[38] Ceperley, D. M. and Alder, B. J., "Ground State of the Electron Gas by a Stochastic Method," *Phys. Rev. Lett.*, Vol. 45, Aug 1980, pp. 566–569.

[39] Perdew, J. P., Burke, K., and Ernzerhof, M., "Generalized Gradient Approximation Made Simple," *Phys. Rev. Lett.*, Vol. 77, No. 18, Oct 1996, pp. 3865–3868.

[40] Giannozzi, P., Baroni, S., Bonini, N., Calandra, M., Car, R., Cavazzoni, C., Ceresoli, D., Chiarotti, G. L., Cococcioni, M., Dabo, I., Corso, A. D., de Gironcoli, S., Fabris, S., Fratesi, G., Gebauer, R., Gerstmann, U., Gougoussis, C., Kokalj, A., Lazzeri, M., Martin-Samos, L., Marzari, N., Mauri, F., Mazzarello, R., Paolini, S., Pasquarello, A., Paulatto, L., Sbraccia, C., Scandolo, S., Sclauzero, G., Seitsonen, A. P., Smogunov, A., Umari, P., and Wentzcovitch, R. M., "QUANTUM ESPRESSO: A Modular and Open-Source Software Project for Quantum Simulations of Materials," *Journal of Physics: Condensed Matter*, Vol. 21, No. 39, 2009, pp. 395502.

[41] Kresse, G. and Furthmüller, J., "Efficient iterative schemes for *ab initio* total-energy calculations using a plane-wave basis set," *Phys. Rev. B*, Vol. 54, Oct 1996, pp. 11169–11186.

[42] Hedin, L., "New Method for Calculating the One-Particle Green's Function with Application to the Electron-Gas Problem," *Phys. Rev.*, Vol. 139, Aug 1965, pp. A796–A823.

[43] Hybertsen, M. S. and Louie, S. G., "First-Principles Theory of Quasiparticles: Calculation of Band Gaps in Semiconductors and Insulators," *Phys. Rev. Lett.*, Vol. 55, Sep 1985, pp. 1418–1421.

[44] Aryasetiawan, F. and Gunnarsson, O., "The GW method," *Reports on Progress in Physics*, Vol. 61, No. 3, 1998, pp. 237.

[45] Rohlfing, M. and Louie, S. G., "Electron-hole excitations and optical spectra from first principles," *Phys. Rev. B*, Vol. 62, Aug 2000, pp. 4927–4944.

[46] Yang, L., Spataru, C. D., Louie, S. G., and Chou, M. Y., "Enhanced Electron-Hole Interaction and Optical Absorption in a Silicon Nanowire," *Phys. Rev. B*, Vol. 75, May 2007, pp. 201304.

[47] Bruno, M., Palummo, M., Marini, A., Del Sole, R., and Ossicini, S., "From Si Nanowires to Porous Silicon: The Role of Excitonic Effects," *Phys. Rev. Lett.*, Vol. 98, Jan 2007, pp. 036807.

[48] Noffsinger, J., Kioupakis, E., Van de Walle, C. G., Louie, S. G., and Cohen, M. L., "Phonon-Assisted Optical Absorption in Silicon from First Principles," *Phys. Rev. Lett.*, Vol. 108, Apr 2012, pp. 167402.

[49] Liu, Y., Sun, S., Xu, J., Zhao, L., Sun, H., Li, J., Mu, W. W., Xu, L., and Chen, K. J., "Broadband Antireflection and Absorption Enhancement by Forming Nano-Patterned Si Structures for Solar Cells," *Opt. Express*, Vol. 19, No. S5, Sep 2011, pp. A1051–A1056.

[50] Garnett, E. and Yang, P., "Light Trapping in Silicon Nanowire Solar Cells," *Nano Letters*, Vol. 10, No. 3, 2010, pp. 1082–1087, PMID: 20108969.

[51] Zhu, J., Yu, Z., Burkhard, G. F., Hsu, C.-M., Connor, S. T., Xu, Y., Wang, Q., McGehee, M., Fan, S., and Cui, Y., "Optical Absorption Enhancement in Amorphous Silicon Nanowire and Nanocone Arrays," *Nano Letters*, Vol. 9, No. 1, 2009, pp. 279–282.

[52] Tsakalakos, L., Balch, J., Fronheiser, J., Korevaar, B. A., Sulima, O., and Rand, J., "Silicon Nanowire Solar Cells," *Applied Physics Letters*, Vol. 91, No. 23, 2007, pp. 233117.

[53] Cloutier, S. G., Kossyrev, P. A., and Xu, J., "Optical Gain and Stimulated Emission in Periodic Nanopatterned Crystalline Silicon," *Nat Mater*, Vol. 4, No. 12, 2005, pp. 887–891.

[54] Canham, L. T., "Silicon Quantum Wire Array Fabrication by Electrochemical and Chemical Dissolution of Wafers," *Applied Physics Letters*, Vol. 57, No. 10, 1990, pp. 1046–1048.

[55] Eckhoff, D. A., Sutin, J. D. B., Clegg, R. M., Gratton, E., Rogozhina, E. V., and Braun, P. V., "Optical Characterization of Ultrasmall Si Nanoparticles Prepared through Electrochemical Dispersion of Bulk Si," *The Journal of Physical Chemistry B*, Vol. 109, No. 42, 2005, pp. 19786–19797.

[56] Maier-Flaig, F., Rinck, J., Stephan, M., Bocksrocker, T., Bruns, M., Kübel, C., Powell, A. K., Ozin, G. A., and Lemmer, U., "Multicolor Silicon Light-Emitting Diodes (SiLEDs)," *Nano Letters*, Vol. 13, No. 2, 2013, pp. 475–480.

[57] Van de Walle, C. G. and Northrup, J. E., *FIRST-PRINCIPLES CALCULATIONS OF LIGHT EMISSION FROM SILICON-BASED MATERIALS*, chap. 16, pp. 329–344.

[58] Hybertsen, M. S., "Absorption and Emission of Light in Nanoscale Silicon Structures," *Phys. Rev. Lett.*, Vol. 72, Mar 1994, pp. 1514–1517.

[59] d'Avezac, M., Luo, J.-W., Chanier, T., and Zunger, A., "Genetic-Algorithm Discovery of a Direct-Gap and Optically Allowed Superstructure from Indirect-Gap Si and Ge Semiconductors," *Phys. Rev. Lett.*, Vol. 108, Jan 2012, pp. 027401.

[60] Peelaers, H., Partoens, B., and Peeters, F. M., "Electronic and Dynamical Properties of Si/Ge Core-Shell Nanowires," *Phys. Rev. B*, Vol. 82, Sep 2010, pp. 113411.

[61] Staebler, D. L. and Wronski, C. R., "Optically induced conductivity changes in discharge-produced hydrogenated amorphous silicon," *Journal of Applied Physics*, Vol. 51, No. 6, 1980, pp. 3262–3268.

[62] Perdew, J. P. and Zunger, A., "Self-Interaction Correction to Density-Functional Approximations for Many-Electron Systems," *Phys. Rev. B*, Vol. 23, 1981, pp. 5048.

[63] Ihm, J., Zunger, A., and Cohen, M. L., "Momentum-space formalism for the total energy of solids," *Journal of Physics C: Solid State Physics*, Vol. 12, No. 21, 1979, pp. 4409.

[64] Troullier, N. and Martins, J. L., "Efficient pseudopotentials for plane-wave calculations," *Phys. Rev. B*, Vol. 43, Jan 1991, pp. 1993–2006.

[65] Hybertsen, M. S. and Louie, S. G., "Electron correlation in semiconductors and insulators: Band gaps and quasiparticle energies," *Phys. Rev. B*, Vol. 34, Oct 1986, pp. 5390–5413.

[66] Deslippe, J., Samsonidze, G., Jain, M., Cohen, M. L., and Louie, S. G., "Coulomb-Hole Summations and Energies for GW Calculations with Limited Number of Empty Orbitals: A Modified Static Remainder Approach," *Phys. Rev. B*, Vol. 87, Apr 2013, pp. 165124.

[67] Monkhorst, H. J. and Pack, J. D., "Special Points for Brillouin-Zone Integrations," *Phys. Rev. B*, Vol. 13, No. 12, Jun 1976, pp. 5188–5192.

[68] Wu, X. L., Xiong, S. J., Fan, D. L., Gu, Y., Bao, X. M., Siu, G. G., and Stokes, M. J., "Stabilized electronic state and its luminescence at the surface of oxygen-passivated porous silicon," *Phys. Rev. B*, Vol. 62, Sep 2000, pp. R7759–R7762.

[69] Haick, H., Hurley, P. T., Hochbaum, A. I., Yang, P., and Lewis, N. S., "Electrical Characteristics and Chemical Stability of Non-Oxidized, Methyl-Terminated Silicon Nanowires," *Journal of the American Chemical Society*, Vol. 128, No. 28, 2006, pp. 8990–8991, PMID: 16834345.

[70] Buriak, J. M., "Organometallic Chemistry on Silicon and Germanium Surfaces," *Chemical Reviews*, Vol. 102, No. 5, 2002, pp. 1271–1308, PMID: 11996538.

[71] Bludau, W., Onton, A., and Heinke, W., "Temperature dependence of the band gap of silicon," *Journal of Applied Physics*, Vol. 45, No. 4, 1974, pp. 1846.

[72] Bruggeman, D. A. G., "Berechnung verschiedener physikalischer Konstanten von heterogenen Substanzen. I. Dielektrizitätskonstanten und Leitfähigkeiten der Mischkörper aus isotropen Substanzen," *Annalen der Physik*, Vol. 416, No. 7, 1935, pp. 636–664.

[73] Van Beek, L., "Dielectric Behaviour of Heterogeneous Systems," *Progress in dielectrics*, Vol. 7, 1967, pp. 69–114.

[74] Torres-Costa, V. and Martin-Palma, R., "8 - Optical properties of porous silicon materials for biomedical applications," *Porous Silicon for Biomedical Applications*, edited by H. A. Santos, Woodhead Publishing, 2014, pp. 185 – 222.

[75] Zucca, R. R. L. and Shen, Y. R., "Wavelength-Modulation Spectra of Some Semiconductors," *Phys. Rev. B*, Vol. 1, No. 6, Mar 1970, pp. 2668–2676.

[76] Albrecht, S., Reining, L., Del Sole, R., and Onida, G., "*Ab Initio* Calculation of Excitonic Effects in the Optical Spectra of Semiconductors," *Phys. Rev. Lett.*, Vol. 80, May 1998, pp. 4510–4513.

[77] ASTM G 173-03: *Standard tables for reference solar spectral irradiances: direct normal and hemispherical on 37° tilted surface*. West Conshohoken, PA: ASTM International; 2003. doi:10.1520/G0173-03R12.

[78] Mak, K. F., Lee, C., Hone, J., Shan, J., and Heinz, T. F., "Atomically Thin MoS_2: A New Direct-Gap Semiconductor," *Phys. Rev. Lett.*, Vol. 105, Sep 2010, pp. 136805.

[79] Splendiani, A., Sun, L., Zhang, Y., Li, T., Kim, J., Chim, C.-Y., Galli, G., and Wang, F., "Emerging photoluminescence in monolayer MoS2." *Nano Lett.*, Vol. 10, No. 4, April 2010, pp. 1271–1275.

[80] Baugher, B. W., Churchill, H. O., Yang, Y., and Jarillo, "Optoelectronic devices based on electrically tunable p-n diodes in a monolayer dichalcogenide," *Nat. Nanotechnol.*, Vol. 9, No. 4, 2014, pp. 262–267.

[81] Pospischil, A., Furchi, M. M., and Mueller, T., "Solar-energy conversion and light emission in an atomic monolayer p-n diode," *Nat. Nanotechnol.*, Vol. 9, No. 4, 2014, pp. 257–261.

[82] Ross, J. S., Klement, P., Jones, A. M., Ghimire, N. J., Yan, J., MandrusD.G., Taniguchi, T., Watanabe, K., Kitamura, K., Yao, W., Cobden, D. H., and Xu, X., "Electrically tunable excitonic light-emitting diodes based on monolayer WSe2 p-n junctions," *Nat. Nanotechnol.*, Vol. 9, No. 4, 2014, pp. 268–272.

[83] Bernardi, M., Palummo, M., and Grossman, J. C., "Extraordinary Sunlight Absorption and One Nanometer Thick Photovoltaics Using Two-Dimensional Monolayer Materials," *Nano Lett.*, Vol. 13, No. 8, 2013, pp. 3664–3670, PMID: 23750910.

[84] Xiao, D., Liu, G.-B., Feng, W., Xu, X., and Yao, W., "Coupled Spin and Valley Physics in Monolayers of MoS_{2} and Other Group-VI Dichalcogenides," *Phys. Rev. Lett.*, Vol. 108, No. 19, May 2012, pp. 196802.

[85] Shi, G. and Kioupakis, E., "Quasiparticle band structures and thermoelectric transport properties of p-type SnSe," *J. Appl. Phys.*, Vol. 117, No. 6, 2015, pp. 065103.

[86] Nair, M. T. S. and Nair, P. K., "Simplified chemical deposition technique for good quality SnS thin films," *Semicond. Sci. Tech.*, Vol. 6, No. 2, 1991, pp. 132.

[87] Tritsaris, G. A., Malone, B. D., and Kaxiras, E., "Optoelectronic properties of single-layer, double-layer, and bulk tin sulfide: A theoretical study," *J. Appl. Phys.*, Vol. 113, No. 23, 2013, pp. 233507.

[88] Li, L., Chen, Z., Hu, Y., Wang, X., Zhang, T., Chen, W., and Wang, Q., "Single-Layer Single-Crystalline SnSe Nanosheets," *J. Am. Chem. Soc.*, Vol. 135, No. 4, 2013, pp. 1213–1216, PMID: 23311291.

[89] Singh, A. K. and Hennig, R. G., "Computational prediction of two-dimensional group-IV mono-chalcogenides," *Appl. Phys. Lett.*, Vol. 105, No. 4, 2014, pp. 042103.

[90] Rondinelli, J. M. and Kioupakis, E., "Predicting and Designing Optical Properties of Inorganic Materials," *Annu. Rev. Mater. Res.*, Vol. 45, 2015, pp. 491–518.

[91] Perdew, J. P., Burke, K., and Ernzerhof, M., "Generalized Gradient Approximation Made Simple," *Phys. Rev. Lett.*, Vol. 77, Oct 1996, pp. 3865–3868.

[92] Kresse, G. and Joubert, D., "From ultrasoft pseudopotentials to the projector augmented-wave method," *Phys. Rev. B*, Vol. 59, Jan 1999, pp. 1758–1775.

[93] Hybertsen, M. S. and Louie, S. G., "Spin-orbit splitting in semiconductors and insulators from the ¡i¿ab initio¡/i¿ pseudopotential," *Phys. Rev. B*, Vol. 34, Aug 1986, pp. 2920–2922.

[94] Ismail-Beigi, S., "Truncation of periodic image interactions for confined systems," *Phys. Rev. B*, Vol. 73, Jun 2006, pp. 233103.

[95] Marzari, N., Mostofi, A. A., Yates, J. R., Souza, I., and Vanderbilt, D., "Maximally localized Wannier functions: Theory and applications," *Rev. Mod. Phys.*, Vol. 84, Oct 2012, pp. 1419–1475.

[96] Mostofi, A. A., Yates, J. R., Lee, Y.-S., Souza, I., Vanderbilt, D., and Marzari, N., "wannier90: A tool for obtaining maximally-localised Wannier functions," *Comput. Phys. Commun.*, Vol. 178, No. 9, 2008, pp. 685 – 699.

[97] Olvera, A., Shi, G., Djieutedjeu, H., Page, A., Uher, C., Kioupakis, E., and Poudeu, P. F. P., "$Pb_7Bi_4Se_{13}$: A Lillianite Homologue with Promising Thermoelectric Properties." *Inorg. Chem.*, Vol. 54, Aug. 2015, pp. 746–755.

[98] Toulouse, A. S., Isaacoff, B. P., Shi, G., Matuchov, M., Kioupakis, E., and Merlin, R., "Frenkel-like Wannier-Mott excitons in few-layer PbI[dw]2[/dw]," *Phys. Rev. B*, Vol. 91, 2015, pp. 165308.

[99] Parenteau, M. and Carlone, C., "Influence of temperature and pressure on the electronic transitions in SnS and SnSe semiconductors," *Phys. Rev. B*, Vol. 41, Mar 1990, pp. 5227–5234.

[100] Lukeš, F., "Optical and photoelectric properties of GeSe in the energy range 0.5-1.5 eV," *Czech. J. Phys. B*, Vol. 18, No. 6, 1968, pp. 784–794.

[101] Elkorashy, A. M., "Temperature Dependence of Two-Dimensional Optical Energy Gap for Germanium Selenide Single Crystals," *Phys. Status Solidi B*, Vol. 146, No. 1, 1988, pp. 279–285.

[102] Fei, R. and Yang, L., "Strain-engineering the anisotropic electrical conductance of few-layer black phosphorus." *Nano Lett.*, Vol. 14, No. 5, May 2014, pp. 2884–9.

[103] Zhu, Z. Y., Cheng, Y. C., and Schwingenschlögl, U., "Giant spin-orbit-induced spin splitting in two-dimensional transition-metal dichalcogenide semiconductors," *Phys. Rev. B*, Vol. 84, Oct 2011, pp. 153402.

[104] Bayerl, D. and Kioupakis, E., "Visible-Wavelength Polarized Light Emission with Small-Diameter InN Nanowires," *Nano Lett.*, Vol. 14, No. 7, July 2014, pp. 3709–3714.

[105] Tran, V., Soklaski, R., Liang, Y., and Yang, L., "Layer-controlled band gap and anisotropic excitons in few-layer black phosphorus," *Phys. Rev. B*, Vol. 89, No. 23, June 2014, pp. 235319.

[106] Shi, G. and Kioupakis, E., "Electronic and Optical Properties of Nanoporous Silicon for Solar-Cell Applications," *ACS Photonics*, Vol. 2, 2015, pp. 208–215.

[107] Kioupakis, E., Rinke, P., Schleife, A., Bechstedt, F., and Van de Walle, C. G., "Free-carrier absorption in nitrides from first principles," *Phys. Rev. B*, Vol. 81, Jun 2010, pp. 241201.

[108] Kioupakis, E., Rinke, P., and de Walle, C. G. V., "Determination of Internal Loss in Nitride Lasers from First Principles," *Applied Physics Express*, Vol. 3, No. 8, 2010, pp. 082101.

[109] Peelaers, H., Kioupakis, E., and Van de Walle, C. G., "Fundamental limits on optical transparency of transparent conducting oxides: Free-carrier absorption in SnO2," *Applied Physics Letters*, Vol. 100, No. 1, 2012.

[110] Peelaers, H., Kioupakis, E., and Van de Walle, C. G., "Free-carrier absorption in transparent conducting oxides: Phonon and impurity scattering in $\mathrm{SnO_2}$," *Phys. Rev. B*, Vol. 92, Dec 2015, pp. 235201.

[111] Brown, A. M., Sundararaman, R., Narang, P., Goddard, W. A., and Atwater, H. A.

[112] Cappellini, G., Del Sole, R., Reining, L., and Bechstedt, F., "Model dielectric function for semiconductors," *Phys. Rev. B*, Vol. 47, Apr 1993, pp. 9892–9895.

[113] Troullier, N. and Martins, J. L., "Efficient Pseudopotentials for Plane-Wave Calculations," *Phys. Rev. B*, Vol. 43, No. 3, Jan 1991, pp. 1993–2006.

[114] Baroni, S., de Gironcoli, S., Dal Corso, A., and Giannozzi, P., "Phonons and related crystal properties from density-functional perturbation theory," *Rev. Mod. Phys.*, Vol. 73, Jul 2001, pp. 515–562.

[115] Bernardi, M., Vigil-Fowler, D., Lischner, J., Neaton, J. B., and Louie, S. G., "*Ab Initio* Study of Hot Carriers in the First Picosecond after Sunlight Absorption in Silicon," *Phys. Rev. Lett.*, Vol. 112, Jun 2014, pp. 257402.

[116] Pei, Y., Shi, X., LaLonde, A., Wang, H., Chen, L., and Snyder, G., "Convergence of electronic bands for high performance bulk thermoelectrics," *Nature*, Vol. 473, No. 7345, 2011, pp. 66–69.

[117] Adouby, K., Pérez-Vicente, C., Jumas, J. C., Fourcade, R., and Touré, A. A., "Structure and temperature transformation of SnSe. Stabilization of a new cubic phase Sn4Bi2Se7," *Zeitschrift fur Kristallographie*, Vol. 213, Jan. 1998, pp. 343–349.

[118] Monkhorst, H. J. and Pack, J. D., "Special points for Brillouin-zone integrations," *Phys. Rev. B*, Vol. 13, Jun 1976, pp. 5188–5192.

[119] Kioupakis, E., Tiago, M. L., and Louie, S. G., "Quasiparticle electronic structure of bismuth telluride in the GW approximation," *Phys. Rev. B*, Vol. 82, Dec 2010, pp. 245203.

[120] Scheidemantel, T. J., Ambrosch-Draxl, C., Thonhauser, T., Badding, J. V., and Sofo, J. O., "Transport coefficients from first-principles calculations," *Phys. Rev. B*, Vol. 68, Sep 2003, pp. 125210.

[121] Park, M. S., Song, J.-H., Medvedeva, J. E., Kim, M., Kim, I. G., and Freeman, A. J., "Electronic structure and volume effect on thermoelectric transport in p-type Bi and Sb tellurides," *Phys. Rev. B*, Vol. 81, Apr 2010, pp. 155211.

[122] Parker, D. and Singh, D. J., "Alkaline earth lead and tin compounds Ae 2 Pb, Ae 2 Sn, Ae = Ca, Sr, Ba, as thermoelectric materials," *Science and Technology of Advanced Materials*, Vol. 14, No. 5, 2013, pp. 055003.

[123] Yang, J., "Theory of Thermal Conductivity," *Thermal Conductivity*, edited by T. Tritt, Physics of Solids and Liquids, Springer US, 2004, pp. 1–20.

[124] Goldsmid, H. J., "The Thermal Conductivity of Bismuth Telluride," *Proceedings of the Physical Society. Section B*, Vol. 69, No. 2, 1956, pp. 203.

[125] Zaitsev, V. K., Fedorov, M. I., Gurieva, E. A., Eremin, I. S., Konstantinov, P. P., Samunin, A. Y., and Vedernikov, M. V., "Highly effective $Mg_2Si_{1-x}Sn_x$ thermoelectrics," *Phys. Rev. B*, Vol. 74, Jul 2006, pp. 045207.

[126] Li, W., Lindsay, L., Broido, D. A., Stewart, D. A., and Mingo, N., "Thermal conductivity of bulk and nanowire $Mg_2Si_xSn_{1-x}$ alloys from first principles," *Physical Review B - Condensed Matter and Materials Physics*, Vol. 86, No. 17, 2012, pp. 174307.

[127] Liu, W., Kim, H. S., Chen, S., Jie, Q., Lv, B., Yao, M., Ren, Z., Opeil, C. P., Wilson, S., Chu, C.-W., and Ren, Z., "n-type thermoelectric material $Mg_2Sn_{0.75}Ge_{0.25}$ for high power generation." *Proceedings of the National Academy of Sciences*, Vol. 112, No. 11, 2015, pp. 3269–74.

[128] Sun, J. and Singh, D. J., "Thermoelectric Properties of Mg2(Ge,Sn): Model and Optimization of ZT," *Physical Review Applied*, Vol. 5, No. 2, 2016, pp. 024006.

[129] Viennois, R., Colinet, C., Jund, P., and Tédenac, J. C., "Phase stability of ternary antifluorite type compounds in the quasi-binary systems Mg 2X-Mg 2Y (X, y = Si, Ge, Sn) via ab-initio calculations," *Intermetallics*, Vol. 31, 2012, pp. 146–151.

[130] Yin, K., Su, X., Yan, Y., You, Y., Zhang, Q., Uher, C., Kanatzidis, M. G., and Tang, X., "Optimization of the Electronic Band Structure and the Lattice Thermal Conductivity of Solid Solutions According to Simple Calculations: A Canonical Example of the Mg2Si1xyGexSny Ternary Solid Solution," *Chemistry of Materials*, Vol. 28, No. 15, 2016, pp. 5538–5548.

[131] Khan, A. U., Vlachos, N., and Kyratsi, T., "High thermoelectric figure of merit of Mg2Si 0.55Sn0.4Ge0.05 materials doped with Bi and Sb," *Scripta Materialia*, Vol. 69, No. 8, 2013, pp. 606–609.

[132] Zhang, L., Xiao, P., Shi, L., Henkelman, G., Goodenough, J. B., and Zhou, J., "Suppressing the bipolar contribution to the thermoelectric properties of $Mg_2Si_{0.4}Sn_{0.6}$ by Ge substitution," *Journal of Applied Physics*, Vol. 117, No. 15, 2015, pp. 0–11.

[133] Au-Yang, M. Y. and Cohen, M. L., "Electronic Structure and Optical Properties of Mg_2Si, Mg_2Ge, and Mg_2Sn," *Phys. Rev.*, Vol. 178, Feb 1969, pp. 1358–1364.

[134] Benhelal, O., Chahed, A., Laksari, S., Abbar, B., Bouhafs, B., and Aourag, H., "First-principles calculations of the structural, electronic and optical properties of IIAIV antifluorite compounds," *physica status solidi (b)*, Vol. 242, No. 10, 2005, pp. 2022–2032.

[135] Corkill, J. L. and Cohen, M. L., "Structural, bonding, and electronic properties of IIA-IV antifluorite compounds," *Phys. Rev. B*, Vol. 48, Dec 1993, pp. 17138–17144.

[136] Kutorasinski, K., Wiendlocha, B., Tobola, J., and Kaprzyk, S., "Importance of relativistic effects in electronic structure and thermopower calculations for Mg_2Si, Mg_2Ge, and Mg_2Sn," *Phys. Rev. B*, Vol. 89, Mar 2014, pp. 115205.

[137] Kutorasiński, K., Tobola, J., and Kaprzyk, S., "Calculating electron transport coefficients of disordered alloys using the KKR-CPA method and Boltzmann approach: Application to $Mg_2Si_{1-x}Sn_x$ thermoelectrics," *Physical Review B*, Vol. 87, No. 19, 2013, pp. 195205.

[138] Boulet, P. and Record, M. C., "Influence of the modified Becke-Johnson exchange potential on thermoelectric properties: Application to Mg 2Si," *Journal of Chemical Physics*, Vol. 135, No. 23, 2011.

[139] Pulikkotil, J. J., Singh, D. J., Auluck, S., Saravanan, M., Misra, D. K., Dhar, A., and Budhani, R. C., "Doping and temperature dependence of thermoelectric properties in Mg_2(Si,Sn)," *Phys. Rev. B*, Vol. 86, Oct 2012, pp. 155204.

[140] Kim, C.-E., Soon, A., and Stampfl, C., "Unraveling the origins of conduction band valley degeneracies in $Mg_2Si_{1-x}Sn_x$ thermoelectrics," *Phys. Chem. Chem. Phys.*, Vol. 18, No. 2, 2016, pp. 939–946.

[141] Arnaud, B. and Alouani, M., "Electron-hole excitations in Mg2Si and Mg2Ge compounds," *Physical Review B*, Vol. 64, No. 3, jun 2001, pp. 033202.

[142] Satyala, N. and Vashaee, D., "Modeling of Thermoelectric Properties of Magnesium Silicide (Mg2Si)," *Journal of Electronic Materials*, Vol. 41, No. 6, 2012, pp. 1785–1791.

[143] Bahk, J.-H., Bian, Z., and Shakouri, A., "Electron transport modeling and energy filtering for efficient thermoelectric $Mg_2Si_{1-x}Sn_x$ solid solutions," *Physical Review B*, Vol. 89, No. 7, feb 2014, pp. 075204.

[144] Khan, A. U., Vlachos, N. V., Hatzikraniotis, E., Polymeris, G. S., Lioutas, C. B., Stefanaki, E. C., Paraskevopoulos, K. M., Giapintzakis, I., and Kyratsi, T., "Thermoelectric properties of highly efficient Bi-doped Mg 2Si1-x-ySnxGey materials," *Acta Materialia*, Vol. 77, 2014, pp. 43–53.

[145] Luttinger, J. M. and Kohn, W., "Motion of Electrons and Holes in Perturbed Periodic Fields," *Phys. Rev.*, Vol. 97, Feb 1955, pp. 869–883.

[146] Anastassakis, E. and Hawranek, J. P., "Elastic Constants of II-IV Semiconductors," *Phys. Rev. B*, Vol. 5, May 1972, pp. 4003–4007.

[147] Bayerl, D. and Kioupakis, E., "Theoretical limits of thermoelectric figure of merit in n-type TiO_2 polymorphs," *Physical Review B*, Vol. 91, 2015, pp. 165104.

[148] Winkler, U., "Electrical Properties of the Intermetallic Compounds Mg_2Si, Mg_2Ge, Mg_2Sn, Mg_2Pb," *Helv. Phys. Acta*, Vol. 28, No. 633, 1955.

[149] Morris, R. G., Redin, R. D., and Danielson, G. C., "Semiconducting Properties of Mg_2Si Single Crystals," *Phys. Rev.*, Vol. 109, Mar 1958, pp. 1909–1915.

[150] Stella, A. and Lynch, D., "Photoconductivity in Mg2Si {AND} Mg2Ge," *Journal of Physics and Chemistry of Solids*, Vol. 25, No. 11, 1964, pp. 1253 – 1259.

[151] Stella, A., Brothers, A. D., Hopkins, R. H., and Lynch, D. W., "Pressure Coefficient of the Band Gap in Mg2Si, Mg2Ge, and Mg2Sn," *physica status solidi (b)*, Vol. 23, No. 2, 1967, pp. 697–702.

[152] Lott, L. A. and Lynch, D. W., "Infrared Absorption in Mg_2Ge," *Phys. Rev.*, Vol. 141, Jan 1966, pp. 681–686.

[153] Mead, C. A., "Photothresholds in Mg2Ge," *Journal of Applied Physics*, Vol. 35, No. 8, 1964, pp. 2460–2462.

[154] Zaitsev, V. and Nikitin, E., "ELECTRICAL PROPERTIES THERMAL CONDUCTIVITY AND FORBIDDEN BAND WIDTH OF MG 2 SN AT HIGH TEMPERATURES," *FIZIKA TVERDOGO TELA*, Vol. 12, No. 2, 1970, pp. 357–361.

[155] Lipson, H. G. and Kahan, A., "Infrared Absorption of Magnesium Stannide," *Phys. Rev.*, Vol. 133, Feb 1964, pp. A800–A810.

[156] Blunt, R. F., Frederikse, H. P. R., and Hosler, W. R., "Electrical and Optical Properties of Intermetallic Compounds. IV. Magnesium Stannide," *Phys. Rev.*, Vol. 100, Oct 1955, pp. 663–666.

[157] Aizawa, T., Song, R., and Yamamoto, A., "Solid-State Synthesis of Thermoelectric Materials in Mg–Si–Ge System," *MATERIALS TRANSACTIONS*, Vol. 46, No. 7, 2005, pp. 1490–1496.

[158] Vazquez, F., Forman, R. A., and Cardona, M., "Electroreflectance Measurements on Mg_2Si, Mg_2Ge, and Mg_2Sn," *Phys. Rev.*, Vol. 176, Dec 1968, pp. 905–908.

[159] Tiago, M. L., Ismail-Beigi, S., and Louie, S. G., "Effect of semicore orbitals on the electronic band gaps of Si, Ge, and GaAs within the GW approximation," *Phys. Rev. B*, Vol. 69, Mar 2004, pp. 125212.

[160] Malone, B. D. and Cohen, M. L., "Quasiparticle semiconductor band structures including spinorbit interactions," *Journal of Physics: Condensed Matter*, Vol. 25, No. 10, 2013, pp. 105503.

[161] Strehlow, W. H. and Cook, E. L., "Compilation of Energy Band Gaps in Elemental and Binary Compound Semiconductors and Insulators," *Journal of Physical and Chemical Reference Data*, Vol. 2, No. 1, 1973, pp. 163–200.

[162] Giustino, F., Louie, S. G., and Cohen, M. L., "Electron-Phonon Renormalization of the Direct Band Gap of Diamond," *Physical Review Letters*, Vol. 105, No. 26, Dec. 2010, pp. 265501.

[163] Tritt, T. M., *Thermal Conductivity*, Kluwer Academic/Plenum Publishers, New York, 2004.